Nicolaus Copernicus University in Toruń
Faculty of Physics, Astronomy and Informatics

Decaying Feshbach Resonances in Complex Ultracold Systems

Doctor of Philosophy Dissertation

by

Marcin Umiński

Supervisor

Dr hab. Piotr S. Żuchowski, Prof. UMK

Co-supervisor

Dr inż. Mateusz Borkowski

Toruń, September 2025

Acknowledgements

I would like to thank my supervisor, Piotr Żuchowski, for his great support and effort he put into guiding during my PhD research. His passion and expertise had profound impact on my work, as he not only led me through the quantum realm of ultracold physics, but also demonstrated what the true figure of a scientist should be. I'm also thankful for all his patience and understanding throughout the years of our collaboration.

My thanks go to my coworkers, Mateusz Borkowski and Maciej Kosicki, for sharing their knowledge with me and for their invaluable feedback and motivation.

I want to acknowledge the community of our faculty, especially Mirosław Bylicki, Roman Ciuryło, Czesław Koepke and Jarosław Zaremba, who have been a great source of insipiration, and from whom I have learned much since the very beginning of my academic journey.

Finally, I would like to express my heartfelt gratitude to my family for their unwavering support, without which this would not have been possible, especially my parents, who always placed great emphasis on my education, and, last but not least, my loving wife Julia, who has stood by my side through this entire time.

Contents

List of Tables

List of Figures

CHAPTER 1

Introduction to Feshbach resonances

The aim of this chapter is to introduce the concept of ultracold physics, the basics of quantum resonances, and the theoretical basis of the field. This chapter addresses what cold atoms and molecules are and why they are scientifically important. It discusses how said species are obtained, trapped, and measured. It introduces the theory of interaction potentials and scattering theory, as well as the concept of quantum scattering resonances: how they are formed and how they impact atomic and molecular collisions. Finally, this chapter discusses major experiments and breakthroughs in the field, placing them in context and setting the stage for the remainder of the thesis.

1.1 Ultracold temperatures, atoms and molecules

The path to reaching ever lower temperatures in physics led to the revolutionary accomplishment of obtaining Bose-Einstein Condensates in 1995 [5, 6], over 70 years after its theoretical prediction, in rubidium and sodium atoms, which resulted in the Nobel Prize in Physics in 2001 [7, 8] and paved the way for a new field of physics.

A Bose-Einstein Condensate is a macroscopic quantum-mechanical state of matter in which all particles occupy the same ground state. As the name implies, those particles must be bosons, that is, particles with integer spins, as they are not limited by the Pauli exclusion principle (which states that multiple identical fermions can not occupy the same quantum state at the same time). All particles can be described with one wavefunction with all its consequences. Condensation occurs at a critical temperature T_c. Below this temperature, the thermal de Broglie wavelength is larger than the distance between atoms. For a uniform ideal Bose gas in three dimensions, $k_B T_c = \frac{2\pi\hbar^2}{m}\left(\frac{n}{\zeta(3/2)}\right)^{2/3}$, which is equivalent to the phase-space density criterion $n, \lambda_{dB}^3 = \zeta(3/2) \approx 2.612$, with k_B being the Boltzmann constant and λ_{dB}- thermal de Broglie wavelength, explained in 1.1.

This led to rapid progress: BECs in other atomic species (mainly alkali or alkali-earth metals but also species as Cr and Er [9, 10], Sr, Li, K, Yb or Dy [11]); quantum degeneracy in fermionic gases [12, 13]; continuous condensation [14] and even molecular condensates - very recently [15]. New experimental tools emerged, which contributed immensely to the field of optics and experimental control, including magnetic and optical traps (later extended to molecules), optical cavities, and optical tweezers [16].

Following the discovery of ion trapping [17] and laser cooling methods [18] (honored with the Nobel Prize in Physics), physics and chemistry managed to reach sub-kelvin temperatures, followed by even lower temperatures in the range of micro- to nanokelvin, which are now known as cold and ultracold ranges, as shown in fig. 1.1. In the cold regime, otherwise small energy splittings such as hyperfine shifts become comparable to the thermal energy scale $k_B T$. As energies decrease, atomic states are limited to small

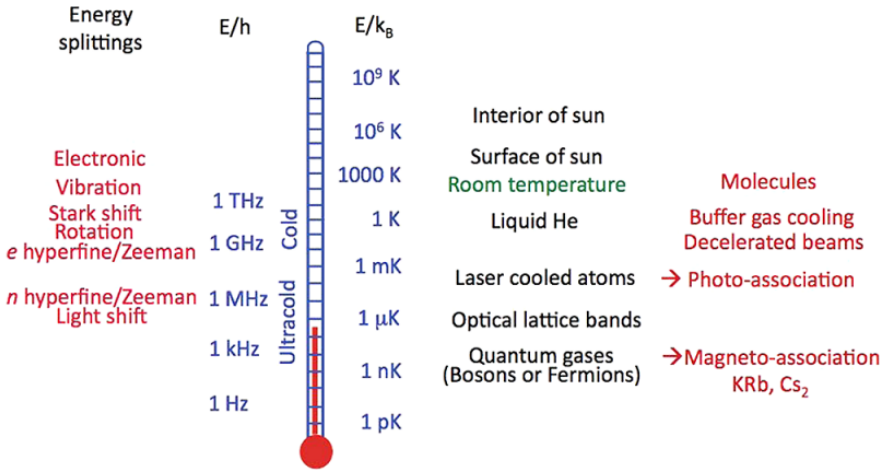

Fig. 1.1: Orders of magnitude of energies and their associated phenomena. Ultracold region highlighted for energies below 1 μK. Reproduced from ref. [1].

quantum numbers, breaking down Bohr's correspondence principle as we no longer average over a large number of quantum states to reproduce classical behavior. Atoms and molecules can be described by the de Broglie formula, where wavelength is given by:

$$\lambda_{dB} = \frac{h}{p} = \frac{h}{\sqrt{2mk_bT}} \tag{1.1}$$

In the ultracold range of temperatures, the de Broglie wavelength is comparable to the interatomic distance within a gas. Thus, collisions between particles are sensitive to long-range interactions [19], subject to experimental control. The possibility of precise manipulation of particles is the main premise of ultracold physics and chemistry.

As partial waves uncouple and all degrees of freedom become quantised, particles in the ultracold regime enable us to build state-selected quantum systems [1]. Atomic and molecular collisions become purely quantum-mechanical, which, paired with finely-tuned conditions, allow us to control particle interactions strictly while manipulating single select systems [20, 21]. Ultracold species exhibit unique properties and let us observe quantum-exclusive phenomena, like interference, diffraction, solitons, and fermion-pairing. This finds applications in fundamental physics [22], including studying physical constants [23, 24] and dark matter [25, 26] optical clocks [27, 28, 29], high-resolution spectroscopy [30, 31], nanochemistry, quantum simulations and computing [32, 33], quantum chemistry, or condensed-matter physics [34].

1.2 Production of ultracold molecules

Since the last decade of the 20th century, the production of ultracold atoms and molecules has been possible using several methods. They are required to effectively cool, trap, and collide ultracold species. Most of the slowing methods are based on using the laser cooling technique, which was awarded the Nobel Prize in Physics in 1997 [18, 35].

A stream of particles is moving with a laser light shining from the opposite direction. The atom absorbs the photon and re-emits it shortly after. While all photons absorbed come from a direction opposite to the atoms' propagation, they are emitted in a random direction. As all photons carry momentum, this results in an effective decrease of the atoms' own momentum [36]. Usually, the light is slightly red-detuned from the transition frequency, so that the Doppler shift from the atom's motion would bring it into resonance. Zeeman's slower brings it a step further- by using a gradient magnetic field along the particles' path, we may keep them in resonance with the laser's frequency as they are slowed down with each consecutive photon absorption.

Once slowed, atoms and molecules need to be held in place in order to conduct further experiments- this process is called trapping. One can imagine using six laser coolers, arranged in the following manner: two in both directions, along each of three axes. Such a setup is used in optical molasses, in which atoms are always pushed back to the center while being further slowed, though not being still. Using an array of two mutually perpendicular, precisely tuned lasers can form a two-dimensional standing wave. Such a plane would have evenly spaced minimums and maximums of potential energy related to the intensity of the electromagnetic field. Atoms seeking external fields' minima would occupy the lows of the wave's amplitudes in what's known as an optical lattice, as in 1.2 [37]. Such atoms, whose energy increases with external field are known as low-field-seeking, as opposed to high-field-seeking ones whose energy decreases with field's increase [38]. A magnetic trap would consist of a three-dimensional varying magnetic field,

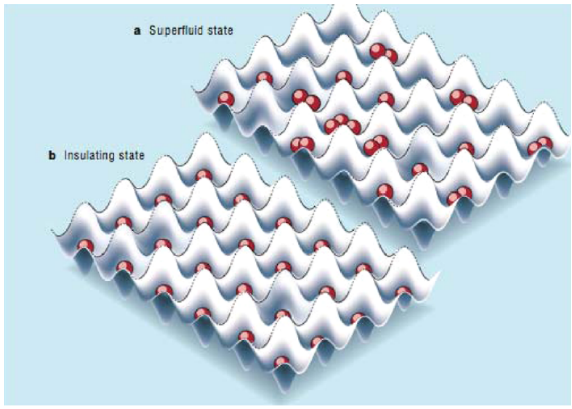

Fig. 1.2: Schematic representation of optical lattice, organising atoms in either a superfluid or a Mott insulator state. Reprinted from [1].

with a defined local minimum at a specific point, which would attract particles in low-field seeking states. Magneto-optical traps are commonly used is ultracold molecules, as they allow for higher densities and lower temperatures than just magnetic traps [39]. They are a combination of laser cooling and magnetic trap, with a magnetic field minimum and a gradually increasing field, tuning particles to resonance with lasers, increasing absorption effectiveness. Another efficient way of atom and molecule trapping, not limited to just low-field seeking, is using optical dipole traps [40].

Such cooling methods are limited by photon recoil, due to the natural linewidth of the laser-induced transition. To lower the temperature even further, sub-Doppler methods are used, like Sisyphus cooling [41, 42, 43, 44] or evaporative cooling [45], which was used to first obtain BEC[5]. The latter requires a certain population of cool atoms [45]. As all

atoms have a certain distribution of energies across population (e.g., Maxwell-Boltzmann distribution), some of them have higher energies than others. Evaporative cooling is essentially a method of selecting just the low-energy atoms and rejecting high-energy ones: by gradually decreasing the depth of the trap the atoms are in, high-energy particles are let out of it, resulting in lowering the amount of atoms, but also decreasing their average energy until it's sufficiently low. Atoms that are kept in magneto-optical traps are usually paired with radio-frequency fields [46, 47], which transfer warmer atoms to untrapped states instead. The remaining particle population's energy may be much lower than after just laser-cooling, by orders of hundreds of nanokelvins.

Finally, obtaining ultracold molecules can be done in several ways, with two main groups of methods: direct and indirect. Direct methods of producing molecules assume obtaining "hot" molecules and cooling them down to ultracold temperatures. Conceptually, those methods would allow the creation of a wide variety of molecules (not only those of easily-trappable atoms), but cooling molecules is much more difficult than atoms due to their complex structures and many energy levels [19]. Simple buffer-gas cooling assumes cooling molecules thermally by injecting them into cold helium atoms. This can produce sub-Kelvin molecules, but separating them from helium is challenging. A variation of this method is called buffer-gas beam[48], in which, once cooled, molecules form a slow particle beam. Another way is using Stark or Zeeman decceleration[49, 50, 51]. Neutral polar molecules enter an inhomogeneous and time-varying electric (or magnetic) field to decelerate. As molecules experience a force in an electric field due to the Stark effect, this changes their energy. The fields are arranged in a way that low-field seeking molecules are always moving against rising potential, which lowers their kinetic energy. Alternatively, they can be cooled by ultracold collisions [52] or by laser cooling [53, 54], just as with atoms. While this method is popular with atoms, molecular energy level structures and additional degrees of freedom don't allow for easy and repeatable optical transitions. Nevertheless, recent experiments resulted in obtaining NaLi molecules by collisional cooling [55], and molecular MOTs allowed cooling molecules such as SrF and CaF to the sub-100 μK range [56, 57].

Indirect methods involve obtaining ultracold atoms and then associating them into desired molecules [58, 16]. Two main methods used succesfully are photoassociation[59, 60, 61] and magnetoassociation[62], sometimes followed by stimulated raman adiabatic passage[61]. Magnetoassociation requires using an external magnetic field, which is varied to tune the ultracold atoms into a Feshbach resonance, allowing atoms to collide and merge. If the colliding species are excited (i.e., rotationally, hyperfine, or by the Zeeman effect), they can also undergo a decay. Resulting molecules are called Feshbach molecules, and this method has been successfully used among many molecular systems. Photoassociation is based on using a laser to transfer colliding atoms into a bound state in electronically excited states: a pair of atoms is transferred into a quasi-bound state in which one atom is excited, which subsequently decays, through spontaneous or stimulated emission, into a lower electronic state, while leaving the molecule in the bound state. While usually limited to alkali or alkali-earth atoms, those methods can efficiently produce dense samples of molecules with temperatures in the sub-microkelvin range [63]. Naturally, cooling molecules is more challenging than atoms, due to the lack of fully closed laser cooling transitions [39, 64]. Their optical trapping is also more technically challenging, e.g., photo-induced losses might appear, and starting densities are low. Optical tweezers can be used to hold the species in the center of the beam waist of

highly-focused laser light, as an oscillating electric field creates an attractive potential, which allows for their spatial manipulation [65, 66, 56] and controlling inelastic molecular collisions [67]. Mergoassociation is a technique involving merging two optical tweezers containing different atoms in order to adiabatically pair them into molecules [68, 58]. Ultracold molecules can also be obtained by manipulating atoms kept in an optical lattice [69] or by merging two parallel beams of particles: with very low relative speeds, their collision energies may be in the subkelvin range- enough for an associating resonance to happen [70].

1.3 Theoretical basics

1.3.1 Interaction potential and Born-Oppenheimer approximation

We start solving the Schrödinger equation $\hat{H}\Phi = E\Phi$ by splitting the movement of atomic nuclei and electrons. Due to their huge mass discrepancy, three orders of magnitude lighter electrons move much faster than protons and neutrons. We may think of electrons that rapidly orbit the nucleus, moving in a time-lapse. Since they move on very different time scales, their wavefunctions can be factorized, which leads us to the Born-Oppenheimer approximation:

$$\Phi_k(\mathbf{r}, \mathbf{R}) = \psi_k(\mathbf{r}, R)\Psi_k(\mathbf{R}) \tag{1.2}$$

where k denotes some *fixed* single electronic state. Within the framework of Born-Oppenheimer approximation[71], the wavefunction for a molecule can be separated into nuclear function Ψ_k and electronic function ψ_k, which is dependent on electronic coordinates, and parametrically on the nuclei positions. The total energy can be written as a sum of nuclear kinetic energy and potential energy, which is an average of an integral over the electronic function. The Born–Oppenheimer leads us to the concept of electronic energy, which constitutes the potential energy of nuclear motion; thus, we can solve the electronic problem independently of the nuclear Schrödinger equation. The electronic Hamiltonian reads

$$\hat{H}_{\mathrm{el}} = \sum_{i}^{N_{\mathrm{el}}} -\frac{1}{2}\nabla_i^2 + \sum_{i>i'} \frac{1}{|r_i - r_{i'}|} - \sum_{i,\alpha} \frac{Z_\alpha}{|r_i - R_\alpha|} + \sum_{\alpha,\alpha'} \frac{Z_\alpha Z_{\alpha'}}{|R_\alpha - R_{\alpha'}|} \tag{1.3}$$

where indices i refer to electrons and α to all nuclei in the system of a charge Z_α. The Hamiltonian of nuclear motion in the simplest, diatomic case is given by is given by

$$\hat{H} = -\frac{\hbar^2}{2\mu}\frac{\partial^2}{\partial R^2} + V_J(R) \tag{1.4}$$

where

$$V_J(R) = \frac{\hbar J(J+1)}{2\mu R^2} + V(R) \tag{1.5}$$

and $V(R)$ is defined through the eigenvalue of $H_{\mathrm{el}}(\mathbf{r}, R)\psi_k(\mathbf{r}, R) = E_{\mathrm{el}}(R)\psi_k(\mathbf{r}, R)$, i.e. the electronic energy, as

$$V(R) = E_{\mathrm{el}}(R) - E_{\mathrm{el}}(R = \infty). \tag{1.6}$$

This is the essence of the Born–Oppenheimer (BO) approximation: one solves the electronic Schrödinger equation at fixed nuclear coordinates $\mathbf{R}$; the resulting electronic energy $E_{\mathrm{el}}(\mathbf{R})$ defines an adiabatic potential-energy surface $V(\mathbf{R})$ on which the nuclei move. The BO approximation is remarkably accurate for most molecules. For systems containing very light atoms (e.g., H, He, Li), deviations from strictly adiabatic behavior can be non-negligible; in such cases, adiabatic (diagonal) and nonadiabatic corrections are commonly included. The BO separation becomes unreliable near regions of strong interstate coupling—most notably at conical intersections in polyatomics or avoided crossings in diatomics—where the product ansatz in Eq. (1.2) ceases to be adequate and a coupled-state (or diabatic) treatment is required.

Born–Oppenheimer interaction potentials $V(\mathbf{R})$ can be obtained either empirically—e.g., by inverting spectroscopic or scattering data [72]—or from first principles by solving the electronic Schrödinger equation.

Methods for solving the electronic Schrödinger equation (ab initio electronic-structure theory) constitute a vast discipline. Although these methods are not the central focus here, we briefly summarize the approaches relevant to constructing $V(\mathbf{R})$.

The most basic many-electron approximate method is Hartree–Fock (HF), which adopts an independent-particle picture with a single Slater determinant $|\Phi_0\rangle$ as the wave function. HF treats each electron as moving in the average field of all the others, capturing the mean-field Coulomb interaction and exchange exactly for the chosen determinant, but it omits dynamical electron correlation arising from the instantaneous electron–electron repulsion. On top of HF, a well-established hierarchy of correlated methods has been developed [**?**]. Particularly important is coupled-cluster (CC) theory, which uses the nonlinear exponential ansatz

$$e^{T}|\Phi_0\rangle \quad T = T_1 + T_2 \ldots \tag{1.7}$$

yielding a size-extensive (correctly dissociating), systematically improvable framework (e.g., CCSD, CCSD(T)). For many closed-shell ground-state problems, CCSD(T) is often regarded as a gold-standard, largely black-box approach. With sufficiently large basis sets, current ab initio treatments can approach accuracies of a few cm^{-1} in well depths for weakly bound complexes typical of ultracold chemistry. Unlike HF—which lacks dispersion and therefore fails to reproduce the correct long-range behavior—correlated methods recover the van der Waals tails ($-C_6/R^6 - C_8/R^8 - \cdots$), crucial for quantitatively reliable cold atom–atom and molecule–atom collision potentials.

1.3.2 Nuclear motion and close-coupling equations

Thanks to the Born-Oppenheimer approximation, we may obtain the interaction potential, or the potential hypersurface on which the atomic nuclei may move. Atoms may move in relation to each other; their rotationally- vibrational movement must be considered, and energy levels associated with it found to calculate the eigenfunctions of this movement. The Hamiltonian includes additional terms for new degrees of freedom of the molecule. Since the conservation of angular momentum is a consequence of spatial isotropy (as stated in Noether's theorem), in the case of an anisotropic interaction potential, separate angular momenta of subsystems of the bigger system are not conserved:

just their sum, which is the total angular momentum, is preserved. It should be noted that in the case of space anisotropy (i.e., due to the presence of an external magnetic field), only the projection of the total angular momentum is a good quantum number.

In this introductory chapter, let us consider a rigid-rotor type of molecule colliding with a structureless atom. As a matter of fact, all systems considered in this paper can be viewed as some derivative of that model: atom-atom cases correspond to zero anisotropy (vide infra), while highly magnetic atoms resemble homonuclear molecules. However, for the atom-rigid rotor case studied further in this work, the Hamiltonian for nuclear motion, which considers additional rotational motion, may be written as [71]:

$$\hat{H} = -\frac{\hbar^2}{2\mu R^2}\frac{\partial^2}{\partial R^2}R^2 + \frac{\hat{L}^2}{2\mu R^2} + \hat{V} + \hat{H}_A + \hat{H}_B \tag{1.8}$$

In Jacobi coordinates, the interaction potential is a function of the distance between the atoms and just one angle θ:

$$\hat{V} = V(R,\theta) \tag{1.9}$$

The interaction potential is the sum of the van der Waals attraction and the Coulomb repulsion. It is often represented with model potentials, like Lennard-Jones written in 1.10 or Tang-Tönnies potentials [73], that capture those two effects. It is derived from the states of separated interacting species and their complex due to their long-range interactions[19]. Such potentials depend asymptotically on the type of interaction: they scale with $\frac{1}{r^6}$ for neutral atoms and atom-molecule interactions, $\frac{1}{r^4}$ atom-ion, $\frac{1}{r^3}$ dipole-dipole, etc. It models an equilibrium distance between repulsive and attractive forces and the resulting potential well's depth. Plot of a model Lennard-Jones potential with centrifugal barrier is presented in 1.5.

$$V(r) = 4\varepsilon\left[\left(\frac{\sigma}{r}\right)^{12} - \left(\frac{\sigma}{r}\right)^{6}\right] \tag{1.10}$$

It is standard procedure for the interaction potential operator $\hat{\mathcal{V}}$ from 1.9 to be expanded in Legendre polynomials in case of aspherical atoms and molecules.[74]

$$V(R,\theta) = \sum_{\lambda} V_\lambda(R) P_\lambda(cos\theta) \tag{1.11}$$

with V_0 being an isotropic potential, and parts with $\lambda > 0$ representing anisotropic interactions. The term $\mathcal{V}_0(R)$ has the physical interpretation of *orientation* average potential, while $\mathcal{V}_k(R)$ for $k = 2,\ldots,2l$ are the anisotropic potentials. The potential can have many spin multiplicities, and the low-spin and high-spin potentials can be different for each molecule.

The Hamiltonian from 1.4 may be rewritten to include H_{int} explicitly:

$$\hat{H} = -\frac{\hbar^2}{2\mu}\frac{\partial^2}{\partial R^2} + V_J(R) + \hat{H}_{int}(\rho) \tag{1.12}$$

The Schrödinger equation $\hat{H}\Psi = E\Psi$ can be written as

$$[-\frac{\hbar^2}{2\mu}\frac{\partial^2}{\partial R^2} + \frac{\hat{L}^2}{2\mu} + V(R,\rho) + \hat{H}_{int}(\rho)]\Psi(R,\rho) = E\Psi(R,\rho) \tag{1.13}$$

In the formula 1.5 μ is the reduced mass of the system, and potential energy is a sum of centrifugal potential [75] and effective potential energy, often shifted so that $V(R) \to 0$ as $R \to \infty$. H_{int} is a sum of independent internal Hamiltonians of separated particles in the long range. H_{int} contains all effects of external fields, atoms, and their internal structure. Ψ is the collision wavefunction and ρ are generally coordinates other than R, not to be confused with θ used previously.

Since the Hamiltonian is the full energy operator, H_{int} contains other terms, if applicable. Most commonly, it may also describe energy level changes due to spin-orbit coupling and hyperfine shift, as well as energy change in an external magnetic field- the Zeeman effect [38]. Hyperfine interaction depends on the hyperfine coupling constant and the dot product of electronic and nuclear spin. Similarly, spin-orbit interaction is based on the interaction of an electron's magnetic field coming from rotational and orbital motions.

$$\hat{H}_{HF} = a_{HF}\hat{i} \cdot \hat{s} \tag{1.14}$$

The Zeeman effect is the splitting of energy levels in an external magnetic field. As particles spin freely along an axis, the orientation of the axis isn't important from energy's point of view. Situation changes, however, in a magnetic field: energies change, depending on the field's intensity and the projection of the spin on the magnetic field. This is true for both nuclei and electrons. This effect is demonstrated on the plot of lithium's states energies in a magnetic field 1.3. Thus, the Hamiltonian may include:

$$\hat{H}_Z = (g_e \mu_B \hat{s}_z + g_j \mu_N \hat{i}_z) B_Z \tag{1.15}$$

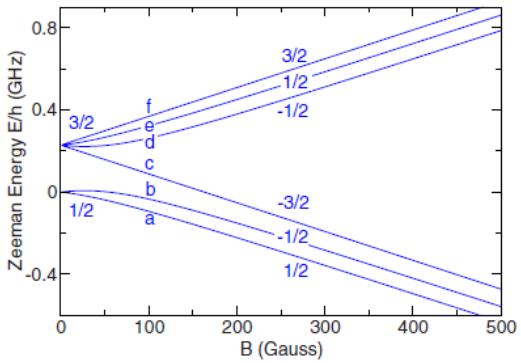

Fig. 1.3: Atomic energy levels and Zeeman splitting in ^6Li atoms. At zero field, the energy depends on the total angular momentum F. In a magnetic field, energies shift according to the angular momentum's projection m_F. In high magnetic fields, levels are grouped based on their m_J. Reproduced from [2]

The full wavefunction in eq 1.13 can be expanded as

$$\Psi(R, \rho) = \frac{1}{R} \sum_i \phi_i(\rho) \psi_i(R) \tag{1.16}$$

as a sum of N functions forming the basis set.[76] Their number, while arbitrary, must be sufficiently high to achieve physical convergence in results. Channel functions $\phi_i(\theta)$ contain information about the system's structure and its representation; they often are eigenfunctions of the Hamiltonians of separate particles.

Substituting the equations, we arrive at the so-called "close coupling" equations [77, 78, 79]:

$$[-\frac{\hbar^2}{2\mu}\frac{\partial^2}{\partial R^2} - E]\psi_j(R) = -\Sigma W_{ji}(r)\psi_i(R) \tag{1.17}$$

with coupling elements W_{ij} that couple functions between different channels

$$W_{ij}(r) = \int \phi_j(\rho)[\frac{\hat{L}^2}{2\mu r^2} + V(r,\rho)]\phi_i(\rho)d\rho \tag{1.18}$$

We may choose a basis set in which the W matrix is diagonal. asymptotically as $R \to \infty$ and then sort the channels. The channels are either open with energy higher than W_{ii}, in which particles are free to separate, or closed ($(E < W_{ii})$ in which particles cannot reach infinite separation. The wavevector k for the ith channel is defined as

$$\frac{\hbar^2 k_i^2}{2\mu} = |E - W_{ii}(R \to \infty)| = E_{k,i} \tag{1.19}$$

and boundary conditions are

$$\Psi(R \to 0) = 0 \tag{1.20}$$

$$\Psi(R \to \infty) = \frac{1}{R}[\phi_j(\rho)k_j^{-1/2}e^{-ik_j r + iL_j\pi/2} + \Sigma S_{ji}\phi_i(\rho)k_i^{-1/2}e^{-ik_i r + iL_i\pi/2}] \tag{1.21}$$

The first part of the equation 1.21 describes the wavefunction in the incoming channel j, and the second part is a sum over all different open channels the wave may be scattered into. The result of the scattering process is described by the Scattering matrix S defined above.

The S-matrix is crucial, as it contains information about the scattering process. It's a complex unitary, symmetric matrix of $N \times N$ elements for each open channel. Its general physical property is that it relates to the phase shift δ as $S(k) = e^{2i\delta(k)}$[80]. Equation 1.17 can be formally rewriten in the matrix notation [78, 81] as:

$$[\mathbf{1}\frac{d^2}{dr^2} + \mathbf{W}(r)]\mathbf{\Psi}(r) = 0 \tag{1.22}$$

where

$$\mathbf{W}(r) = 2\mu[E\mathbf{1} - \mathbf{V}(r)] \tag{1.23}$$

The solution to eq 1.22 is a matrix representing N linearly independent solutions with N coefficients ψ_{nm} each for every state. Due to the fact that with $R \to \infty$ the Hamiltonian is limited to independent particles' individual Hamiltonians [81], as shown in 1.12, matrix W is asymptotically diagonal

$$W_{nn}(r) = k_n^2 = 2\mu[E - \epsilon - \frac{l(l+1)}{R^2}] \tag{1.24}$$

And equation 1.21 can be written as

$$\lim_{R\to\infty} \mathbf{\Psi}(r) = \mathbf{\hat{h}^{(2)}}(r) - \mathbf{\hat{h}^{(1)}}(r)\mathbf{S} \tag{1.25}$$

With matrix operators

$$\mathbf{\hat{h}^{(1)}}(r) = \begin{bmatrix} k_1^{-1/2}\hat{h_{l1}}^{(1)}(k_1 r) & 0 \\ 0 & k_1^{-1/2}\hat{h_{l1}}^{(1)}(k_2 r) \end{bmatrix} \tag{1.26}$$

$$\mathbf{\hat{h}^{(2)}}(r) = \begin{bmatrix} k_1^{-1/2}\hat{h_{l1}}^{(2)}(k_1 r) & 0 \\ 0 & k_1^{-1/2}\hat{h_{l1}}^{(2)}(k_2 r) \end{bmatrix} \tag{1.27}$$

As mentioned above, there are N linearly independent solutions that fulfill boundary conditions 1.21, but to know their combinations, we first need to propagate and match them in the long range. We have an $N \times N$ wavefunction matrix $\mathbf{\Psi}(R)$, with one index specifying the solution and the other the channel the coefficient refers to. There are several methods of propagating the solutions; the most commonly used is the log-derivative method [82, 83, 84], which is the backbone of modern quantum chemical calculations [85, 86]. This method doesn't propagate the wavefunction itself (which may be problematic for classically forbidden regions for closed channels), rather its logarithmic derivative:

$$\mathbf{Y}(R) = \frac{d\mathbf{\Psi}}{dR}\mathbf{\Psi}(R)^{-1} \tag{1.28}$$

After the propagation, the solutions are matched to the long-range boundary condition that in $\lim_{R\to\infty}$

$$\mathbf{\Psi}(R) = \mathbf{J}(R) + \mathbf{N}(R)\mathbf{K} \tag{1.29}$$

where **J** and **N** are diagonal matrices of spherical Bessel functions [87].
K is known as the reactance matrix containing information about the collision, and it's related to the S-matrix by

$$\mathbf{S} = (1 + i\mathbf{K_{00}})^{-1}(1 - i\mathbf{K_{00}}) \tag{1.30}$$

with K_{00} being K-matrix elements related to open channels. Collisional cross section from state α to β is given by

$$\sigma_{\alpha,\beta} = \frac{\pi}{k_\alpha^2}\Sigma|\delta_{i,j} - S_{i,j}|^2 \tag{1.31}$$

with i, j being channels related with energy levels α, β. In case of scattering a structureless atom, we may rewrite the elastic cross section as a sum over partial waves related to the quantum number L:

$$\sigma_{el} = \frac{4\pi}{k_\alpha^2}\sum(2L+1)sin^2\delta_L \tag{1.32}$$

x and total inelastic cross section as:

$$\sigma_{\alpha,inel} = \frac{\pi}{k_\alpha^2}\sum_{i,j} 1 - |S_{i,j}|^2 \tag{1.33}$$

At low energy, scattering is dominated by long-range interactions, and for higher Ls, it is suppressed by the centrifugal barrier. For a multi-channel process, scattering may be characterised by complex scattering length $a(k) = \alpha(k) - i\beta(k)$, defined for the ith channel as:

$$a_i(k) = \frac{1}{ik_i}(\frac{1 - S_{ii}(k)}{1 + S_{ii}(k)}) \tag{1.34}$$

which conveniently determines elastic and inelastic scattering cross sections:

$$\sigma_{el} = \frac{4\pi|a_s|^2}{1 + k^2|a_s|^2 + 2k\beta} \tag{1.35}$$

$$\sigma_{inel} = \frac{4\pi\beta}{k(1 + k^2|a_s|^2 + 2k\beta)} \tag{1.36}$$

1.3.3 Bound states

Bound states are states with energies lying below the dissociation threshold. These would be states of discrete energies locally inside the potential well. A special category of states with resemblance of bound states are the meta-stable states, with energies higher than threshold energies. The meta-stable states would be allowed to escape into infinite distance, but are trapped below the potential's local maximum [71]. As they are submerged in the continuum, they can't be normalized as regular bound states. Those states are particularly interesting, as coupling to them is a mechanism behind the Feshbach resonances [75]. Bound state wavefunctions are related to modes of standing waves of nuclear motion propagating within the potential well. They have the property that the nth state wavefunction has n-1 nodes [88], which we often take advantage of.

Coupled-channel methods are useful in finding bound states. The Schrödinger equation 1.22 and coupled-channel equations are the same in the case of bound state calculations. The are different boundary conditions. In case of scattering the wavefunction decays exponentially to zero within limit of $R \to 0$ and propagates as the Bessel function with $R \to \infty$. With bound states, the second boundary condition is

$$\Psi(R \to \infty) = 0 \tag{1.37}$$

As the bound states' wavefunction can not extend indefinitely beyond its limited region. Only energies of bound states used with the wavefunctions would satisfy both boundary conditions. Hence, the procedure is to perform calculations for particular energy values and verify each time if such energy fulfills the conditions. As one propagation of the wavefunction from one end to the other would run into numerical instability, two propagations are performed: one from a high value of R inwards, and one from a small R outwards. They are then matched in the middle at a specific matching point R_{match} in the classically allowed region. Counting of nodes of the propagated wavefunctions is often used to find all bound state energies, as well as to more easily converge numerically on select states. Within the log-derivative method, the matching condition is for the derivatives [88], as the wavefunctions could be arbitrarily scaled to match themselves:

$$(\Psi_L(R_{match}))'/\Psi_L(R_{match}) - (\Psi_R(R_{match}))'/\Psi_R(R_{match}) = 0 \tag{1.38}$$

For multichannel calculations, N independent solutions must be calculated, and the condition in the matrix notation is:

$$det[\mathbf{Y}_L(R_{match}) - \mathbf{Y}_R(R_{match})] = 0 \tag{1.39}$$

1.4 Scattering resonances

One of the abovementioned phenomena is Feschbach resonances. While described relatively recently, our knowledge of them expands rapidly, and they're a subject of many ongoing studies regarding problems, including multi-body collisions, Efimov states. As they allow us to control the interactions between particles by tuning scattering properties, they play a vital role in obtaining ultracold molecules.

A resonance is an observable event among oscillating and vibrating objects (including single particles as well as massive objects) in which, when a vibration's frequency matches the system's natural frequency, we see a rapid increase in amplitude. Generally speaking, a resonance is associated with metastable states (resonance states [89]) in a system, which break into several subsystems as time passes [80], which means that even though a system has enough energy to break apart, it doesn't happen instantly, but rather decays over time. In the quantum world, a resonant increase of coupling between states may happen when the phase shift changes rapidly over a narrow range of energy [75]. We may observe this as an increase in, for example, scattering length [75] as seen in 1.4. There are two main types of quantum resonances: shape resonances and Feshbach resonances.

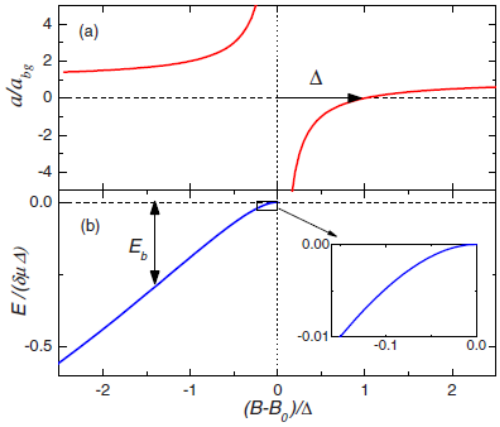

Fig. 1.4: Feshbach resonance observed in the scattering length (a) and molecular state energy near magnetically tuned Feshbach resonance (b). Cited from [2]

1.4.1 Shape resonances

Shape resonances are related to the shape of the interaction potential of colliding particles. They are related to the tunneling effect and based on the existence of a centrifugal barrier in the interaction potential [80]. Potential's form, as described in formula 1.5 and

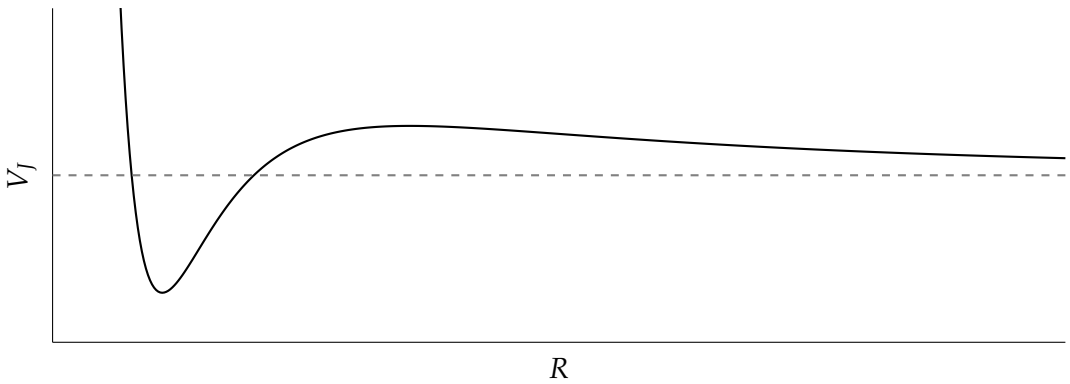

Fig. 1.5: Illustration of a model Lennard-Jones potential, showing the repulsive and attractive contributions as well as the centrifugal barrier.

depicted in fig. 1.5 has two extrema- a minimum at equilibrium distance and a local maximum due to rotational energy of orbiting particles higher than threshold energies (commonly shifted to zero). Truly bound states with negative energies lie below threshold energies, while the dissociation energy is the energy between the bottom of the minimum and the peak of the maximum. Rotationally excited states with energies below the potential's maximum can tunnel through the barrier and dissociate- at an energy lower than the "classical" dissociation energy. As tunneling may be described with a certain probability (or finite time), for the initial vibrational state, we may define the survival probability, which decays as

$$\tau = \frac{\hbar}{\Gamma}$$

as $t \to \infty$. These are the metastable states, which support the existence of collisional resonances. Resonance energy bandwidth is given by $\Delta E = \hbar\Delta\omega$ and Γ is the resonance width ΔE. What's important, such resonances may happen within just one channel (with incoming and outgoing particles remaining in their initial states), they require just a sufficiently high centrifugal barrier.

The derivative of the slope affects resonance parameters, like the rate of decay. They may be well used in describing the behaviour of atomic and molecular single-channel collisions [90, 91, 92], though they may also be related to, for example, potential barriers in radioactive decays [89], and this resonant behavior underlies the operation of diodes and transistors.

1.4.2 Feshbach resonances

This type of resonance is attributed to at least one bound state becoming metastable due to a coupling to a continuum it is embedded in [80]. As the states are associated with different potentials, it is a strictly multi-channel case. Worth noting, by channels we understand combinations of quantum numbers related to specific potentials in a molecular collision. Channels with threshold energy higher than collision energy are called "closed", and with lower energy- open, as depicted in 1.6.

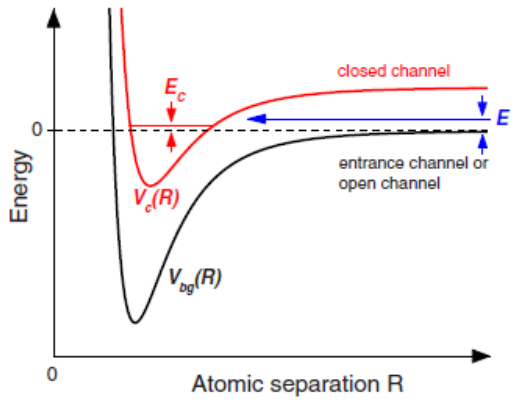

Fig. 1.6: A basic two-channel model for a Feshbach resonance. The resonance occurs when two colliding partners with energy E in the entrance, open channel couple to the bound state with energy E_c supported by the closed channel. Reproduced from [2].

When atoms interact, there may be closely spaced thresholds with related bound states. Some of the higher bound states may cross lower thresholds; such states embedded in a continuum may produce a resonance [38]. When the scattering state of colliding atoms is coupled to an approximate bound state of a different channel, a resonance may be observed, resulting in a rapid change of phase shift of the involved atoms, which in turn greatly increases the scattering length for the collision across a certain energy width. The ratio of resonant to background scattering length defines the strength of the resonance. Since molecular channels and atomic levels split and shift in external fields due to Stark and Zeeman effects, resonance position can be tuned with a magnetic or optical field, which is a crucial property of ultracold resonances. Assuming low collision energies, scattering properties can vary with the external magnetic field, thus allowing the resonances to be controlled. As mentioned before, it is one of the main tools to obtain ultracold molecules indirectly.

Early experiments with the phenomena of bound states coupling to the continuum started in the 1930s. Fano and Feshbach independently carried out research based on different approaches- nuclear and atomic physics. The resonances may be known as Fano-Feshbach resonances; the name Feshbach resonances is more commonly used, however [75]. The first experiment with Feshbach resonances in ultracold gases in 1998 paved the way for the phenomenon to become a tried and trusted tool to control quantum scattering processes. The possibility of using Feshbach resonances to obtain molecules was predicted in 1999 [93]. Currently, Feshbach resonances can be observed in collisions between ultracold molecules [94, 95] and are successfully used for magnetic control of reactive collisions [96, 70].

To introduce the basics of resonance scattering, let's introduce the following [75] and assume a system with two uncoupled channels, as shown in fig. Open background scattering channel $|bg\rangle$ with scattering states labeled by collision energy $|E\rangle = \phi_{bg}(R,E)|bg\rangle$ and closed channel $|c\rangle$ supporting a bound state $|C\rangle = \phi_c(R)|c\rangle$ with its eigenenergy E_c. Functions $\phi_{bg}(R,E)$ and $\phi_c(R)$ are the eigenfunctions of the Hamiltonian given by 1.12 for the open and closed channels' potentials, respectively $V_{bg}(R)$ and $V_c(R)$. When the Hamiltonian coupling $W(R)$ is taken into account, the two states start mixing, and scattering in the open channel is dependent on both background phase shift and resonant phase shift, with a standard Breit-Wigner form [97, 98].

$$\eta(E) = \eta_{bg}(E) + \eta_{res}(E) \tag{1.40}$$

The short-range interaction $W(R)$ determines the resonance's width and energy shift $E_c \to E_c + \delta E(E)$:

$$\Gamma(E) = 2\pi|\langle C|W(R)|E\rangle|^2 \tag{1.41}$$

$$\delta E(E) = \int \frac{|\langle C|W(R)|E\rangle|^2}{E - E'} dE' \tag{1.42}$$

The main difference between regular and resonance scattering is that if the collision energy is close to the open channel threshold, the resonance's width and shift depend explicitly on the energy [99, 100].
The crucial property of Feshbach resonances is the possibility to tune the states into them by shifting the threshold resonance positions, through varying external magnetic or optical fields. While both of those follow the same formalism, magnetic resonances may be

lossless, while optically-induced resonances are always related to decay processes in the excited states.
As scattering length passes through a pole whenever phase changes by $\frac{1}{2}\pi$, its dependance on magnetic field in an elastic scattering process follows the formula 1.43 [3, 101], showing a peak at magnetic field matching resonance as seen in fig. 1.4.

$$a(B) = a_{bg}(1 - \frac{\Delta_B}{B - B_{res}}) \tag{1.43}$$

The width Δ_B is constant in low energy, as $k \to 0$, while Γ remains proportional to the wavevector [102]. Their relation is given by

$$\Gamma_B = -2a_{bg}k\Delta_B \tag{1.44}$$

Let's introduce decay rate $\gamma/\hbar$; the mean scattering length [103] follows the formula

$$a(B) = \alpha - i\beta = a_{bg} - a_{res}\frac{\gamma E_0}{E_0^2 + (\gamma/2)^2} \tag{1.45}$$

The decay rate is related to the fact that the resonance may cause a reaction and loss of the sample's population, as observed in fig. 1.8. Scattering length in optical resonances has additional complex collisional loss β, and the strength of the resonance may be defined by its resonant scattering length [104]:

$$a_{res} = a_{bg}\Gamma/\gamma \tag{1.46}$$

Worth noting is that the scattering length follows a different behaviour in decaying states; its poles have a finite value. Similarly to dampened mechanical resonances, coupling to inelastic channels suppresses the scattering length [3] as shown in fig 1.7. Importantly, the imaginary part of the scattering length has a peak in the same position as the real part changes its sign. Decay in this form may mean atoms merging into Feshbach molecules through magnetoassociation and later experiencing 'leak' to another state via collisional relaxation[105].

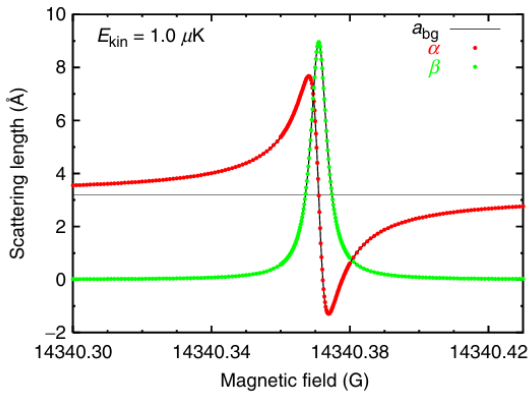

Fig. 1.7: Real and imaginary parts of the scattering length near an optically tunable, inelastic Feshbach resonance. Reproduced from [3].

An important feature of resonances is their distribution with respect to energies and magnetic fields at which they appear. Light systems display regular patterns of independent resonances. In contrast, the resonances in some systems were found to be extremely

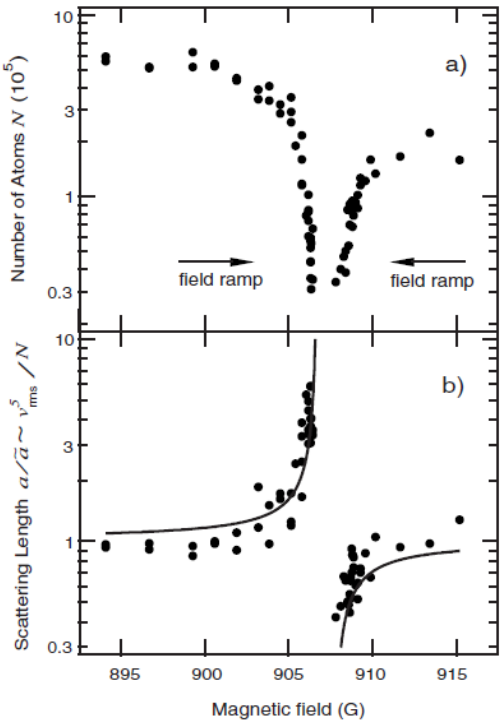

Fig. 1.8: Observation of magnetically tuned Feshbach resonance in an optically trapped Bose-Einstein condensate sample. The upper panel shows a strong loss of atoms due to resonant three-body recombination. The bottom panel presents the profile of the measured scattering length near the resonance. Reprinted from [4].

dense. In case the coupling strength between the scattering state and the bound state is very large, the position and shape of nearest neighbour resonances can be altered, as one resonance affects the positions of others by repulsion, exhibiting chaotic behaviour. Such a phenomenon was noticed as early as 1950 in nuclear scattering and explained by E. Wigner, who used random matrix theory to model these resonances.

Chaos in the context of scattering resonances was first studied by Bohn's group in [106] and [107] in erbium atoms, further studied in Yb and Li+ CaF and CaH[108, 109], and later on in ErYb molecules [110]. A similar analysis was also performed on Cr and Eu bearing dimers [111]. Quantum chaos characterizes the distribution of resonances, and statistical methods are employed to distinguish and characterize them [109, 107]. Their positions, analyzed in terms of spacing statistics, could be described by two main cases: Poisson, if resonances are not correlated and randomly positioned, or Wigner-Dyson, if strongly mixed states repel each other. For spacing s between two neighbouring resonances, the distributions are given by:

$$P_{WD}(s) = \frac{\pi s}{2} \exp\left(-\frac{\pi s^2}{4}\right) \tag{1.47}$$

$$P_P(s) = \exp(-s) \tag{1.48}$$

Between these limiting cases (chaotic and non-chaotic) Brody distribution is introduced where the distribution is proportional to $\exp\left(-\alpha s^{(}\eta+1)\right)$ where $\eta = 0$ means non-chaotic Poisson, and $\eta = 1$ chaotic Wigner-Dyson case. η characterizes *"randomness"* of such resonances and can be fitted to the actual distribution of nearest neighbours in a

properly constructed histogram of energy level spacings.

1.5 Motivation

Ultracold atomic gases have emerged as a universal framework for exploring quantum many-body physics, offering unprecedented control over interactions, dimensionality, and preparation of quantum states. Their tunability enables the precise engineering of model Hamiltonians, making them ideal candidates for simulating complex quantum systems. One of the most compelling applications of ultracold matter is the development of quantum simulators—tailored quantum systems designed to emulate the behavior of more complex or less accessible quantum models, like various modifications of the Hubbard Hamiltonian [112]. These simulators hold great promise for addressing longstanding challenges across condensed matter physics, quantum chemistry, and high-energy physics, including problems that are computationally intractable with classical algorithms [113]. One of the areas of the global technological arms race is quantum computing. This promising and developing field is heavily dependent on progress in ultracold physics- trapped ions [114] or Rydberg atoms [115] are prime candidates for qubits [32, 116, 117]. As stated before, optical lattice clocks are the state-of-the-art frequency standards with applications beyond just measuring time, and ultracold species are the bread and butter of modern high precision spectroscopy [118, 119].

Physicists of various backgrounds try to reach beyond the Standard model- and ultracold molecules play an important role in this search for new physics, as a tool to find particles that would violate charge-parity symmetry [120]. Symmetric top molecules are candidates for discovering T-violating interactions [121]. Electronic states, dipole moments, and zero-field splitting in molecules of DyOH or ErOH suggest they might be used as well in symmetry-violation research [122]. Ultracold experiments are a source of precise values of physical constants, such as the ratio between electron and proton masses m_e/m_p [123, 124] or properties of electrons, like their electric dipole moment [125, 126, 127, 2]. Progress in trapping technology enabled conducting few- and many-body collisions [128, 15] and interactions of atom-molecule [129] or ion-molecule [130, 131] have been a subject of experiments in recent years. Ultracold molecules provide a great case for researching Efimov states [132] or quantum chaos [107, 110, 133, 109].

Among various types of interactions, dipole-dipole interactions have attracted significant attention due to their anisotropic and long-range nature, opening avenues to explore novel quantum phases and phenomena not accessible with isotropic, short-range interactions alone. Thus, it is not surprising that quantum gases of molecules or ultracold highly magnetic atoms, like Erbium, Dysprosium, Thulium, and Holmium, attracted so much attention in the past 10 years- they proved to be an excellent platform for research [10, 134].

Systems with both fermionic and bosonic isotopes available are interesting, as they provide distinct opportunities for quantum simulations: not only different mass and energy level structure, but also different distribution of species, since fermions obey the Pauli exclusion principle. This also implies that fermionic atoms cannot form resonances in the s-wave collisions, as one of the interacting partners must occupy a higher state.

Such exclusion alters resonance spectra.

It was found that highly magnetic atoms exhibit an extremely dense pattern of resonances, which is attributed to their rich energy level structure and multitude of couplings. Compared to alkali metal dimers, the key difference in the mechanism that drives the resonances is related to the *anisotropy* of the electronic cloud of highly magnetic atoms [135]. One of the most important way of controlling their interactions and scattering properties are Feshbach resonances, in which the closed channels of colliding species are coupled to the continuum of scattering states. In most cases, these are used whenever atoms are in their absolute ground states. The presence of open channels above the initial states can completely change the character of resonance.

The objective of this thesis is to give insight into the nuances of decaying Feshbach resonances in complex systems: their feasibility, tunability, and application. Understanding this phenomenon is crucial in ultracold physics, and great progress in the previous years has just proved the potential for discovery in this field.

This introductory chapter presents the idea of ultracold physics and its role, as well as explaining the basic theory behind it. The remaining part of this work is organised as follows. Each chapter is dedicated to research in different molecular systems. In Chapter 2, collisions between NO^+ ions and molecular hydrogen are discussed. While not focused directly on resonances, bound state calculations explain molecules' behaviour as a function of increasing orbital angular momentum, and the insights gained in this study are applied in the later chapters. Chapter 3 is focused on collisions between ultracold helium and lithium. The theoretical frameworks and computational methodology are explained in detail. Preliminary results are also presented. Chapters 4 and 5 are dedicated to resonance calculations in Li-Er and K-Dy molecules, respectively. These molecules, with their distinct energy level structures and anisotropic shapes, give detailed information about resonance patterns and positions. The two systems are compared and contrasted to highlight how magnetic moment and reduced mass influence resonances. Lastly, Chapter 6 discusses recent progress in theoretical research on Sr-SrOH molecules. The work is summarized in the last chapter.

CHAPTER **2**

Interactions of nitrosonium and hydrogen

2.1 Introduction to $NO^+ + H_2$

The ion-molecule collisions are responsible for many different processes both in Earth's atmosphere and in the interstellar medium. The NO^+ ion is one of the most stable diatomic ions [136] and, in turn, is one of the most abundant species in the thermosphere, playing a crucial role in the energy balance; it's also one of the most active ions in atmospheric reactions [137] The hypothesis of the presence of the nitric oxide cation was discussed before [138, 139] and finally confirmed in 2014 [140]. This revelation provides insight into nitrogen reactions in the ISM and the formation of HNO molecules. Due to this, the NO^+ ion plays a key role in astrophysical studies [136].

Precise characterisation of NO^+ interactions with atmospheric and interstellar species is of interest. Collisional data have been previously calculated for collisions of NO^+ with several noble gases [141, 142]. Experimental and theoretical research of NO^+ interactions with atmospheric gases, such as N_2, O_2, H_2O,CO_2 was conducted in the recent years [143]. Despite its importance, very little is known about interactions with the most dominant ISM collider- H_2, as only basic calculations of potential energy with reduced dimensionality were performed [144].

To satisfy this demand and enable more accurate interpretations of observational spectra, a full 4D potential energy surface for NO^++H_2 was obtained using CCSD(T)-F12a ab initio method [145]. The PES computations were supplemented by bound state calculations, providing a method of validating the accuracy of the results. Experimental data could offer additional insight into the system and its resonances.

2.2 Calculation details

The calculations of bound state energies were performed using the BOUND program [146, 86], treating hydrogen's spin isomers, ortho- and para-H_2 separately. For the expansion of the wavefunction, a rotational basis set was used which included NO^+ quantum numbers up to $j = 22$, while for the hydrogen molecule, up to $j = 4$ for para-H_2 and up to $j = 3$ in case of ortho-H_2. Coupled-channel equations (as detailed in 1.17) were solved with the log-derivative method (explained in 1.28). Spatial propagation of wavefunction propagation along R was performed using the log-derivative propagator with a step of $0.01\,a_0$, starting from $2.5\,a_0$ and reaching $18\,a_0$ for deeply bound states, with a matching point of $8\,a_0$. For near-threshold bound states, the R_{max} was increased up to $80\,a_0$). The rotational constants B_0 were set to $1.980\ \mathrm{cm}^{-1}$ for NO^+ and $60.853\ \mathrm{cm}^{-1}$ for H_2 molecules. The centrifugal distortions were taken into account, with distortion constants D equaling $2 \times 10^{-7}\ \mathrm{cm}^{-1}$ for NO^+ and $0.0471\ \mathrm{cm}^{-1}$ for H_2.

2.3 Results

Despite a small reduced mass, the system is quite strongly bound. For the ground state of $para - H_2 - NO^+$ it supports 49 bound states, while the $ortho - H_2 - NO^+$ yields 38 bound states in even and 60 in odd parity. To illustrate bound state density, the staircase function $S(E) = \sum_i \Theta(E - E_i)$ is defined for para-H_2–NO^+, where $\Theta(x)$ denotes the Heaviside step function. Plot 2.1 visualizes bound state positions and their derivative dN/dE. As expected, bound state density increases significantly for bound states close to the threshold.

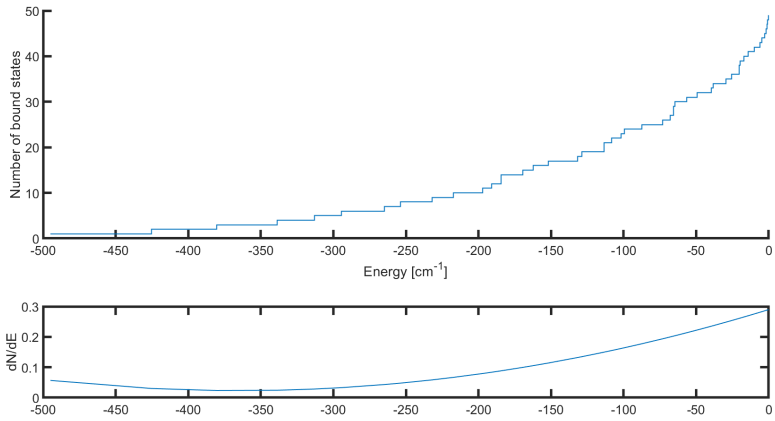

Fig. 2.1: Top panel: staircase function of NO^++H_2 bound states. Bottom panel: derivative of the polynomial fit with respect to energy, dN/dE.

Increasing total angular momentum J splits the rovibrational lines into several components related to angular momentum projection onto the body-fixed frame m_J. Bound states for $J = 0$ and 1 for $ortho-$ and $para - H_2 - NO^+$ interacting with NO^+ are listed relative to the ground rotational states in table 2.1. The fact that $ortho - H_2 - NO^+$ is more strongly bound could be explained by the fact that the main potential anisotropy term, V_{101}, is negative and diagonal in $J = 1$.

Bound states in the range of $550 - 250 cm^{-1}$ are exhibited in plot 2.2. Energy levels are visibly congested. For $para - H_2 - NO^+$, the $J = 0$ manifold remains clearly separated for J up to 8, beyond which states of different total angular momenta cross each other and the pattern becomes blurred. For $ortho - H_2 - NO^+$, however, bound states appear in pairs corresponding to the opposite parities, with a few cm^{-1} distance between them. For rovibrationally excited states, the energy levels strongly overlap.

It could be noticed that in the lowest state, the $para - H_2 - NO^+$ molecular complex behaves like an asymmetric top. To confirm this behaviour, the asymmetric top model was used and, by solving linear equations using results for a few lowest J states, the rotational constants were fitted. Table 2.2 provides energies for those states and matching constants. Results indicate that a higher total angular momentum J is associated with longer intermolecular distance, as values of rotational constants increase. A notable change occurs between the second and third vibrational state, signaling a structural change of molecular geometry. These outcomes can be intuitively understood: the faster

para-H_2 – NO^+				ortho-H_2 – NO^+			
$J = 0$		$J = 1$		$J = 0$		$J = 1$	
Energy	Parity	Energy	Parity	Energy	Parity	Energy	Parity
-498.15	+	-496.54	-	-541.25	+	-541.34	+
		-494.85	-			-541.24	-
		-494.57	+			-539.61	+
-428.20	-	-426.46	-	-537.19	-	-535.56	-
		-425.04	-			-530.40	-
		-424.60	+			-530.29	+
-382.80	+	-380.93	-	-470.67	+	-470.36	-
		-379.26	-			-470.53	+
		-378.64	+			-468.95	+
-341.93	-	-339.95	-	-465.59	-	-463.87	-
		-337.83	-			-459.25	-
		-337.06	+			-459.07	+

Table 2.1: Positions of ro-vibrational levels and parities of bound states of para-H_2 – NO^+ and ortho-H_2 – NO^+. Positions are given related to the ground rotational states of corresponding spin isometries.

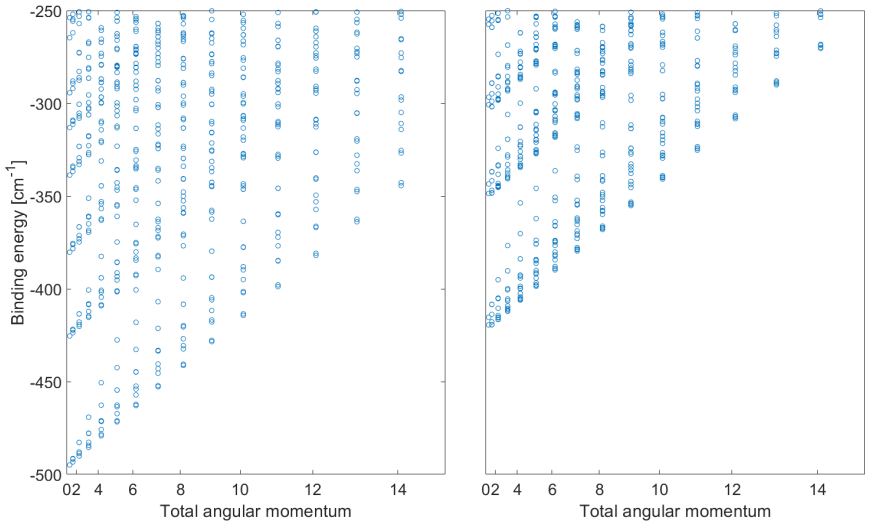

Fig. 2.2: Bound state energies of NO^++H_2 as a function of total angular momentum J. Energies are presented as a function of $J(J+1)$, so that patterns of bound states exhibit linearity. The left panel presents results for $ortho - H_2$, the right panel for $para - H_2$.

the rotational movement, the less stable and regular the complex becomes.

Binding energy for $J = 0$ (cm^{-1})	Asymmetric top rotational constants (cm^{-1})		
	A	B	C
−498.15	2.6375	0.9449	0.6679
−428.20	2.5140	1.0951	0.6454
−382.80	2.9184	1.2459	0.6239
−341.93	3.4926	1.3720	0.6017
−315.85	2.7804	1.1416	0.5957
−297.81	5.1902	1.8187	0.5064

Table 2.2: Asymmetric top rotational constants of lowest bound states of $NO^+ + H_2$

2.4 Chapter summary

In this chapter, a summary of bound state calculations of NO^++H_2 was presented, and rovibrational spectra of this complex were analyzed. Bound states show distinct patterns, different for each nuclear spin isomer of H_2. While the results provide direct information about abundant and important ISM collisions, this work served an educational purpose, and the main outcome is the expertise and techniques developed here, which will be further applied in the following chapters. Bound state patterns, as well as fitting to the asymmetric top model, depict how molecular complexes' rotations change in higher excited states. Both knowledge of this irregularity and the asymmetric top model will be referenced in further sections of this work.

CHAPTER 3

Ultracold Collisions of Helium and Lithium

3.1 Introduction to He+Li

This chapter focuses on collisional processes leading to chemical reactions between ultracold helium and lithium. The main objective of chemistry as a science is to develop insight into chemical reaction mechanisms. This is why understanding them at the microscopic level, from 'first principles', took a fundamentally important place in chemistry, as best proven by several Nobel prizes won by researchers in this and similar fields [17, 7, 8, 18, 147]. The optimal practical realization of this plan is to conduct chemical reactions in perfectly controlled conditions. Cold chemistry was born only 30 years ago as a realization of the dream of attaining a molecular Bose-Einstein condensate and established the foundations of the ultimate control of quantum dynamics experiments using highly controlled fields. There are still unsolved puzzles about how to tune the interaction between ultracold atoms and molecules or how to induce chemical reactions between them. These gaps in our knowledge are the motivation for this study.

The autoionization process in He+Li molecules was described thoroughly before [148], while penning ionization in the photoassociation process was studied by Skomorowski et al [149]. Theoretical studies of controlling ionization processes in various molecules, including He* + Li, were the subject of [150], whereas detailed calculations describing collisions of room-temperature Helium with cold lithium were presented in [151]. As Feshbach resonances in elastic and inelastic ultracold collisions are considered a major tool for molecular association [70, 94], it is tempting to execute fully-controlled collisions leading to obtaining ultracold He+Li mixtures. Experimental possibilities of such process were predicted recently [152], and shortly after the team led by Katrin Dulitz of Freiburg performed experiments with He+Li molecules, including suppression of Penning ionization as a tool for increasing the efficiency of laser cooling and trapping [153] and controlling chemi-ionization in collisions of metastable helium and lithium [154], though no further experiments with this system were carried out as of now.

It is hypothesized that in systems consisting of the metastable helium atom and a paramagnetic molecule, the Penning ionization could be suppressed in a controllable manner through the choice of magnetic fields and the reactant states. In the vicinity of Feshbach resonances, on the other hand, a sudden increase of the reaction rate of ion production should be observed due to the strong mixing of all spin quantum numbers of the whole complex. This theoretical research is dedicated to understanding the Penning ionization process in an external magnetic field. Penning ionization and associative ionization are processes underlying molecular formation [155, 156] relying on quantum resonances, detailed in 3.2:

$$He^* + Li \rightarrow [HeLi]^* \rightarrow He + Li^+ + e^- \tag{3.1}$$

$$He^* + Li \rightarrow [HeLi]^* \rightarrow HeLi^+ + e^- \tag{3.2}$$

This study involves the application of the close-coupling method with optical potential, introducing losses. The method was generally known, but was not studied systematically for optical potentials, nor for systems of excited atoms.

3.2 Theory and methods

Losses to the Penning ionization process are modeled in this system by a complex optical potential. Such an approach requires calculations beyond the hermitian quantum mechanics framework (which assumes that all observables have real eigenvalues) to account for imaginary terms in the Hamiltonian [80]. The full energy operator incorporated has the form 3.3:

$$\hat{H} = -\frac{\hbar^2}{2\mu}\frac{\partial^2}{\partial R^2} + \frac{\hbar^2}{2\mu}\frac{J(J+1)}{R^2} + V(R) - \frac{i}{2}\Gamma(R) \tag{3.3}$$

The interaction potential is the same as the one used for calculations of Penning ionization in metastable helium-alkali atom collisions by Kędziera et al. [157]. To explore separately both short-range and long-range interactions, a Morse/Long-Range potential was used:

$$V(R) = D_e(1 - \frac{u_{LR}(r)}{u_{LR}(r_e)}exp[-\phi(r)y_p(r)])^2 - D_e \tag{3.4}$$

The potential well depth D_E, equilibrium distance r_e, and C_{6-10} coefficients present in u_{LR} were taken from that publication. The potential has two spin anisotropies describing the states of the He+Li molecule. The low-spin, doublet, is lossless and includes an electron exchange term described in [158]; its coefficients were calculated to match results from [159]. The high-spin, quartet state is coupled to the continuum. It gives rise to Feshbach resonances, which are responsible for molecular losses, e.g., via Penning ionization. The complex component present in the quartet potential uses a constant Γ determined semi-empirically as seen in [160]. Plot of the potential is illustrated in fig. 3.1. Its eigenvalues

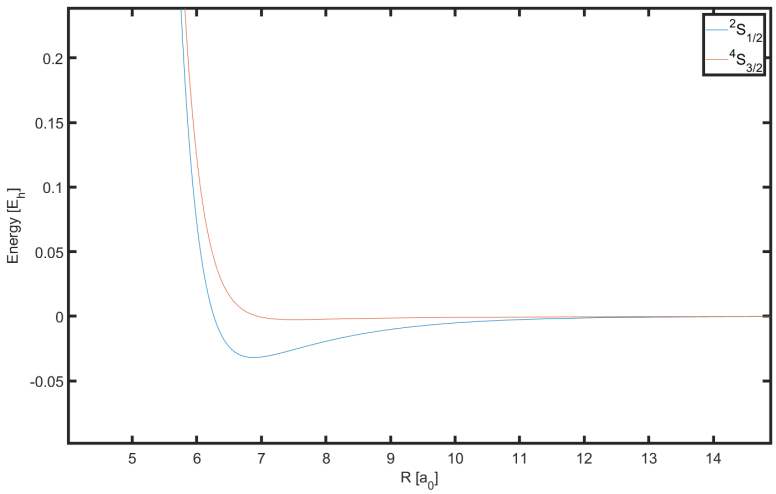

Fig. 3.1: Plot of the interaction potential of high-spin and low-spin $He + Li$ states.

are complex, for resonant states they take the form

$$E = E_r - \frac{i}{2}\Gamma \tag{3.5}$$

where Γ has a physical interpretation as resonance width and is related to the decay rate by $\Gamma = \|\gamma\|^2$. NIST atomic data used for calculations [161], with physical constants taken from [162]. The basis set for the system was constructed as follows: lithium, with its nonzero nuclear spin, is described with quantum numbers $|s, m_S, i, m_i\rangle$, while helium is described by $|s, m_s\rangle$. For calculations of excited helium and lithium, the following values were used: $s_{Li} = 1/2$, $i = 3/2$, $s_{He} = 1$, and selected $m_{tot} = -2$. Interaction potential is diagonal in the basis set of $|(s_{Li}s_{He})S_{AB}, m_S, i, m_I\rangle$. This convention uses lowercase labels for monomer quantum numbers, while capital letters denote quantum numbers of the molecule. Internal atomic energies, including Zeeman and hyperfine terms, as discussed in the previous chapter in 1.15 and 1.14, are diagonal in their respective eigenbases. To relate these representations, relevant Clebsch-Gordan coefficients were used. The Breit-Rabi diagram for He+Li molecules is presented in the graph 3.2.

$$C^{JM}_{j_1 m_1 j_2 m_2} = \langle j_1 m_1 j_2 m_2 | JM \rangle \tag{3.6}$$

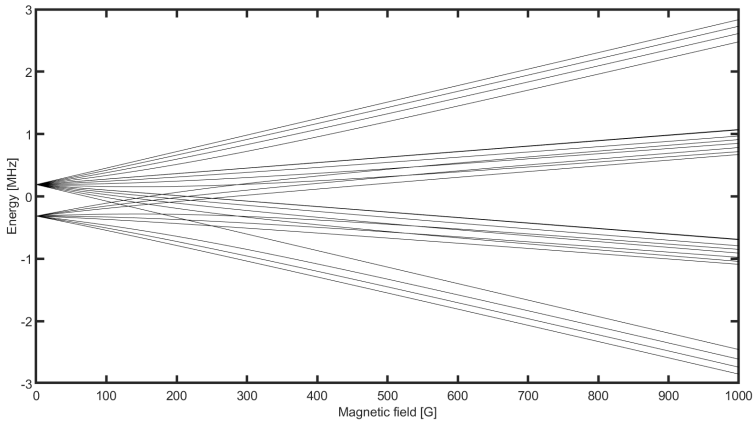

Fig. 3.2: Breit-Rabi diagram for $He + Li$ molecules.

To propagate the wavefunction, the log-derivative and renormalized Numerov methods were used [87]. The log-derivative, which is encoded in popular quantum mechanical programs [146], was explained in the introduction 1.28. The renormalized Numerov algorithm is alternatively used to solve the close-coupling equations 1.22. The method is as follows. First, a three-term recurrence relation is introduced:

$$\left[\mathbf{I} - \mathbf{T}_{n+1}\right]\Psi_{n+1} - \left[2\mathbf{I} + 10\mathbf{T}_n\right]\Psi_n + \left[\mathbf{I} - \mathbf{T}_{n-1}\right]\Psi_{n-1} = 0, \tag{3.7}$$

Where

$$\mathbf{T}_n = -\frac{h^2}{12}\,\mathbf{W}(r_n) \tag{3.8}$$

to "renormalize" the algorithm, a matrix is defined:

$$\mathbf{F}_n = \left[\mathbf{I} - \mathbf{T}_n\right]\Psi_n, \tag{3.9}$$

which substituted to the previous equation gives:

$$\mathbf{F}_{n+1} - \mathbf{U}_n \mathbf{F}_n + \mathbf{F}_{n-1} = 0, \tag{3.10}$$

where

$$\mathbf{U}_n = \left(\mathbf{I} - \mathbf{T}_n\right)^{-1} \left(2\mathbf{I} + 10\mathbf{T}_n\right). \tag{3.11}$$

Next, the ratio matrix is defined

$$\mathbf{R}_n = \mathbf{F}_{n+1}\, \mathbf{F}_n^{-1}, \tag{3.12}$$

To obtain the two-term basic relation:

$$\mathbf{R}_n = \mathbf{U}_n - \mathbf{R}_{n-1}^{-1}. \tag{3.13}$$

To calculate the S-matrix, for large r:

$$\mathbf{F}_n = \mathbf{j}(r_n) + \mathbf{n}(r_n)\, \mathbf{K}, \tag{3.14}$$

which leads to the reactance matrix

$$\mathbf{K} = -\Big[\mathbf{R}_N \mathbf{n}(r_N) - \mathbf{n}(r_{N+1})\Big]^{-1} \Big[\mathbf{R}_N \mathbf{j}(r_N) - \mathbf{j}(r_{N+1})\Big]. \tag{3.15}$$

Which is related to the scattering matrix, as shown in 1.21. This is an efficient and stable method of solving numerically the Schrödinger equation (with an error of order $O(h^6)$) and extracting key observables, like the scattering length.

3.3 Results

This section provides preliminary outcomes of calculations using the methods disclosed above. First, figure 3.3 shows positions of bound states of the He+Li molecule expressed in terms of real and imaginary parts of energy. Two things are apparent: some weakly bound states are purely real, and bound state density increases with proximity to the dissociation threshold, which is an expected behaviour.

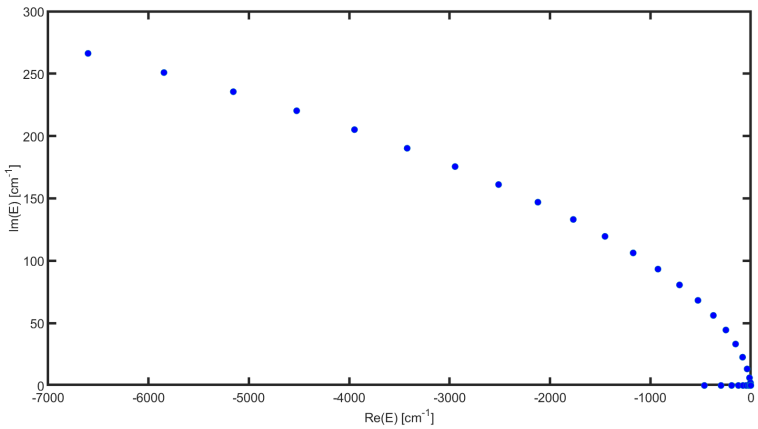

Fig. 3.3: Complex bound states of $He - Li$ molecules. The X-axis shows the real binding energy. The y-axis presents the imaginary energy, given by $E_{im} = -\frac{i}{2}\Gamma$.

E [cm^{-1}]	Lifetime [s]
−5.733e−2	−7.613e−12
−1.310e−1	−4.205e−9
−8.222e−2	−5.467e−9
−6.933e−2	−2.156e−5
−6.596e−2	−3.124e−6
−6.037e−2	−7.572e−7
−5.255e−2	−2.361e−7
−4.257e−2	−8.432e−8
−2.023e−2	−5.482e−9
−2.560e−2	−1.413e−8
−3.043e−2	−2.787e−8
−2.881e−2	−6.502e−8
−1.614e−2	−1.364e−8
−1.276e−2	−2.972e−9
−1.229e−2	−5.442e−7
−9.057e−3	−2.175e−8
−3.658e−3	−1.594e−9
−3.033e−3	−1.436e−8

Table 3.1: Calculated lifetimes of weakly bound complex states of $He - Li$.

Energy thresholds and bound states associated with them are displayed in plot 3.4. This is vital, as Feshbach resonances occur when a higher bound state of one channel approaches energetically an open channel's threshold [75]. The crossings allow for resonance position prediction, which is used in further simulations. Some avoided crossing behaviour is also noticeable in the bound state patterns [163].

For near-threshold complex bound states, lifetimes have been calculated using the relation 3.5 and formula 3.16. Energies and lifetimes are presented in Table 3.1

$$\tau = \frac{\hbar}{\Gamma} \tag{3.16}$$

Panel 3.5 exhibits the evolution of the wavefunction using the renormalized Numerov method meeting the boundary conditions introduced in the previous chapter. Real and imaginary values are plotted separately. The real part of the wavefunctions starts propagating early on, with rapid fluctuations in the range of the potential well, then proceeds to propagate freely in the open channel. The imaginary component, on the other hand, arises later on and converges to oscillate with a relative phase shift of around 110^o, which is close to $\pi/2$, in relation to the real part. Lastly, chart 3.6 exemplifies a resonance, with a distinct pattern in real and imaginary scattering length, obtained with his method. The exact numerical values shouldn't be overemphasized, as they serve as a mere illustration of the method's potential. The resonance is visibly decaying, explained by the strong coupling between open and closed channels.

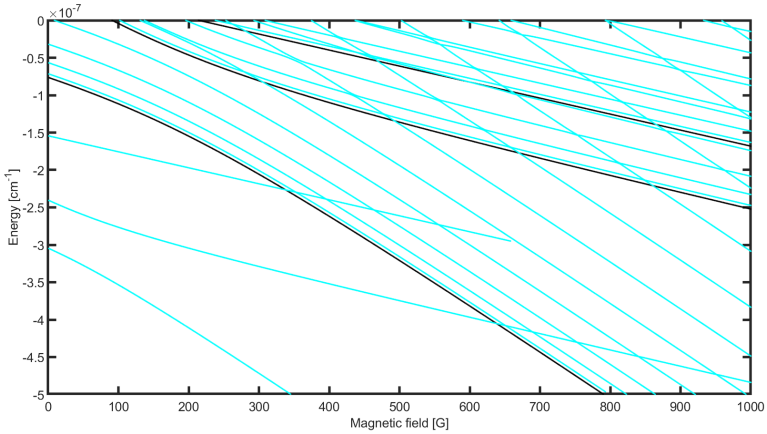

Fig. 3.4: Threshold energies (black) and corresponding bound states (cyan) of $He + Li$ presented as a function of magnetic field.

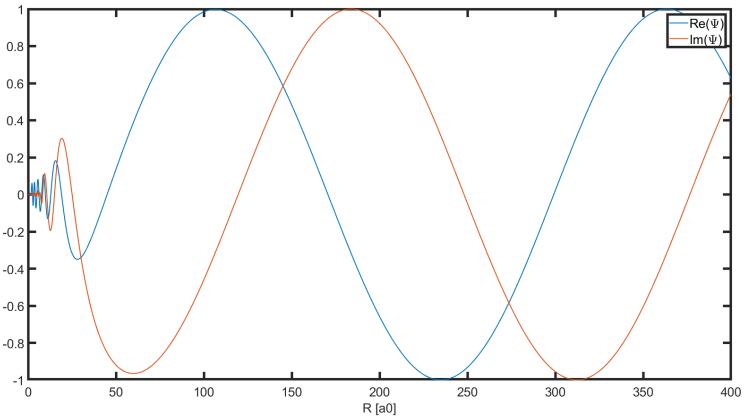

Fig. 3.5: Propagation of the wavefunction of an open channel of the $He + Li$ molecule. Real and imaginary parts of the complex wavefunction are displayed separately.

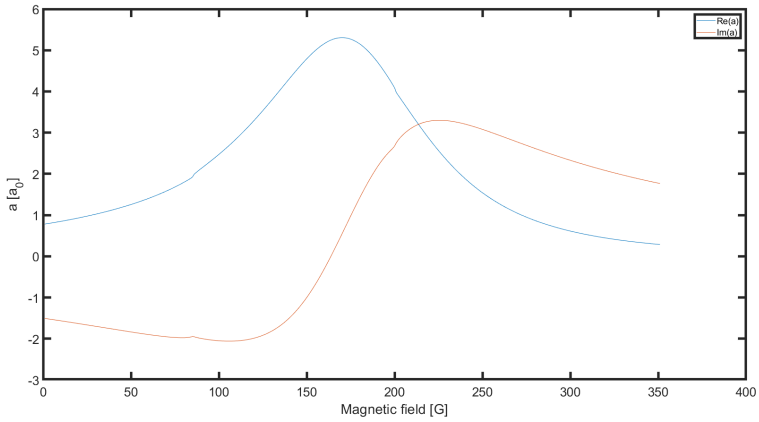

Fig. 3.6: Real and imaginary parts of the scattering length in the vicinity of a Feshbach resonance.

3.4 Chapter summary

In this chapter, a summary of experimental and theoretical research regarding autoionization processes and their role in molecular formation was presented. He+Li molecules, with their relatively simple structure, tunability, and successful ultracold experiments conducted in the past, were highlighted as a promising benchmark for further studies. An overview of theoretical methods for calculations involving complex potentials to model optically-induced ionization processes was given. A Feshbach resonance was identified with the implemented method. The resonance exhibits a strongly decaying nature related to its coupling to the continuum. The results provided are exploratory and serve as a basis for further work.

CHAPTER 4

Ultracold Collisions of Lithium and Erbium

4.1 Introduction do Li+Er

Collisions of ultracold lithium and erbium are of our particular interest. Lithium atoms are well-studied and lightweight, and their non-zero nuclear spin and magnetic moment provide relatively simple hyperfine structure. Ground-state Li+Er molecules have both magnetic and electric dipole moments, allowing for tunable Feshbach resonances and magnetoassociation of the molecules. Li+Er spectra are less congested and less chaotic than those of heavier atoms [164], and the great mass discrepancy between erbium and lithium puts this system in favour of researching Efimov physics or studying time variation of physical constants. The Li+Er system offers significant tunability, where both elements can serve as either bosons or fermions. The fermionic and bosonic lithium atoms possess distinctly different hyperfine structures, resulting in a Feshbach spectrum that varies considerably.

The efforts in cooling highly-magnetic species resulted in obtaining Bose-Einstein condensation in erbium [10], which was followed by Ferilaino's team's impactful experiment [107], in which they studied Feshbach resonances in erbium molecules and confirmed their chaotic nature, which was generally studied before by J. Bohn [106]. A similar approach was employed by Kosicki et al in their theoretical studies on resonances in the Er+Yb system [110]. They showed that while in both systems anisotropic couplings are responsible for Feshbach resonances, in the heteronuclear Er+Yb system, their pattern is more sparse and less chaotic. Theoretical studies of the Li+Er dimers were performed by Maykel González-Martínez and Piotr S. Żuchowski- they analyzed tunable Feshbach resonances in the ground state and calculated resonance spectra in a magnetic field of up to 1000 G.

Lithium-erbium molecules were the subjects of experiments led by Y.Takahashi [165, 166], which confirmed tunability in various isotopes despite high mass asymmetry between the atoms. Recently, erbium was the focus of Ferlaino's experiments involving optical tweezers [167], while Kalia's team incorporated sympathetic cooling in Li+Er molecules [168]. Comparable experimental methodology was adopted by Xie et al. in [169], where they studied Feshbach resonances in another similar system of high mass imbalance- Li+Dy mixtures.

A key application of the Li+Er system is in mixed quantum simulators that incorporate two different particle types, potentially facilitating the investigation of important problems in condensed matter physics, e.g., help model the Kondo effect, its competition vs RKKY, pairing of fermions [170, 171, 172], or other impurity-related problems. This is particularly noteworthy because the large mass imbalance can mimic the pairing of *dressed* electrons exhibiting different effective masses within periodic potentials.

An "ideal" simulator lets one tune interactions without sacrificing stability. In Li+Er,

anisotropy-induced coupling (from Er's orbital angular momentum and large magnetic moment) generates the dense, mostly narrow interspecies resonance structure, while selected broader resonances provide practical tuning knobs. Theory anticipated this pattern—and even emphasized that Li+Er should be less chaotic than lanthanide–lanthanide systems—making Li+Er a promising gateway to paramagnetic, polar molecule formation as well. Altering the quantum state of one of the species could yield intriguing implications. First of all, the position of resonances will change once we change either of the atoms. The Zeeman shifts will be different, and the crossing points of bound states coupled to the continuum will be different. Secondly, for fermionic atoms, a change of states might produce a very interesting case of a mixture where there exists one kind of fermion with a unique mass and two particles of the same mass in two different hyperfine states, which is essentially a 3-compound mixture. In a similar manner, one can envision a heavy boson mixture with two different light fermions of a bosonic Li bath with heavy fermions represented by Er in whatever hyperfine states.

The main problem addressed by this part of the thesis can be briefly stated as "Are these resonances lossy?". At the two-body level, a Feshbach resonance is "lossless" if no energetically lower hyperfine channel is available; then the scattering length has a real pole and intrinsic 2-body decay is absent. Lack of 2-body loss also means that quasi-bound states that produce given resonances have infinite lifetime. If an inelastic channel opens, the scattering length becomes complex and the resonance acquires a finite two-body lifetime Breit–Wigner in energy, by analogy with optics, 'dispersive' versus magnetic field. In Li+Er mixtures prepared in their absolute ground state, measured losses near interspecies resonances are dominated by three-body recombination rather than two-body decay—i.e., lifetimes remain compatible with spectroscopy and tuning protocols at resonance fields. In the ^{167}Er–^{6}Li Fermi–Fermi mixture, decay curves fit an Er–Li+Er three-body model, with coordinated loss of both species; single-species controls show no loss, supporting the three-body interpretation. These data make a clear case that broad, usable interspecies resonances can be long-lived when entrance channels are chosen wisely.

This chapter also addresses the question of whether Feshbach resonances in excited states are useful. For fermionic ^{6}Li, the Feshbach resonances are among the most powerful tools in manipulating their attraction and repulsion. Since the fermion cannot collide in the *s*-wave due to the Pauli exclusion principle, to observe the interaction in the ultracold regime, one has to transfer them to the first excited Zeeman state (let us denote it as $|2\rangle$) from the ground state ($|1\rangle$). Today, the mixture of fermionic Li atoms remains one of the most used mixtures in quantum simulations of few- and many-fermion mixtures, due to the very favourable 834 G resonance found in Selim Jochim's group [173]. This resonance, despite one of Li being in an excited state, is lossless, due to the Pauli exclusion principle and energy constraints: it is not possible to decay to the $|1\rangle + |1\rangle$ state at the collision energy below the *p*-wave centrifugal barrier.

4.2 Theory and calculation details

The potential calculated by Zuchowski and González-Martínez using CASSCF and RCCSD(T) methods (interpolated and extrapolated by means of reciprocal kernel Hilbert Space) [164]

was used, following the theory by González-Martínez and Hutson [174]. Hamiltonian in this system can be expressed as explained in 1.8:

$$\hat{H} = -\frac{\hbar^2}{2\mu R^2}\frac{\partial^2}{\partial R^2}R^2 + \frac{\hat{L}^2}{2\mu R^2} + \hat{V} + \hat{H}_{Li} + \hat{H}_{Er} \tag{4.1}$$

$\hat{H}_{Li}$ and $\hat{H}_{Er}$ describe Hamiltonians for isolated lithium and erbium as follows:

$$\hat{H}_{Li} = a_{HF}\hat{i}\cdot\hat{s} + (g_e\mu_B\hat{s}_z + g_j\mu_N\hat{i}_z)B_Z \tag{4.2}$$

$$\hat{H}_{Er} = a_{SO}\hat{l}\cdot\hat{s} + (g_e\mu_B\hat{s}_z + g_L\mu_N\hat{l}_z)B_Z \tag{4.3}$$

Hyperfine and spin-orbit coupling constants and g factors were taken from [162, 175]. The nuclear magnetic moment used was 3.2565, the hyperfine constant 401.752, and the spin-orbit constant -1159.721. Interaction potential V_r is decomposed into functions with well-defined total spin S and spin projections m_S [176] and then are expanded in Legendre polynomials:

$$\hat{\mathcal{V}} = \sum_k P_k(\cos\theta)\mathcal{V}_k(R). \tag{4.4}$$

The term $\mathcal{V}_0(R)$ has the physical interpretation of *orientation* average potential, while $\mathcal{V}_k(R)$ for $k = 2,\ldots,2l$ are the anisotropic potentials. The requirement that k be even stems from the symmetry properties of the anisotropic Er atom.

The anisotropies $k = 2,4\ldots$ can be obtained from the values of the Hund Case (a) potentials using the following transformation [176, 177, 178]

$$\mathcal{V}_k(R) = \frac{2k+1}{2l+1}\sum_{\Lambda=-l}^{l}\frac{\langle l\Lambda k0|l\Lambda\rangle}{\langle l0k0|l0\rangle}V_\Lambda(R). \tag{4.5}$$

For Li–Er interaction $k = 2\ldots8$ for each multiplicity.

The matrix element for the case considered in this paper was derived by Gonzalez-Martinez [177], and they are a generalization of the simpler case of $l > 0$, an atom colliding with a structureless object discussed before by Alexander and coworkers, as well as by Krems and Dalgarno [176] - for the case of collisions in a magnetic field.

Due to erbium's character, the potential is anisotropic and has two spin multiplicities, as presented in 4.1. For most of the computations, just the V_0 and V_2 potential terms were utilized. Notably, in contrast to alkali molecules, the high- and low-spin potentials are separated only by tens of cm^{-1}.

Calculations were performed using MOLSCAT, with additional use of FIELD and BOUND [146, 86]. For resonance fitting, an algorithm by M. Frye and J. Hutson was employed [179, 180]. MOLSCAT calculates scattering lengths by finding solutions to the Schrödinger equation solving the close coupling equations (discussed in 1.17) with the log-derivative method formulated in 1.28.

Frye and Hutson's algorithm converges on the poles of scattering length using the bisection method, taking the results from FIELD as initial boundary parameters for a chosen open incoming scattering channel, and then characterizes the particular resonance

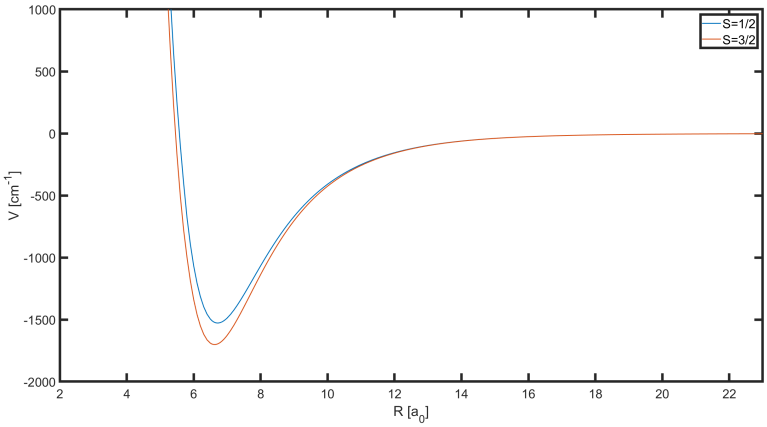

Fig. 4.1: V_0 interaction potential of $Li + Er$ molecule presented for the two spin multiplicities, $S = 1/2$ and $S = 3/2$.

depending on the indicated type: whether it is elastic, weakly inelastic, or strongly decayed. In the elastic case, resonances are fitted to the formula 1.43:

$$a(B) = a_{bg}(1 - \frac{\Delta_B}{B - B_{res}}) \tag{4.6}$$

The close-coupling method employs a variable-step Airy propagator and applies the following boundary conditions: the log-derivative matrix is transformed into its eigenbasis at $r = r_{min}$, and locally closed channels satisfy the condition that they exponentially decay to zero in the classically forbidden regions.

The following parameters were used for calculations: computations are performed on a grid from $r_{min} = 3a_0$ to $r_{max} = 400a_0$ with r_{mid} between $15 - 30a_0$ and $dr = 0.005$. Magnetic field is varied between $0G$ and $1000G$ with a step $dF = 1G$. This range overlaps with one that is given in the paper of Schaffer [165]. Collision energy equaled $E_c = 1e - 7K$.

For FIELD, the matching distance was set to $r_{match} = 20a_0$ and r_{max} reduced to $300a_0$ with no fixed collision energy. For detailed resonance calculations, starting magnetic field values were set to the initial resonance position $+ - 1e - 3G$. ICHAN parameter was set for each selected J_{TOT} to match the ground level with $L = 0$ in a select channel, and IFCONV assumed decaying resonances.

Based on the Hamiltonian's form in 4.1, the basis set for the calculations is constructed as follows. Lithium is characterised by its electron and nuclear spin and their projections. S and i are coupled to total spin f:

$$|(s,i)f, m_f\rangle \tag{4.7}$$

Ground state is labeled with s = 1/2, i = 3/2, f = 1, m_f =1. Erbium, on the other hand, has no nuclear spin, but possesses orbital angular momentum l, and is described by

$$|(s,l)j, m_j\rangle \tag{4.8}$$

In its ground state, the values are s = 1, l = 5, j = 6, $m_j = -6$. Total momentum projection, which is a conserved quantum number, equals -5 in the ground state. Exciting lithium means decreasing its total spin projection to $0, -1$ in the lower f branch, which decreases the resulting m_{tot} to $-12, -14$ in the first two excited states. Excited erbium has increased $m_j = -5, -4...$, which in turn means its states are represented by increased $m_{tot} = -8, -6...$ Lithium and erbium spins couple to $S = 1 - 1/2, 1 + 1/2 = 3/2, 1/2$, which is responsible for the low-spin and high-spin multiplicities of the interaction potential. Positions and behaviour of those states in the magnetic field can be seen on the Breit-Rabi diagram 4.2. Positions of the ground state, first excited lithium and erbium are highlighted. Potential energy adiabatic curves, which include the spin-orbit and hyperfine splittings, are depicted in illustration 4.3. It's worth noting that the profiles are parallel, with a gap of several thousands cm^{-1}, meaning those states could be laser coupled.

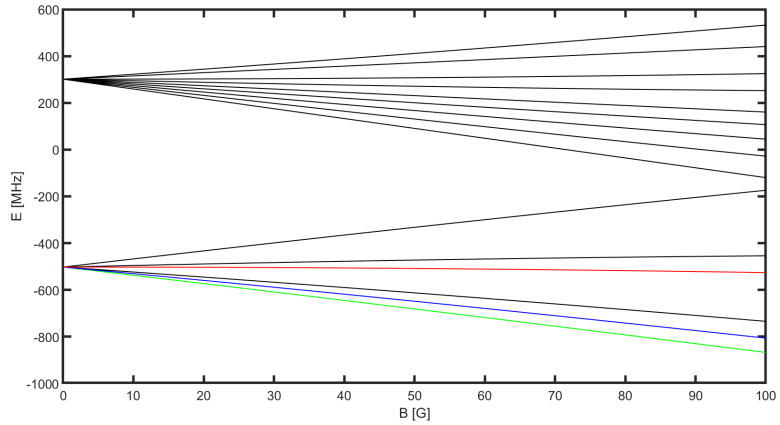

Fig. 4.2: Breit-Rabi diagram of $Li + Er$. Ground state ($m_{tot} = -5$) is highlighted in green. The first excited state of lithium ($m_{tot} = -6$) is marked with blue and the excited erbium ($m_{tot} = -4$) with red colour.

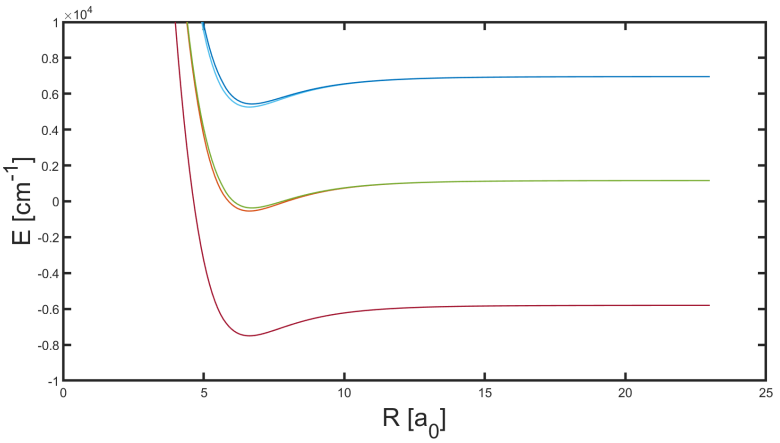

Fig. 4.3: Adiabatic potential energy curves as a function of internuclear distance R for the $Li + Er$ system. Three main branches are separated by the spin-orbit interaction energies.

Another quantum number is the end-over-end orbital angular momentum L_{max}. It describes the molecular rotation and couples different states through its projection, which contributes to the conserved m_{tot}. Higher L_{max} increases the range of states that match

the selected m_{tot}. Thorough calculations were carried out using different basis sets. Resonance number converged for $L_{max} = 6$, and it was included in the basis used for most calculations. Comparison of different values of L_{max} is represented in the panel 4.4.

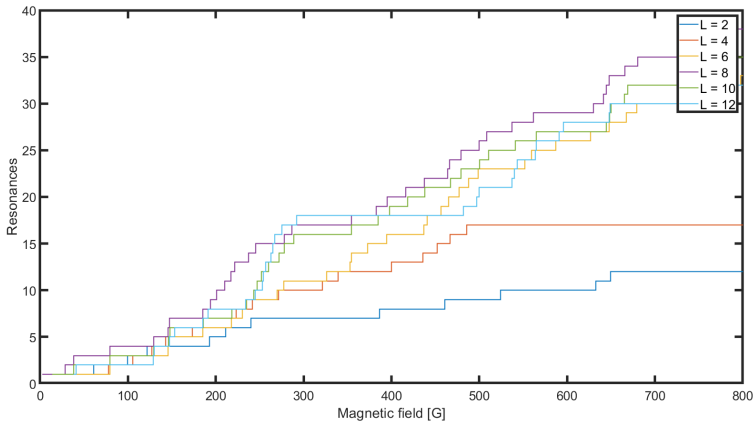

Fig. 4.4: Staircase function of resonance density in the ground state for different values of L_{max} in the basis set. Numerical convergence was reached for $L_{max} = 6$.

Sensitivity of the results to the potential was examined in detail. Scattering length follows patterns described by Gribakin and Flambaum's formula [103, 181]. The scattering length varies periodically as the potential is scaled. While the interaction can be arbitrarily scaled, physically reasonable values must be assumed. V_0 was scaled in order to reproduce the resonance positions measured by [165]. First, scattering length was calculated on a coarse grid in a wide range of scaling factors, which was followed by more precise computations for a single range of its values, as pictured in 4.5, separately for both multiplicities of the V_0 potential. Resulting values were normalized to $\bar{a} = 37.3a_0$, the mean scattering length, determined by asymptotic behaviour of the potential [103, 75].

Next, for select values of scaling factors, additional calculations were conducted, with V_0 low-spin and high-spin being scaled on a two-dimensional grid. As displayed in 4.6, for lower L_{max} in the first panels, a clear resonance pattern is visible. However, this becomes less regular with increasing end-over-end rotations, which is an important conclusion from this analysis. For $L_{max} = 2$, additional ridges are visible in the plot, and for $L_{max} = 4$ or higher, no distinct structure can be identified. In the final panels, the distances on the x and y axes are expressed in terms of the scattering length obtained in one-dimensional potential scaling. Ultimately, the calculations for this system were performed with an unscaled potential.

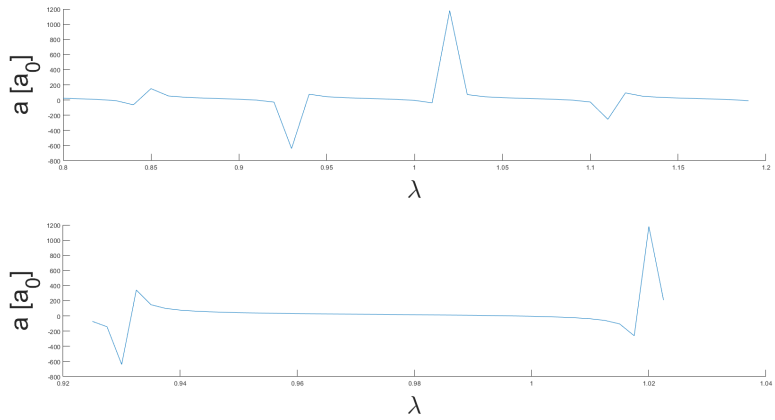

Fig. 4.5: Scattering length as a function of interaction potential scaling. The top panel depicts a scan across a wider range of scaling factors. The bottom panel presents results for further calculations with an increased resolution.

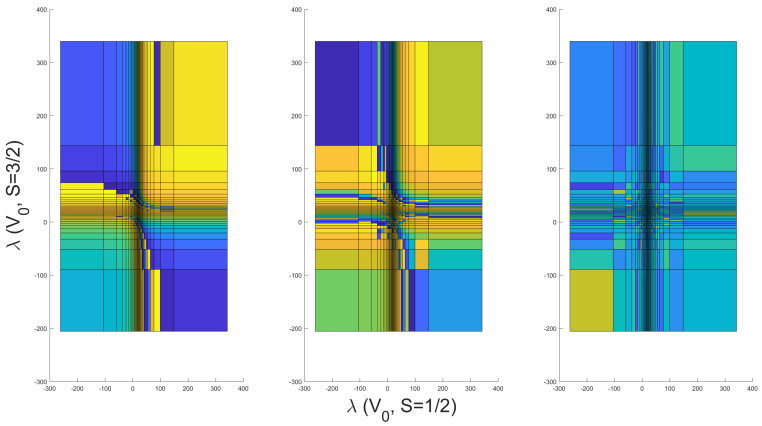

Fig. 4.6: Results of 2-D potential scaling. Horizontal axis corresponds to the low-spin scaling factors, and the vertical axis to the high-spin scaling factor λ. Leftmost panel presents results for $L_{max} = 0$, middle one for $L_{max} = 2$ and rightmost one for $L_{max} = 4$. Distances along each axis are scaled to the values of scattering length obtained from 1-D scaling calculations. Results are normalized to $\bar{a}$.

4.3 Results

In this chapter results of calculations in this system are presented. The following subsections discuss Feshbach resonances in ground and excited states, the influence of potential and reduced mass scaling on scattering length and bound state positions in a magnetic field. The last two subsections are dedicated to showing differences between excited erbium and lithium states and a linear model of resonance positions.

4.3.1 Feshbach resonances in ground and excited channels

First, let us discuss the case of the ground state of lithium-erbium molecules. This is the state associated with $m_{tot} = -5, m_f = 1, m_j = -6$. Results of scattering length calculations are shown in fig. 4.7. Noticeably, the scattering length is a real number in this case. As could be expected, resonances are lossless- molecules in the lowest state have no lower states to decay into. Detailed resonance positions B_C, resonance widths Δ, and real background scattering lengths are shown in Table 4.1. No values of resonant scattering lengths were calculated, since in the case of real resonances, they diverge to infinity. The resonance spectrum exhibits a moderate density with 26 resonances, some of which are clustered together.

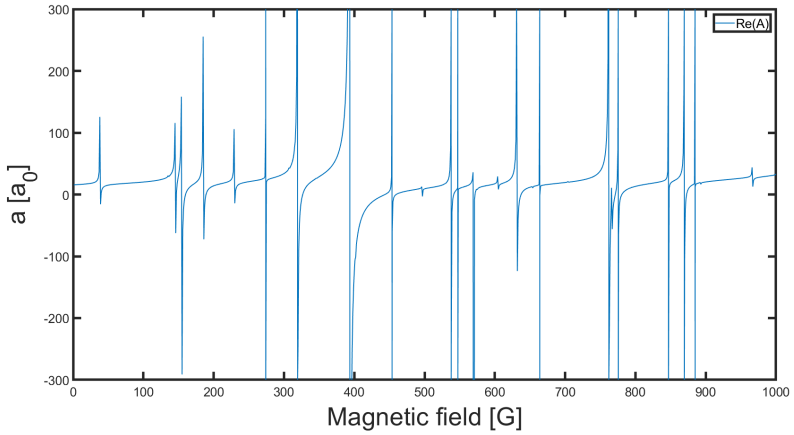

Fig. 4.7: Scattering length as a function of magnetic field. Results for the ground state ($m_{tot} = -5$, $m_J = -6$, $m_F = +1$).

Next, graph 4.8 presents the results of first excited erbium state related with $m_{tot} = -4, m_f = 1, m_j = -5$. The resonance pattern here is clearly visible, with the scattering length oscillating irregularly from high negative values to high positive values. The spectrum is sparser, with fewer resonances than in the ground state. Many resonances show partial overlap. The scattering length reaches very high values for some resonances, while others remain moderate. Particularly notable are the results of the imaginary part of the scattering length. Most resonances are complex, some with moderate, some with very high values of imaginary scattering length. As mentioned before, the imaginary scattering length visibly suppresses resonances [3]. Positions of peaks in the imaginary part match positions of poles in the real part, true to the expected behaviour. A complete set of results, including resonance positions, real and imaginary parts of resonant

B_C	a_{BG}^{RE}	Δ
966.48	28.77	0.27
884.79	16.73	0.05
869.45	20.49	3.29
846.98	18.07	0.53
775.48	5.59	5.6
762.09	22.62	9.62
704.23	19.90	0.02
663.89	15.64	0.11
653.93	12.91	0.01
631.32	15.82	6.01
604.43	17.12	0.3
574.69	9.64	0.05
569.99	13.64	1.65
547.26	8.62	0.07
537.81	-90.9	-0.59
496.79	9.86	0.27
453.68	3.11	5.54
393.67	18.77	45.65
319.26	27.75	7.3
274.05	24.76	0.2
229.28	19.27	1.25
185.27	16.71	3.84
154.68	18.07	5.32
145.52	32.15	1.38
135.14	28.56	0.01
38.23	16.46	1.5

Table 4.1: Detailed results of resonance fitting for the ground state ($m_{tot} = -5$).

and background scattering lengths as well as inelastic contribution to resonance width Γ along with width Δ, is presented in table 4.2.

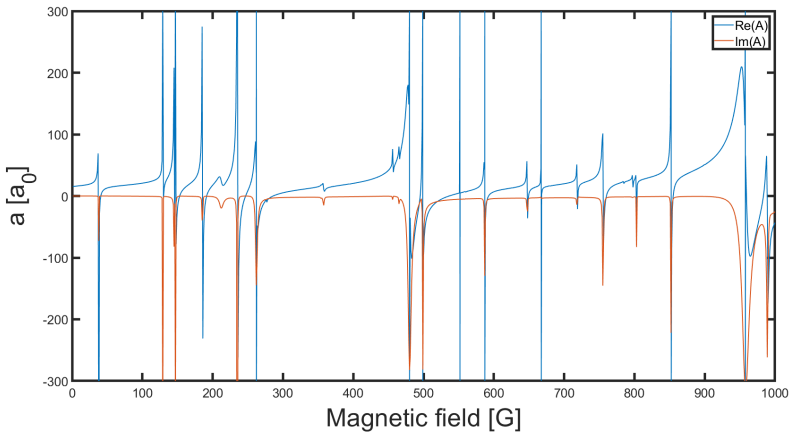

Fig. 4.8: Scattering length as a function of magnetic field. Results for the first excited erbium state ($m_{tot} = -4$, $m_J = -5$, $m_F = +1$).

Plot 4.9 depicts the scattering length in the second excited erbium state, with quantum numbers $m_{tot} = -3, m_f = 1, m_j = -4$. The spectrum here has a regular cluster of resonances in low field and a few, widely spaced resonances in higher field. In a low field, the scattering length has finite, complex values. In the higher field, however, broad, complex resonances overlap with peaks of narrow and sharp real resonances. High values of background scattering length across a wide range of magnetic fields. Exact tabular results are provided in 4.3

Plot 4.10 and table 4.4, on the other hand, present data for the first excited lithium

B_C	a_{BG}^{RE}	a_{BG}^{IM}	a_{RES}^{RE}	a_{RES}^{IM}	Γ_{inel}	Δ
989.33	-21.46	-30.16	234.32	-68.64	-1.94	-10.59
957.68	21.30	-2.84	309.88	60.16	-12.65	92.04
852.22	34.32	-0.89	450.96	18.25	-0.45	2.94
802.95	25.34	-1.28	123.77	-3.10	-0.14	0.34
797.63	26.60	-1.43	96.47	-5.33	-0.10	0.18
784.66	22.69	-1.48	140.18	-4.80	-0.01	0.04
755.36	22.75	-2.00	193.46	-12.61	-1.13	4.79
667.29	15.20	-3.01	573.30	58.97	-0.03	0.57
647.56	14.94	-3.23	133.95	-3.48	-0.40	1.78
587.08	10.18	-4.09	132.01	6.93	-0.83	5.38
559.61	7.02	-4.85	39.02	-15.37	-0.02	0.05
551.72	4.94	-5.24	75.35	38.70	-0.00	0.04
498.80	-16.18	-12.08	282.74	98.37	-0.79	-6.91
479.98	14.51	-3.05	278.84	50.13	-5.46	52.45
465.34	67.89	-5.05	27.28	-0.98	-0.47	0.09
456.26	48.18	-0.56	243.62	-16.93	-0.06	0.16
394.75	19.53	-1.20	179.92	-8.77	-0.00	0.01
357.87	14.68	-1.83	13.98	-1.97	-1.67	0.80
276.65	-6.54	-5.15	12.59	-3.09	-0.21	-0.20
262.12	6.68	-2.10	145.78	17.34	-2.44	26.67
235.06	22.91	-0.71	1758.6	-76.38	-0.29	11.09
213.89	31.06	-8.67	7.81	-13.33	-7.00	0.88
185.49	21.99	-0.70	1984.4	-45.80	-0.13	5.76
129.04	28.21	-0.98	610.49	-23.86	-0.10	1.11
37.91	16.45	-0.03	3720	-20.55	-0.03	2.92

Table 4.2: Detailed results of resonance fitting for the first excited erbium state ($m_{tot} = -4$).

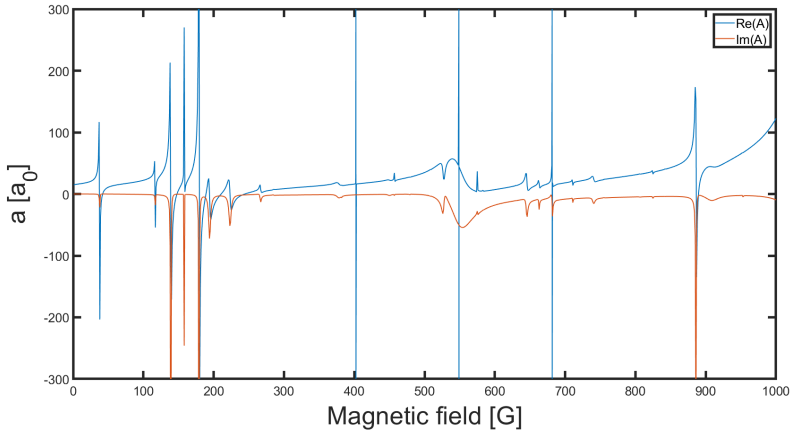

Fig. 4.9: Scattering length as a function of magnetic field. Results for the second excited erbium state ($m_{tot} = -3$, $m_J = -4$, $m_F = +1$).

B_C	a_{BG}^{RE}	a_{BG}^{IM}	a_{RES}^{RE}	a_{RES}^{IM}	Γ_{inel}	Δ
952.81	67.13	-2.76	2.64	3.21	-0.24	0.00
886.18	49.75	-4.38	423.82	-64.84	-0.82	3.50
824.66	35.81	-4.27	9.18	1.41	-0.39	0.05
754.75	23.84	-6.74	-0.89	-0.55	-2.51	-0.05
681.46	15.96	-8.70	24.63	33.49	-0.96	0.74
548.79	16.78	-6.14	44.01	27.82	-34.05	44.65
479.22	27.56	-0.52	0.80	-0.82	-0.60	0.01
457.18	22.50	-0.71	83.19	-1.00	-0.05	0.10
402.30	16.23	-1.40	32.53	8.97	-0.01	0.01
381.97	13.72	-4.46	0.64	3.12	-0.05	0.00
377.95	15.56	-1.73	4.61	1.03	-7.11	1.05
194.64	6.25	-5.32	63.85	-30.70	-2.69	13.76
158.03	18.45	-0.67	500.89	2.55	-0.06	0.81
138.97	24.90	-1.14	619.20	-46.46	-0.68	8.48
37.69	16.06	-0.07	2028.1	-21.78	-0.07	4.32

Table 4.3: Detailed results of resonance fitting for the second excited erbium state ($m_{tot} = -3$).

state, described with $m_{tot} = -6, m_f = 0, m_j = -6$. A regular, dense pattern of well-spaced resonances is noticeable. While a real background scattering length is present, the resonances are pronounced with distinct peaks. Most resonances are purely real, with some resonances of high values of imaginary scattering length, which otherwise is almost nonexistent. Plot 4.11 illustrates values of scattering length for the second

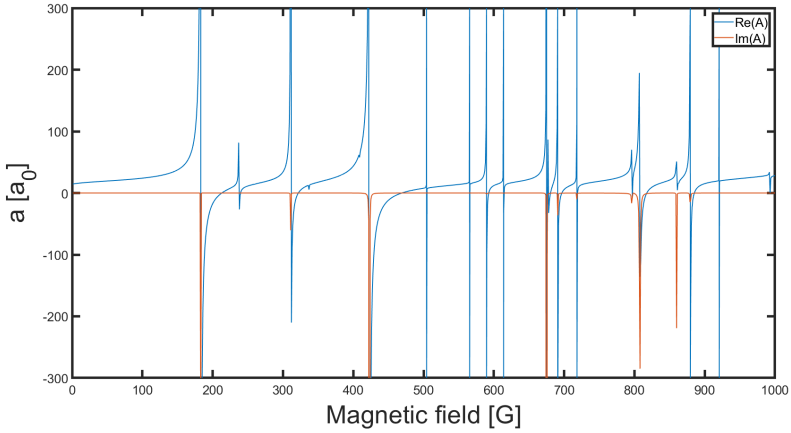

Fig. 4.10: Scattering length as a function of magnetic field. Results for the first excited lithium state ($m_{tot} = -6, m_J = -6, m_F = 0$).

B_C	a_{BG}^{RE}	a_{BG}^{IM}	a_{RES}^{RE}	a_{RES}^{IM}	Γ_{inel}	Δ
992.83	28.07	-0.00	1393	0.15	-0.01	0.18
920.50	19.68	-0.01	8344.5	19.09	-0.00	0.01
879.45	18.77	-0.01	3587.1	17.33	-0.06	5.73
860.01	23.21	-0.06	222.67	0.33	-0.17	0.81
807.72	19.77	-0.02	368.53	-2.38	-1.05	9.79
796.55	37.12	-1.34	144.34	-26.40	-0.29	0.57
718.12	13.97	-0.10	820.77	17.36	-0.03	0.87
690.79	12.75	-0.08	3685.9	32.22	-0.04	5.73
675.03	19.85	-0.04	3138.1	11.96	-0.07	5.92
613.81	15.53	-0.01	5578.2	14.26	-0.00	0.54
589.54	16.07	-0.01	8072.5	14.72	-0.01	3.18
422.98	15.18	-0.01	12194	8.43	-0.12	46.73
565.51	16.03	-0.00	25117	22.41	-0.00	0.08
504.24	8.16	-0.02	1.5775e+05	100.69	-0.00	0.15
336.99	12.89	-0.00	191.74	-0.16	-0.00	0.00
311.12	18.63	-0.00	46108	-7.86	-0.01	10.66
237.34	10.76	-0.00	1.4089e+05	-3.40	-0.00	2.26
183.02	21.46	0.00	2.3789e+06	20.82	-0.00	29.51

Table 4.4: Detailed results of resonance fitting for the first excited lithium state ($m_{tot} = -6$).

excited lithium state of quantum numbers $m_{tot} = -7, m_f = -1, m_j = -6$. The plot presents a coarse structure of semi-regular, widely spaced resonances of narrow, well-defined peaks. Just a few of them have an imaginary compound of high magnitude. In the high range of magnetic field, there's a cluster of complex, overlapping resonances. In the low field, there's a distinct feature in the scattering length: values don't change sign between two resonances, rather just approach zero and rise back up. This is probably due to the fact that in this range energies in the Breit-Rabi diagram behave nonlinearly, and a single bound channel may approach a threshold twice on a bending part- once crossing from below, once from above. All results are included in tab 4.5.

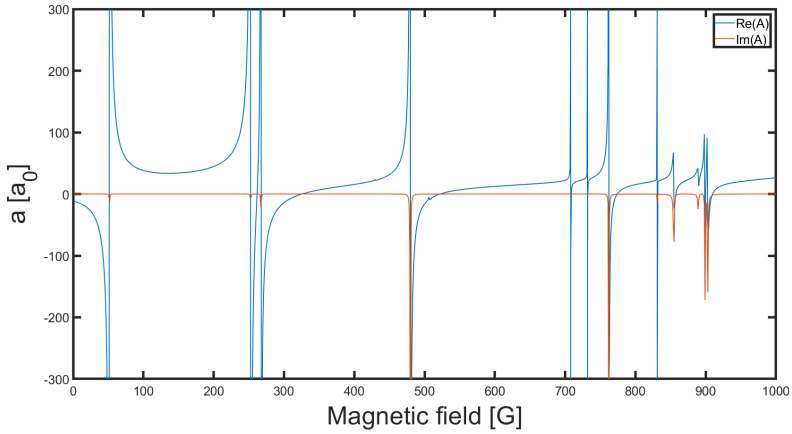

Fig. 4.11: Scattering length as a function of magnetic field. Results for the second excited lithium state ($m_{tot} = -7, m_J = -6, m_F = -1$).

B_C	a_{BG}^{RE}	a_{BG}^{IM}	a_{RES}^{RE}	a_{RES}^{IM}	Γ_{inel}	Δ
951.50	20.46	-0.07	2.17	-0.58	-0.19	0.01
902.83	13.81	-1.65	175.77	-10.49	-1.08	6.88
898.87	49.62	-7.36	230.46	-16.50	-0.44	1.03
889.45	33.14	-1.67	29.71	-10.23	-1.12	0.50
854.68	22.24	-0.33	98.71	-8.98	-1.37	3.03
830.91	21.61	-0.40	86.33	11.24	-0.07	0.14
762.20	19.36	-0.09	2183.5	20.31	-0.21	11.96
731.81	24.54	-0.00	25898	13.47	-0.00	0.26
707.84	21.04	-0.01	3899	10.66	-0.01	0.84
638.49	15.19	-0.01	88.67	2.13	-0.01	0.02
479.75	13.95	-0.01	6885.8	10.74	-0.17	42.82
506.22	-8.86	-0.12	1125.6	8.34	-0.00	-0.11
429.21	21.94	-0.00	3514.6	-3.72	-0.00	0.02

Table 4.5: Detailed results of resonance fitting for the second excited lithium state ($m_{tot} = -7$).

4.3.2 Potential and mass scaling

While most calculations in this chapter were performed without scaling the interaction potential, this subsection covers the results of scaling the potential and its influence on resonances. All data here relate to the ground state. Base outcomes of regular, non-scaled potential have been shown in fig. 4.7. The premise is that results are sensitive to interaction potentials, and the goal is to observe this impact. Cycles of scattering length have been observed and analyzed before, as shown in 4.5. Potential scaling factors were chosen based on those results for V_0 potentials. One scaling factor was chosen to shift the scattering length to values around zero, i.e., to the middle of the cycle, and another to shift the values towards extrema near the peaks. Factors were chosen separately for the low-spin and high-spin potential. For doublet potential, the chosen values of λ were 0.9975 and 1.015, whereas for the quartet state, 0.96 and 1.01. Since these are ground-state calculations, all resonant scattering lengths diverge to $\pm\infty$, which may not be accurately depicted due to the limited resolution of calculations.

Figure 4.12 presents the plot for both low and high spin potentials scaled to "low" values. Compared to the average, generally used, non-scaled potential, the spectrum is less crowded, still fairly regular, with few grouped resonances. Figure 4.13 presents results

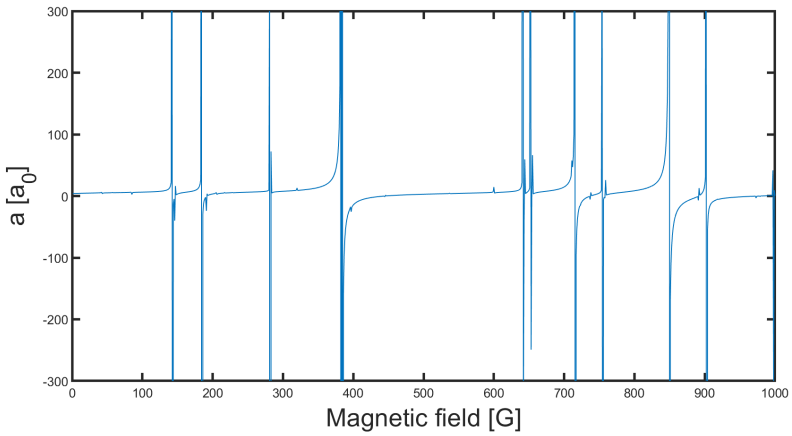

Fig. 4.12: Scattering length plot for the ground state. V_0 potential scaling factors: $\lambda_{1/2} = 0.9975$, $\lambda_{3/2} = 0.96$.

for low-spin scaled to "high" values, with high-spin kept with the same scaling factor. Resonances here are irregular, with some overlapping and clustering. Some resonances are shown as small peaks due to the low resolution of the plot. There are high values of background scattering length with few sharp and wide resonances.

In figure 4.14 an opposite situation is presented: low-spin potential is scaled to "low" values and high-spin to higher values of scattering lengths. It is less regular and sparse than previous plots, but similarly to 4.12, resonances are narrow, sharp, and well visible in otherwise low background scattering length. Lastly, plot 4.15 is a visualisation of the results of calculations with both interaction potential parts being scaled towards increased values of scattering length. The resonance structure is highly irregular, with both a few grouped resonances and a few completely separate ones. Broad resonances overlap with narrow ones, background scattering length has high values across the magnetic field range.

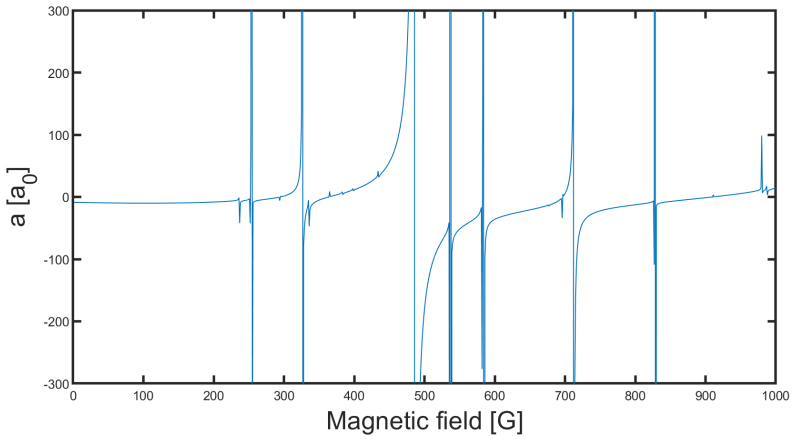

Fig. 4.13: Scattering length plot for the ground state. V_0 potential scaling factors: $\lambda_{1/2} = 1.015$, $\lambda_{3/2} = 0.96$.

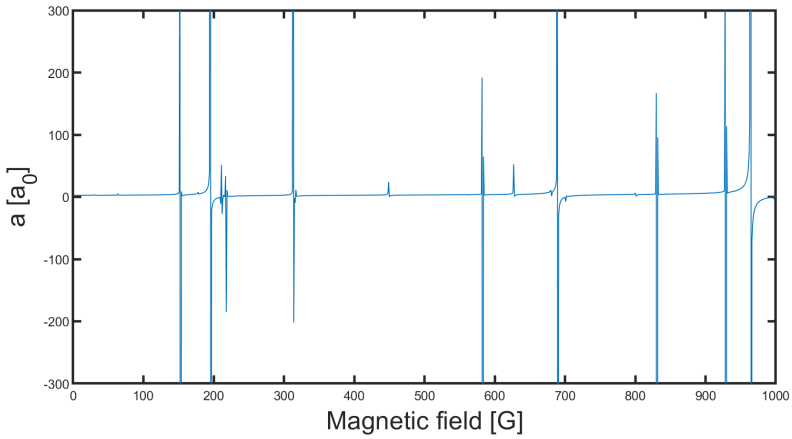

Fig. 4.14: Scattering length plot for the ground state. V_0 potential scaling factors: $\lambda_{1/2} = 0.9975$, $\lambda_{3/2} = 1.01$.

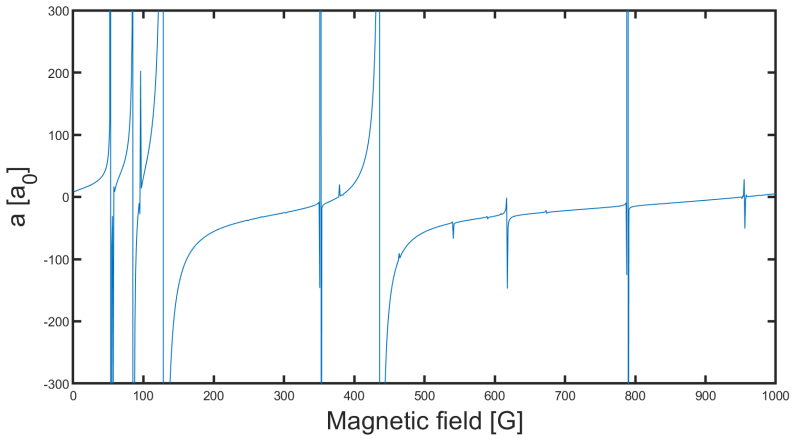

Fig. 4.15: Scattering length plot for the ground state. V_0 potential scaling factors: $\lambda_{1/2} = 1.015$, $\lambda_{3/2} = 1.01$.

Next, the results of V_2 potential scaling are presented. This potential is related to the anisotropy of the system and is responsible for the coupling between resonant states. For these calculations, the isotropic potential was kept at its baseline level, while only V_2 was scaled. Plots 4.16 and 4.17 demonstrate results for the anisotropic potential scaled by factors of 0.5 and 2.0, respectively. Compared to the reference potential (fig. 4.7), decreasing the potential weakens the interactions; the resonance spectrum is quasi-regular and less dense, with few closely-spaced resonances. The total number of resonances is lower, although their density increases with the magnetic field. The next plot shows an inverse situation. Higher potential is responsible for increased coupling between neighbouring states, which opens up more resonance opportunities. The plot is seemingly crowded, with a great amount of closely stacked, sharp, overlapping resonances. Resonance density is much higher, and the peak of the distribution is noticeably shifted towards a lower magnetic field. Resonance patterns are chaotic, and resonant states are composed of many participating channels. Obtained V_2 scaling results align with the generally expected behaviour of scattering length and resonance patterns.

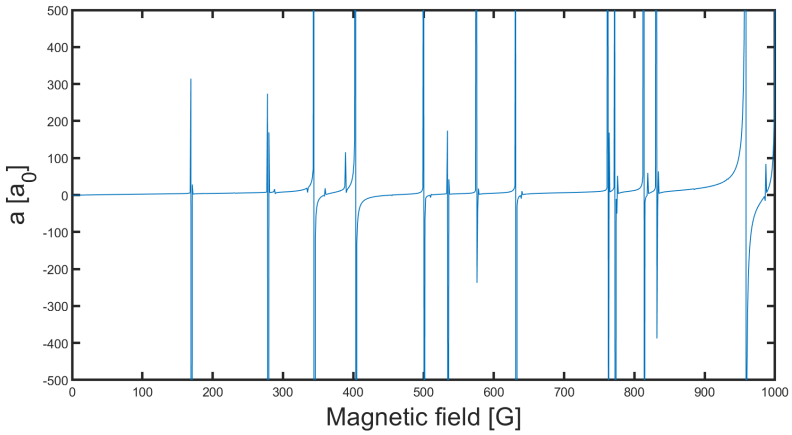

Fig. 4.16: Scattering length plot for the ground state. V_2 potential scaling factor $\lambda = 0.5$.

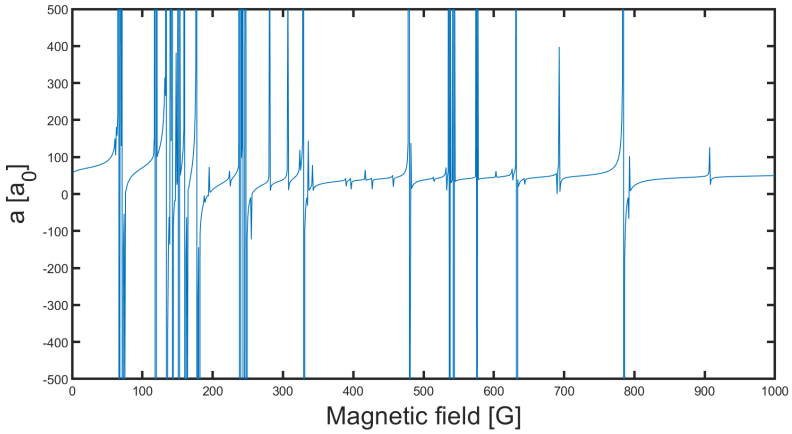

Fig. 4.17: Scattering length plot for the ground state. V_2 potential scaling factor $\lambda = 2.0$.

Finally, in this section, the consequences of scaling the reduced mass itself are discussed. The reduced mass is one of the key properties defining molecular interactions and enters the Hamiltonian in the kinetic energy's denominator, in the centrifugal effect,

and in the Zeeman effect 4.1. Higher reduced mass results in more strongly bound states, and a closer proximity to the threshold causes a higher Feshbach resonance density. As Zeeman energies increase, resonance positions in the external field shift. Another aspect is that wavefunctions of dimers of higher reduced mass oscillate more slowly, and resonances are wider (due to wider overlap of coupled states' wavefunctions). Finally, a larger mass and a slower wavefunction variation extend the period of the scattering length cycle.

Outcomes of reduced mass scaling are presented below. Plots 4.18 and 4.19 show the scattering length of the system with μ scaled by 0.5 and 0.9, respectively. Resonance spectra are sparse, with just a few sharp peaks visible. Figure 4.20 represents a scaling factor of 1.1, and the resulting band presents many fewer resonances than the base one, with a few much wider resonances in a low magnetic field. Lastly, the scattering length of μ scaled by 2 on graph 4.21 has a much denser profile with plenty of both narrow and overlapping wide resonances. The resulting resonances are much more irregular with little recognizable structure.

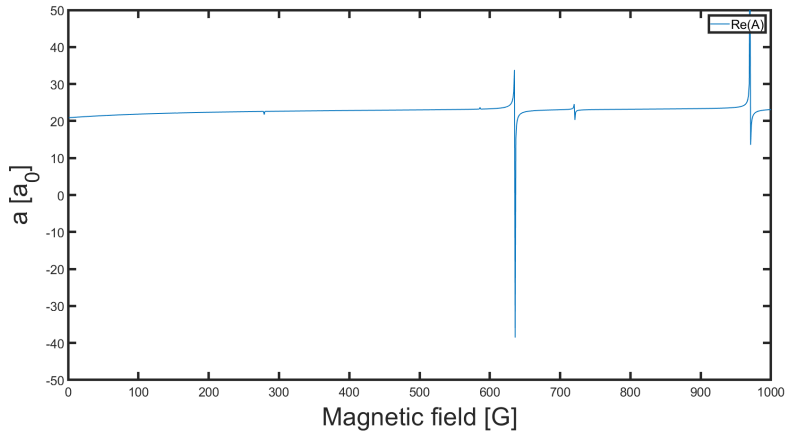

Fig. 4.18: Scattering length plot for the ground state. Reduced mass μ scaled by 0.5.

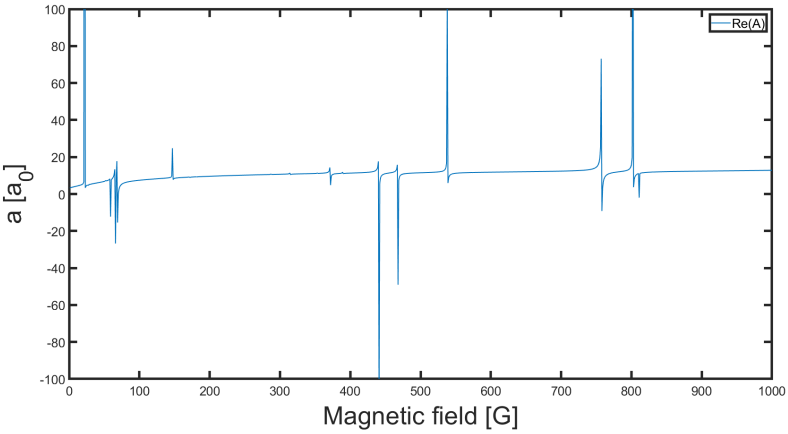

Fig. 4.19: Scattering length plot for the ground state. Reduced mass μ scaled by 0.9.

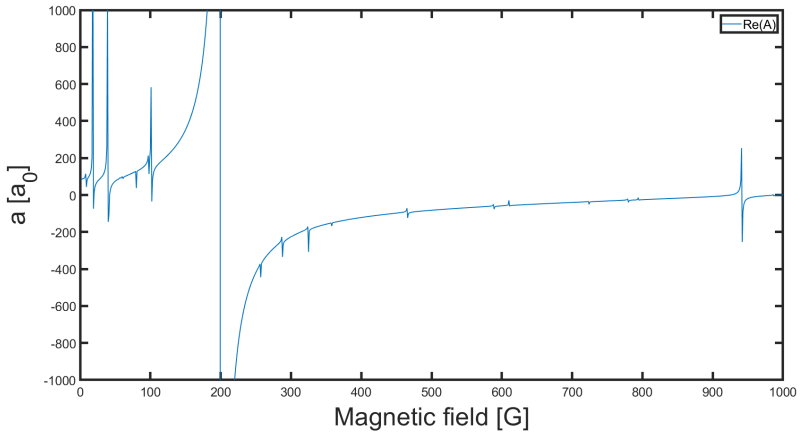

Fig. 4.20: Scattering length plot for the ground state. Reduced mass μ scaled by 1.1.

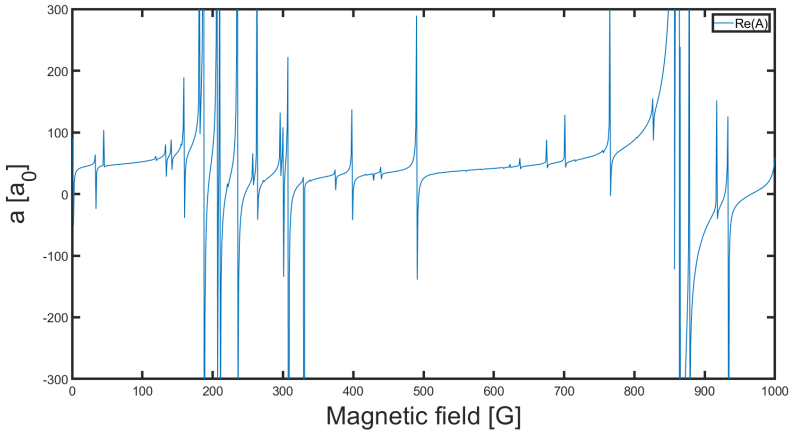

Fig. 4.21: Scattering length plot for the ground state. Reduced mass μ scaled by 2.0.

4.3.3 Bound states in magnetic field

One of the aspects under consideration in the research was the bound states. Calculations were conducted for weekly bound states, lying closely just below the thresholds. Energies ranged from -0.1 K to 0 K with a wide magnetic field scan of 0 to 1000 G. As those states are near-threshold, they are of particular importance, as they are most likely to participate in Feshbach resonances. Figure 4.22 exhibits bound states in the ground state of the molecule. All visible states here are low-field-seeking[38] and their energies slide upwards with magnetic field- until, eventually, they cross the threshold. Some states are parallel, which suggests that they might be higher levels of the same channel. Points where channels cross are an indication of possible Feshbach resonance positions. Notable are areas where states avoid crossing, altering their paths instead. Those anticrossings [162, 163] are owed to small interactions between states of the same m_f, which repel each other.

Figure 4.23 represents bound states corresponding to the first excited erbium. The presented levels show resemblance with the previous case: the positions and paths followed are similar for most of them. There are a few variations, though. There are a few additional bound states, and most lines are less inclined in the magnetic field. This increases the resonance density, and crossing positions drift towards a higher magnetic field. An important feature here is the presence of layers of densely packed bound states in the upper-right section. These are the eigenstates of the potential well itself, manifesting themselves in such a manner. Those virtual bound states are results of the mathematical model and depend on the width and depth of the potential well[182]; they don't have the same physical interpretation as regular bound states. They don't alter the general bound state trajectories, which remain recognizable. Bound states related to the second excited erbium are depicted in the figure 4.25. Those calculations, as numerically costly and time-consuming, were conducted in a lower field range of 200 G. They do, however, illustrate the tendency shown before: additional bound states emerge, with more crossings and Feshbach resonance opportunities.

Plot 4.24, on the other hand, provides results for excited lithium states. Some previous states are absent here, with lesser inclination and higher nonlinearity and many avoided crossings. In the lower magnetic field, they share characteristics with the ground state and the excited erbium. As the magnetic field increases, the patterns change. Some potential well states are also visible here.

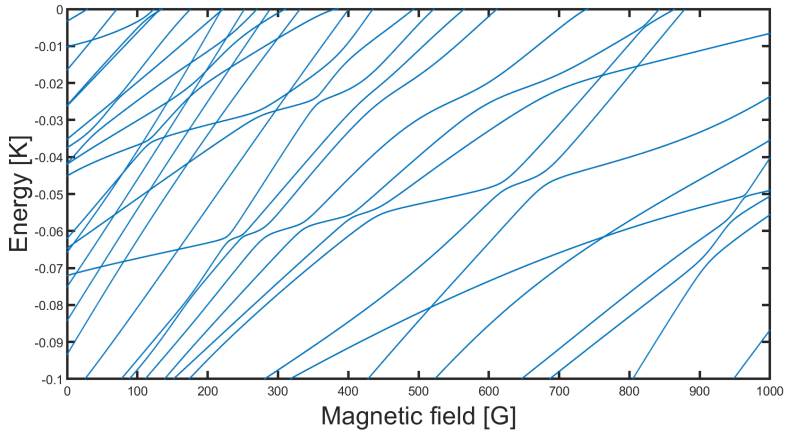

Fig. 4.22: Bound state energies as a function of magnetic field in the ground state ($m_{tot} = -5$).

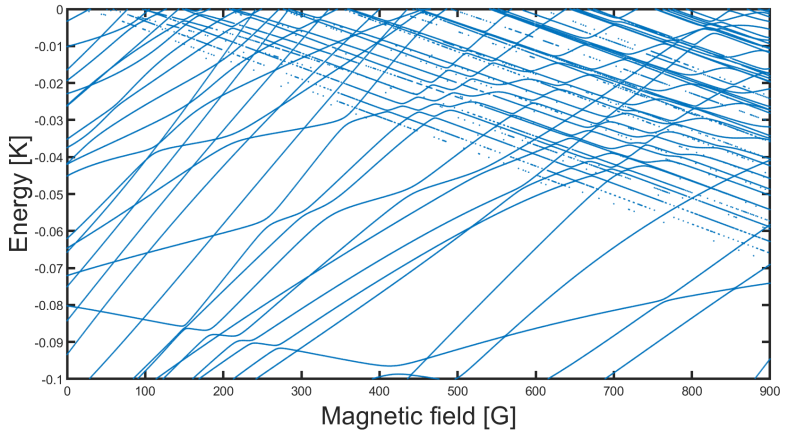

Fig. 4.23: Bound state energies as a function of magnetic field in the first excited erbium state ($m_{tot} = -4$).

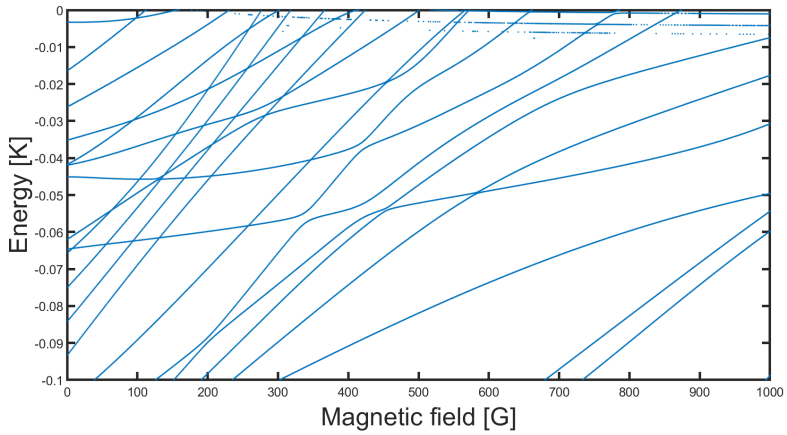

Fig. 4.24: Bound state energies as a function of magnetic field in the first excited lithium state ($m_{tot} = -6$).

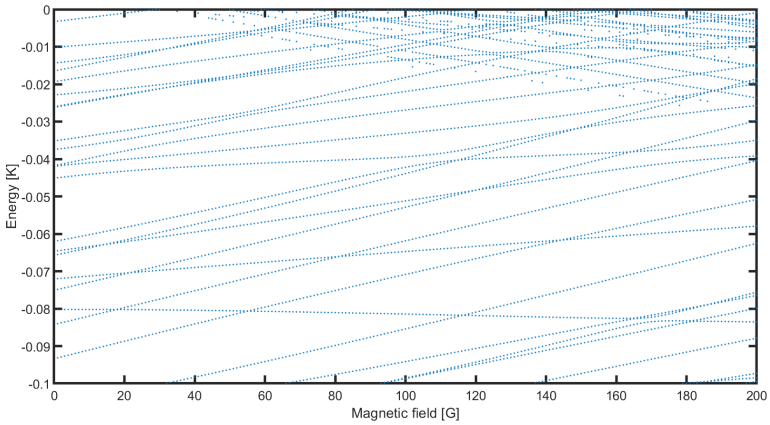

Fig. 4.25: Bound state energies as a function of magnetic field in the second excited erbium state ($m_{tot} = -3$).

4.3.4 Comparing excited lithium and erbium states

This section is dedicated to showing qualitative differences between excited erbium and lithium. As shown in the sections before, the results are different for the states associated with lithium's or erbium's excitations. This is, unsurprisingly, related to different mechanisms causing Feshbach resonances. In lithium's case, they are caused by coupling between low-spin and high-spin states, while erbium's resonances are a result of mixing between matching anisotropies [135]. Thus, the resonances behave differently.

As mentioned before, the imaginary parts of the scattering length are distributed differently in excited resonant states. To distinguish it, an index R is introduced, defined as the ratio of the variance of the imaginary part of the scattering length to that of the real component, calculated for each state separately. As real profiles are comparable, this index emphasizes qualitative differences between imaginary parts. In systems with moderate, but persistent values of imaginary scattering length, the value of R is higher. If imaginary resonances have high values, but are present occasionally, R is lower. Despite very similar mean values of scattering length across systems, this index highlights systematic differences in fluctuations of the compared results. While it is mathematically possible for this formula to have a zero in the denominator, it is implausible as $Re(a)$ would have to be effectively constant.

$$R = \frac{\sum (\mathrm{Im}(a_{res})_i - \mathrm{Im}(\bar{a}))^2}{\sum (\mathrm{Re}(a_{res})_i - \mathrm{Re}(\bar{a}))^2} \tag{4.9}$$

The results are shown in 4.6. There is a clear distinction between results in excited lithium's and erbium's cases- it differs by a few orders of magnitude.

Now, let's see the average resonance widths and lifetimes for each J. To calculate lifetimes, a formula used by [3, 183] is applied:

$$\Gamma_{\mathrm{inel}} = \frac{\hbar}{\tau\, \Delta\mu} \tag{4.10}$$

m_{tot}	R
-3	2.700e−3
-4	2.500e−3
-6	1.362e−9
-7	1.904e−6

Table 4.6: Mean ratio of the variance of imaginary to the real parts of the resonant scattering length for different excited states.

where $\Delta\mu$, an effective magnetic moment, is the rate at which the open channel's threshold energy changes with the magnetic field:

$$\Delta\mu = \frac{dE}{dB} \tag{4.11}$$

which was calculated by numerically differentiating using the two-point difference formula using reference energies for given states in different ranges of magnetic field, one in low field (around 100 G), one in high (1000 G), for a reliable linear approximation (as seen in 1.3). Results are shown in 4.7. Excited erbium's resonances are, on average, wider but with shorter lifetimes than excited lithium's.

m_{tot}	Resonance width [G]	$\Delta\mu$	liftetime [s]
-3	6.450	−2.595e−4	2.001e−7
-4	1.815e1	−3.138e−4	7.019e−7
-6	1.423e1	−3.625e−4	5.507e−5
-7	1.219e1	−3.557e−4	7.218e−6

Table 4.7: Mean resonance widths, magnetic moments, and lifetimes calculated for different excited states.

4.3.5 Matching resonance positions

Feshbach resonances emerge when a bound state intersects with another channel's state at a given energy. We may draw a general diagram showing some bound state energies in a magnetic field. Black lines shown in figure 4.26 correspond to energies of the eigenstate, while dashed lines are energies of higher states associated with a different threshold. Note that those resonant states are a combination of different channels. A scattering channel is highlighted in red, and its crossings with consecutive bound states are marked with dots. Using this simplified representation, we may assume a linear approximation of the state's energies in an external magnetic field. With it, some generalized magnetic moment μ_R could be assigned to the collisional state, which would enable us to extrapolate and predict further crossings. Energy depends linearly on the magnetic field

$$\Delta E = \mu \Delta B \tag{4.12}$$

If bound states labeled with $1, 2...$ with initial $E = 0$ and magnetic moments $\mu_1, \mu_2, ...$ cross the red-marked with initial $E = -E_R$ at energies $E1, E2...$ corresponding to magnetic fields $B1, B2...$, we may notice that

$$-\mu_1 B_1 = \mu_R B_1 - E_R \tag{4.13}$$

$$E_R = B_1(\mu_1 - \mu_R) \tag{4.14}$$

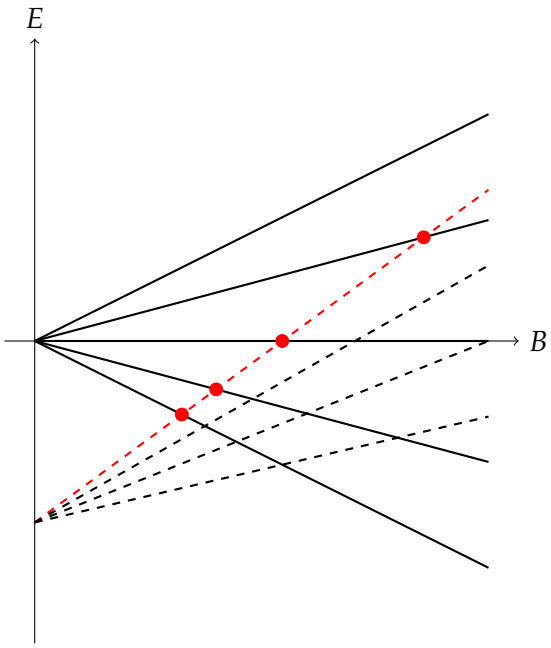

Fig. 4.26: Model Breit-Rabi diagram illustrating the general dependence of energies on the magnetic field. Continuous lines represent bound states, while dashed lines represent resonant states.

If we calculate it for

$$\mu_R = \frac{B_1\mu_1 - B_2\mu_2}{B_1 - B_2} \tag{4.15}$$

$$B_1\mu_1 - B_1\mu_R = B_3(\mu_3 - \mu_R) \tag{4.16}$$

$$B_3 = B_1\frac{\mu_1 - \mu_R}{\mu_3 - \mu_R} \tag{4.17}$$

Indeed, resonances may be observed in bound states of lithium and erbium with increasing angular momentum projections, where the resonant states are a combination of similar eigenvector components. In both ground and excited state calculations, several such channels could be highlighted. Using resonance positions for two channels (ground and first excited), a magnetic moment is calculated using formula 4.15, and the position of an expected resonance in a higher level is predicted with 4.17. Results are shown in tables 4.8 for excited lithium states, and for erbium in 4.9. For those select state resonance positions have been estimated accurately, with an average error of 0.4%. This result confirms the reasoning behind this linear model. It doesn't work effectively for all resonances, though, as results in the converged basis set of $L_{max} = 6$ tend to span many of the coupled channels, and resonant states may be composed of dozens of participating scattering eigenstates.

The model used above also shows another dependence: lower levels, with lower magnetic moment and higher negative inclination, are expected to cross the metastable states (dashed lines) at a smaller angle. It may be expected that with increasing B, lower states would cross resonant states earlier and intersect more of them in a select B range than higher-energy states. It could be said that the gradient of the state's slope would correlate with the amount of resonances in B or, more precisely, resonance density. The derivative of the channel's energy in the magnetic field is the μ calculated above. For the

$B_{m=-5}$	$B_{m=-6}$	$B_{m=-7}$	μ_R	B_{calc}
854	859.3	865.2	5.960e−4	865.4
862.4	870.0	878.3	2.780e−4	879.7
734.4	738.5	743.0	7.030e−4	743.3
201.7	223.0	250.0	−3.060e−4	253.7

Table 4.8: Matching resonance positions in the ground and excited lithium $m_{tot} = -5, -6, -7$ states, calculates the resonant state's magnetic moment, and a predicted resonance position in the $m_{tot} = -7$ state.

$B_{m=-5}$	$B_{m=-4}$	$B_{m=-3}$	μ_R	B_{calc}
111.4	113.0	115.0	3.500e−3	114.7
201.7	208.1	213.2	1.400e−3	214.8
617.8	626.2	630.0	3.700e−3	634.7
897.0	903.7	909.1	7.000e−3	910.2

Table 4.9: Matching resonance positions in the ground and excited erbium $m_{tot} = -5, -4, -3$ states, calculates the resonant state's magnetic moment, and a predicted resonance position in the $m_{tot} = -3$ state.

considered states, staircase function plots of the number of resonances in the magnetic field (analogous to 4.4) have been obtained, and the $N(E)$ function's derivative, dN/dE, was calculated with results presented in table 4.10.

m_{tot}	dN/dE
-3	2.664e−2
-4	4.100e−2
-5	4.490e−2
-6	3.415e−2
-7	2.769e−2

Table 4.10: The derivatives of the resonance densities with respect to the magnetic field calculated for different states.

A correlation between the bound state's magnetic moment μ and resonance density in a given state was calculated using Pearson's correlation coefficient, defined as the covariance between variables divided by the product of their standard deviations[184]:

$$\rho(A, B) = \frac{cov(A, B)}{\sigma_A \sigma_B} \tag{4.18}$$

The resulting correlation coefficients are as follows: -0.9488 for excited erbium and -0.9834 for excited lithium, meaning that for those states, a strong correlation is observed.

4.4 Chapter summary

This chapter focused on the ultracold collisions of lithium and erbium. In the introduction, recent experiments and results with these atoms were overviewed, and key problems were stated. The next section gave details of the theory and methodology: what terms constitute the Hamiltonian, how the interaction potential is constructed, what

functions describe the system, and which computational methods were used. Energy structure, basis set, and potential scaling were discussed, justifying the parameters used for calculations.

The results section was divided into subsections. First, resonance spectra supplemented with tabular results were presented for the ground and a few excited states. It was noticeable that while many resonances are highly decaying, the distribution of the imaginary scattering length is not uniform. The next subsection studied the impact of potential and mass scaling on the resonance profiles, confirming the initial assumptions. It was followed by the results of bound state calculations. Their pattern, with gradients changing and new levels emerging in the excited states, supported the resonance profiles shown earlier. Finally, in the last sections of this chapter, excited lithium and erbium channels were compared qualitatively, showing distinct features pointing to different mechanisms behind quantum resonances. A linear model was fitted to resonance positions, providing evidence that resonances in erbium and lithium states follow different trends. The discrepancies are significant, though not as much as in K+Dy.

The study of the $Li + Er$ system provided insight into how Feshbach resonances work, what causes them, and what their properties are. Lossy features were identified, suggesting possibilities of controlling the system and establishing a framework for future experiments with these species.

CHAPTER 5

Ultracold collisions of potassium and dysprosium

5.1 Introduction to K-Dy

Another promising system worth looking into is potassium-dysprosium. Similar to Li+Er, these molecules consist of an alkali atom and a lanthanide, but the mass imbalance between them is moderate. Potassium, just like lithium, is a spherical atom that has the electronic spin of 1/2 and nuclear spin. Dysprosium is a highly magnetic, dipolar atom with strong anisotropy- a system itself lying conceptually in between spherically-symmetric atoms and molecules[107]. This anisotropy in Dy and spin multiplicities in K are different mechanisms behind couplings causing Feshbach resonances[135].

Unlike the previous system, the rare isotope of fermionic potassium-40 has a very high nuclear spin of $i = 4$, a negative nuclear magnetic moment, and a hyperfine constant [162] and, in turn, an inverse energy level structure. Apart from Li-6, it is the only fermionic alkali; thus, it was designed as the unique building block for model systems with fermions (degenerate Fermi gas, unitary Fermi gas). Dysprosium, on the other hand, has higher electronic orbital angular momenta than erbium, and the highest among all elements. Resulting molecules have almost five times greater reduced mass and a much denser energy level structure, strongly affecting resonance spectra.

As mentioned in the previous chapters, highly magnetic atoms are a testbed for a new generation of quantum simulators in modern physics, with interesting new features - dipole-dipole interactions, which are long-range and anisotropic, were shown to cause additional effects in quantum gases. While theoretical aspects of control and Feshbach resonances were studied before [135, 185], recent years have seen new experiments conducted with dysprosium and potassium. K+Dy ultracold molecules were optically trapped, and some of their resonances have been observed [186, 187]: the Grimm group found many low-field magnetic resonances (up to 6 G) and one broad resonance at 217 G and highlighted a resonance at 7 G as particularly promising for experimental use. The activity in the ultracold dysprosium physics is increasing, and new experimental setups are being launched, e.g., the study of Feshbach resonances in ultracold Li+Dy mixtures by Xie et al was performed just this year [169]. Moreover, the excited Zeeman states of Dy were recently presented by Lecomte, including the decaying Feshbach resonances of ^{162}Dy[188, 189, 190]. This demonstrates the high relevance and the right timing of the present study.

Potassium-dysprosium molecules, with similarities to systems studied previously, but with their own, distinct features, like inverted hyperfine energy levels with spin-stretched state and relatively high reduced mass. and a history of a few successful experiments, may be worth looking into, allowing us to broaden our understanding of highly-magnetic atoms and different types of quantum resonances.

The reason to study this system is similar to that of Li+Er: K+Dy has a much smaller mass imbalance than Li+Er but bigger than other limiting cases of interest to experimentalists, Er+Dy. For the design of experiments, like quantum simulations, multiple options for controlling the interaction strength are important. Thus, for the system like K+Dy it is worth exploring states other than the lowest $m_j(\mathrm{Dy}) = -8 \quad m_f(\mathrm{K}) = -9/2$, e.g., to get the positions of resonances at slightly different magnetic fields. K+Dy also has much better mass-tuning possibilities. While not addressed in this work, the choice of Dy isotope can lead to a different pattern of resonances, as the change in reduced mass is larger than in the Li+Er case.

5.2 Theory and methods

This chapter presents details of methods used for K+Dy calculations. The computational approach from Li+Er calculations was extended to this system, since the systems are sufficiently similar, for reasons described below.

Potential calculated by Zuchowski and González-Martínez using CASSCF and RCCSD(T) methods[164], utilized again. The Li+Er isotropic potential was based on Li+Yb result based on RCCSD(T) potential, while CASSCF was used to reproduce the potential anisotropy attributed to electron angular momentum. Accurately calculating the potential of K+Dy is extremely difficult, since it needs the multireference methods that dissociate properly, while exactly recovering all quantum Λ numbers. However, *averaged* scattering properties, such as density of resonances and mean scattering length, depend weakly on C_6 and reduced mass quite, as the fourth root:

$$\bar{a} \approx 0.48 \sqrt[4]{2\mu C_6/\hbar}. \tag{5.1}$$

The difference between $\bar{a}(\mathrm{LiEr}) = 37a_0$ and $\bar{a}(\mathrm{KDy}) = 63a_0$ is quite significant: in the latter case, C_6 was estimated with the assumption of linear scaling with monomer polarizability, hence $C_6(K + Dy) \approx 2500 a.u.$. However, even a large variation of C_6 of K+Dy keeps it around $60a_0$: the difference between $\bar{a}(\mathrm{KDy})$ obtained with the value $C_6 = 2500$ and used exactly the same as in the case of Li+Er (1508 a.u.) is 55. This relies on the polarizability of Li and K atoms of 164 and 290 a.u. [191], respectively.

Provided the number of bound states of K+Dy is large, it is enough if the error made in the number of bound states is not extensive, one can be certain that the physics of resonances obtained with the model potential is correct. Obviously, to assign the resonances, explain their positions, and predict new ones, or predict the positions of resonances in other isotopic mixtures, one needs as accurate a potential as possible. However, one should mention here that a detailed theoretical model for highly anisotropic atoms seems to be, for the time being, impossible to build. Even the systems with much less complex structure, like Li+Cr, Li+Er, or Li+Ba^+ are very hard to address[192, 193, 194].

The Hamiltonian for K+Dy is similar to 4.1:

$$\hat{H} = -\frac{\hbar^2}{2\mu R^2}\frac{\partial^2}{\partial R^2}R^2 + \frac{\hat{L}^2}{2\mu R^2} + \hat{V} + \hat{H}_K + \hat{H}_{Dy} \tag{5.2}$$

With $\hat{H}_K$ and $\hat{H}_{Dy}$ being separated dysprosium and potassium energy operators:

$$\hat{H}_K = a_{HF}\hat{i}\cdot\hat{s} + (g_e\mu_B\hat{s}_z + g_j\mu_N\hat{i}_z)B_Z \tag{5.3}$$

$$\hat{H}_{Dy} = a_{SO}\hat{l}\cdot\hat{s} + (g_e\mu_B\hat{s}_z + g_L\mu_N\hat{l}_z)B_Z \tag{5.4}$$

Physical constants for calculations of hyperfine and spin-orbit shifts and Zeeman effect were taken from [162, 175]. Potassium's magnetic moment used was -1.298, and the hyperfine constant was -285.731. Reduced mass of 32.09225 was obtained using the NIST atomic database [161]. Interaction potential V_r, as in Li-Er's case, is decomposed into the high-spin and low-spin functions [176] and expressed as a sum of Legendre polynomials:

$$\hat{\mathcal{V}} = \sum_k P_k(\cos\theta)\mathcal{V}_k(R). \tag{5.5}$$

For calculations, the orientation-symmetrical V_0 and anisotropic V_2 potential terms were incorporated. Same programs were employed for K+Dy, namely MOLSCAT, FIELD, and BOUND, also taking advantage of Matthew Frye's resonance matching algorithm[146, 179]. Within this framework, a grid from $r_{min} = 3a_0$ to $r_{max} = 1000a_0$,$r_{mid} = 30a_0$ and $dr = 0.005$. Magnetic field ranged from $0G$ to $1000G$ with a step $dF = 1G$ for calculations in $L_{max} = 4$ and collision energy $E_c = 1e-7K$. For FIELD, the spatial grid spanned from $r_{min} = 2a_0$ with a step $dr = 0.005$ to $r_{max} = 500$ with smaller $r_{match} = 10a_0$. Bound state calculations required varying $r_{match} = 2$ to 8 a_0 and were conducted for states of binding energies -0.1 to 0 cm^{-1} .

The basis set for this system is constructed as follows. Potassium is described by electron and nuclear spins s and i coupled to total spin f:

$$|(s,i)f,m_f\rangle \tag{5.6}$$

With values s = 1/2, i = 4, f = 9/2, $m_F = -9/2$ in the spin-stretched ground state. Note the inverted energy level order, with higher f and negative m_F in the lowest eigenstate. Dysprosium states are denoted by orbital angular momentum l, coupled with electron spin s to j, with projection along magnetic field axis m_j:

$$|(s,l)j,m_j\rangle \tag{5.7}$$

The values for energy minimum are s = 2, l = 6, j = 8, $m_j = -8$. Total momentum projection conserved through the interactions equals -25/2 in the ground state. Excited potassium states have increased total spin projection to $-7/2, -5/2...9/2$ in the lower $f = 9/2$ branch. Elevated dysprosium states are characterised by higher $m_j = -7, -6....$ In the case of K+Dy, $m_{tot} = -25/2$ is the lowest possible value, and all excitations increase it to $m_{tot} = -23/2, -21/2...$ Electron spins of atoms are coupled to $S = 2-1/2, 2+1/2 = 5/2, 2/2$, which are the two spin multiplicities of the interaction potential. Molecular orbital momentum L, disclosed in the Hamiltonian 4.1, also participates in coupling the select states. For calculations, a base value of $L_{max} = 4$ was used.

Energy level structure of the system is depicted in the chart 5.1. In a zero field, the degenerate states' energy depends on total angular momentum F, and the levels are split as the magnetic field increases. The lower branch is split depending on dysprosium spin's projection m_S into five sub-branches, and each is further subdivided into ten levels determined by potassium's angular momentum projection m_F. A crucial aspect of the

structure, clearly visible here, is that excited K levels have just a one-step higher energy, while upper levels of dysprosium reach the next sub-branch, which has a greater impact on the resonance structure. As stated in the introduction, a dense energy level pattern correlates with a high number of resonances, presented in the results.

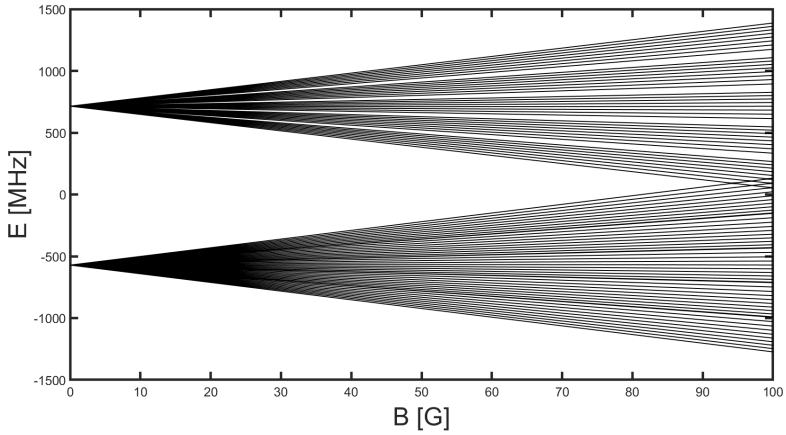

Fig. 5.1: Energy levels in magnetic field for K-Dy molecules.

5.3 Results

This section is dedicated to presenting and discussing the results of calculations in the K+Dy system. The following subsections follow this order: Feshbach resonances in ground and excited states, bound state calculations, chaos in resonance distribution, varying basis size, dipole-dipole interactions, and potential and mass scaling.

5.3.1 Resonances in ground and excited states

First graph 5.2 presents the scattering length in the ground state of K+Dy, associated with $m_{tot} = -25/2, m_f = -9/2, m_j = -8$. The plot reveals analogous behavior to Li+Er at first glance. There's a clearly visible, fine structure of semi-regular, sharp resonances. As the resonant scattering length is real, the numerical values grow indefinitely, but there's a reasonably high level of background scattering length, which is confirmed by exact results in table 5.1. There is little overlap with these narrow resonances. The resonance density is high with 48 resonances in the range 0-1000 G, substantially higher than in Li+Er. Similar to Li+Er, the ground state resonances are real with the scattering length going to $\pm\infty$, although they appear visually limited by the finite grid step.

Excited dysprosium states are considered next. Firstly, the first excited state is described by quantum numbers $m_{tot} = -23/2, m_f = -9/2, m_j = -7$. Real and imaginary parts of scattering length are depicted in fig 5.3, backed by detailed resonance results in tab 5.2. The results show little similarity to the ground state, as the patterns are considerably different. The spectrum is chaotic, with both high and low spikes of narrow

B_C	$a_{\mathrm{BG}}^{\mathrm{RE}}$	Δ
996.22	35.77	2.03
956.6	-730.12	-144.75
924.27	63.19	49.17
862.42	51.55	5.74
848.79	124.04	7.06
826.93	119.21	0.72
775.58	74.04	5.38
728.47	57.66	2.12
697.5	44.91	2.46
680.46	55.57	3.89
635.72	308.22	46.81
634.85	33.69	0.34
561.96	1.04	107.62
550.05	-13.8	-0.72
526.09	291.33	-18.55
521.54	-7.6	-60.07
504.86	-15.4	-4.66
486.8	-91.02	-1.99
455.82	79.61	47.33
413.19	85.04	0.03
401.76	47.89	0.1
384.25	10.2	5.46
356.39	72.38	39.51
313.17	94.82	0.47
296	64.2	1.53
267.36	78.94	13.63
237.88	53.89	0.05
216.16	-284.39	-170.96
201.9	70.53	20.8
197.16	505.49	0.79
181.96	187.75	0.86
159.87	93.83	0.05
149.6	85.35	1.91
126.73	100.17	7.97
122.31	61.81	3.63
114.54	178.66	1.7
93.01	600.36	130.93
87.35	101.83	0.45
82.98	121.16	0.48
79.94	127.36	0
60.03	25.91	3.13
42.46	95.85	0.15
39.32	98.9	0.06
24.68	84.61	0.19
19.79	86.14	0.09
7.12	78.62	0.13
2.88	78.67	0

Table 5.1: Detailed results of resonance fitting for the ground state ($m_{tot} = -25/2$).

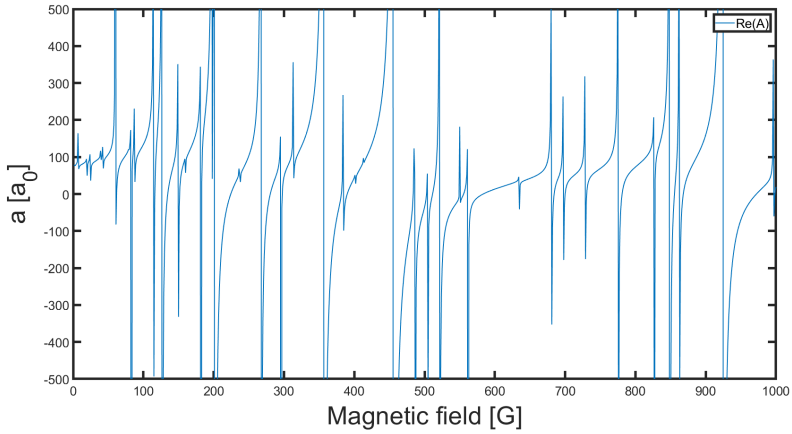

Fig. 5.2: Scattering length as a function of magnetic field. Results for the ground state ($m_{tot} = -25/2$, $m_J = -8$, $m_F = -9/2$).

resonances and strongly overlapping wide ones. There's a region of higher density and some regularity in a low magnetic field, followed by much larger gaps as the field increases. There's a high background real scattering length across the plot, with imaginary resonant parts mirroring real ones (a pattern described before in [3]), indicating strongly decaying resonances.

It's important to note that achieving proper convergence on such broad resonances is challenging for MOLSCAT, for two main reasons. First, the program is numerically optimized for locating sharp features. Second, FIELD returns many apparent resonance positions that do not correspond to resonances, as they appear due to the box states, visible in 5.10, which give no further MOLSCAT results. In regions of broad resonances, many starting field positions either converge on a very distant value or on overlapping resonances undistinguishable from each other.

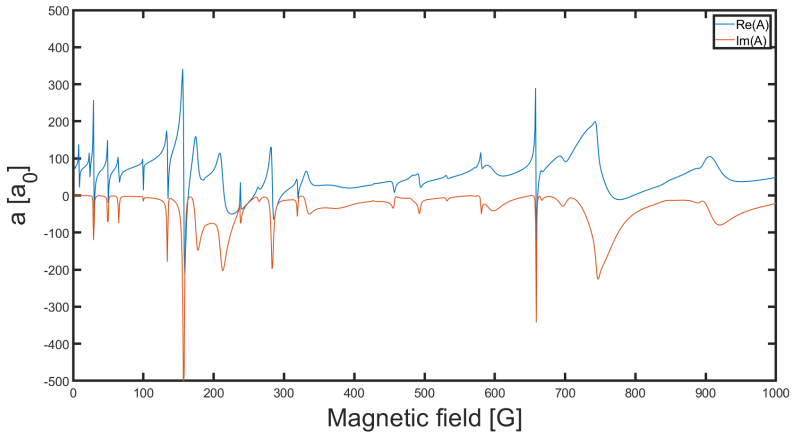

Fig. 5.3: Scattering length as a function of magnetic field. Results for the excited dysprosium state ($m_{tot} = -23/2$, $m_J = -7$, $m_F = -9/2$).

Results in second excited dysprosium state of $m_{tot} = -21/2, m_f = -9/2, m_j = -6$ are exhibited in plot 5.4 and tab. 5.3. The chart presents an even more erratic nature, with scattering length dominated by broad, overlapping resonances of rather weak features,

B_C	$a_{\mathrm{BG}}^{\mathrm{RE}}$	$a_{\mathrm{BG}}^{\mathrm{IM}}$	$a_{\mathrm{RES}}^{\mathrm{RE}}$	$a_{\mathrm{RES}}^{\mathrm{IM}}$	Γ_{inel}	Δ
910.27	41.63	-25.81	37.51	57.84	-32.49	14.64
832.81	92.63	-130.39	-108.13	-66.15	-272.56	-159.09
746.75	38.72	-18.24	206.40	92.30	-19.19	51.13
747.07	34.99	-33.38	200.56	94.40	-20.55	58.90
599.35	70.97	-10.03	30.92	-6.35	-26.53	5.78
580.39	79.47	-12.68	33.25	29.15	-1.81	0.38
573.66	81.81	-6.86	-6.59	-6.31	-3.49	-0.14
531.82	49.10	-6.26	9.05	1.69	-2.68	0.25
492.79	43.03	-12.76	37.95	-5.94	-3.82	1.69
456.69	39.43	-13.09	12.61	-30.70	-3.66	0.59
263.38	14.87	-11.62	0.81	8.16	-2.51	0.07
213.79	37.44	-13.34	195.24	-27.04	-11.62	30.28
237.97	-35.77	-43.25	26.25	74.35	-0.82	-0.30
221.78	134.50	-78.75	59.43	-179.56	-24.58	5.43
175.52	50.11	-53.15	67.02	99.51	-7.15	4.78
157.56	117.65	-10.37	555.83	-120.06	-2.65	6.27
99.85	86.83	-4.53	763.55	46.00	-0.03	0.13
92.95	81.74	-3.22	0.29	-0.98	-0.01	0.00
64.93	68.03	-2.10	73.12	2.33	-1.40	0.75
49.51	69.55	-1.25	172.49	-10.21	-0.81	1.00
40.76	36.32	-5.61	302.60	81.92	-6.44	26.85
29.40	70.02	-0.79	392.09	13.39	-0.56	1.55
23.58	89.11	-0.55	1546.60	-54.65	-0.02	0.19
11.42	123.03	-25.22	109.33	-110.07	-52.82	23.47
8.46	75.04	-0.02	6362.30	11.80	-0.01	0.39

Table 5.2: Detailed results of resonance fitting for the first excited dysprosium state ($m_{tot} = -23/2, m_J = -7$).

with a strong imaginary compound. There's a greater background scattering length, both real and imaginary. Just like in the previous state, there's a different resonance pattern in low and high magnetic fields.

Due to resonance interference visible here, in certain resonances, the imaginary part of the scattering length approaches zero, meaning losses could be suppressed. This behaviour could be adjusted with a magnetic field, opening a pathway for experimental control of resonance decay.

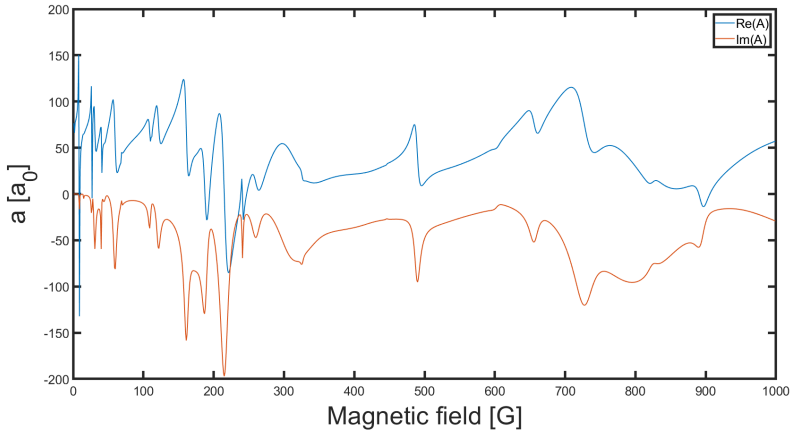

Fig. 5.4: Scattering length as a function of magnetic field. Results for the second excited dysprosium state ($m_{tot} = -21/2, m_J = -6, m_F = -9/2$).

B_C	$a_{\mathrm{BG}}^{\mathrm{RE}}$	$a_{\mathrm{BG}}^{\mathrm{IM}}$	$a_{\mathrm{RES}}^{\mathrm{RE}}$	$a_{\mathrm{RES}}^{\mathrm{IM}}$	Γ_{inel}	Δ
898.44	44.44	-32.31	6.53	-56.18	-33.16	2.44
839.13	64.93	-50.92	22.78	-55.60	-214.51	37.62
720.74	61.98	-62.84	45.25	40.85	-33.10	12.08
661.91	90.65	-40.65	-0.18	-25.09	-16.58	-0.02
649.99	66.83	-24.22	16.30	19.07	-18.26	2.23
621.72	47.96	-65.10	-51.03	25.01	-79.04	-42.05
605.40	-29.96	-77.82	-71.50	89.13	-330.09	393.81
490.14	32.33	-30.53	63.35	19.34	-9.68	9.48
338.40	58.08	36.24	-20.43	-220.04	137.59	24.20
330.55	26.82	-52.25	22.26	-13.92	-19.61	8.14
323.93	19.97	-45.59	28.56	9.13	-15.76	11.28
273.16	37.58	-66.25	-47.05	-17.97	-29.01	-18.16
217.12	28.65	-27.17	165.27	-54.84	-13.11	37.81
191.26	68.52	-82.52	4.83	-97.20	-9.87	0.35
161.78	63.28	-63.63	94.07	14.50	-6.71	4.99
122.03	67.94	-21.39	36.62	13.64	-5.66	1.52
110.64	80.95	-16.37	15.51	-22.37	-3.67	0.35

Table 5.3: Detailed results of resonance fitting for the second excited dysprosium state ($m_{tot} = -21/2, m_J = -6$). All values are given in Gauss.

Now, let's move on to excited potassium states. The scattering length of first two excited states ($m_{tot} = -23/2, m_f = -7/2$ and $m_{tot} = -21/2, m_f = -5/2$ are visualized

in the figure. 5.5. The results are almost identical to the ground state, also included in the plot. The results are numerically different (as proven in the related tab 5.4), but are visually partially indistinguishable. The scattering lengths have also almost completely real values. This corresponds to two factors. First, as reported in the previous section in fig. 5.1, the energy spacing between excited potassium states is much smaller than between dysprosium due to their magnetic momentum discrepancies, hence smaller impact of higher states in K. Secondly, as presented in [195] and highlighted in fig. 2, the energy levels may align in magnetic field in a manner, in which channels may intersect directly vertically to each other. Such an effect would produce resonances in the same positions in excited states.

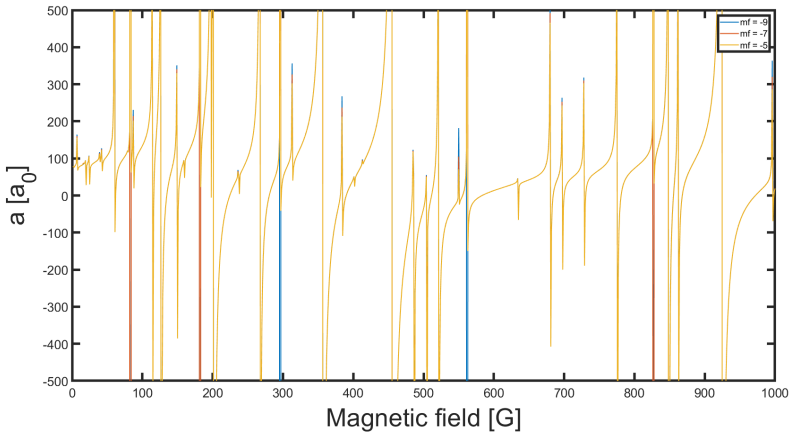

Fig. 5.5: Overlapping plots of the scattering length for different states: ground state, first and second excited potassium ($m_F = -9/2, -7/2, -5/2$).

Let us consider the impact of potassium's promotion to a higher state with simultaneous dysprosium's excitation. Figure 5.6 shows states of first excited Dy and K in ground, first and second elevated levels- $m_{tot} = -21/2, m_f = -7/2, m_j = -7$ and $m_{tot} = -19/2, m_f = -5/2, m_j = -7$. With atoms being excited at the same time, the plot has common features to 5.3, as if potassium's excitation compressed the profile- that is, scaled along the horizontal axis. This effect is non-linear, with weak scaling in lower fields and greater in the higher range. This might be understood with potassium's energy level structure in a magnetic field (reported in [19])- in a lower field, the energy lines are curved due to the Back-Goudsmit effect [162], in the further region, they are linear, with equal spacing between neighbouring states. Same dynamics are manifested in analogous results for second excited dysprosium- that is $m_{tot} = -19/2, m_f = -7/2, m_j = -6$ and $m_{tot} = -17/2, m_f = -5/2, m_j = -6$- brought in the following figure 5.7.

To verify previous results, additional calculations were executed in consecutive higher potassium states in the first hyperfine branch: $m_f = -7/2, -5, 2, -3, 2, -1/2$. Results are showcased in the figure 5.8. The upper panel presents the real parts of the scattering length, which are alike in the depicted states. In the lower panel, the imaginary part of the scattering length is shown. While it's equal to zero in the ground state, it slowly emerges in the $m_f = -7/2$ state and increases in each following one.

B_C	$a_{\mathrm{BG}}^{\mathrm{RE}}$	Δ
996.26	35.79	2.03
924.29	63.19	49.17
862.45	51.37	5.75
848.83	124.33	7.05
826.98	119.28	0.72
821.85	-1262.7	-844.93
775.6	73.72	5.41
730.58	-154.24	-51.66
728.48	57.67	2.12
697.52	44.9	2.46
680.49	55.46	3.89
642.28	276.02	40.42
634.87	33.7	0.34
562	3.39	25.02
550.08	-13.78	-0.72
521.53	-16.81	-19.01
504.88	-24.55	-2.95
486.81	-91.19	-1.99
455.55	1038.7	1.06
413.22	85.03	0.03
401.78	47.76	0.1
384.26	-7.31	-8.68
362.21	48.68	27.73
356.41	118.5	23.26
313.19	94.33	0.47
296.03	63.58	1.53
267.37	78.95	13.58
237.92	54	0.05
201.93	70.45	20.75
197.18	504.55	0.8
181.99	188.39	0.86
176.69	11.58	85.37
159.89	93.81	0.05
156.47	-82.45	-283.96
149.62	84.76	1.91
126.76	102.52	7.82
117.18	500.8	106.85
114.55	178.01	1.7
101.13	1070	178.89
87.4	101.86	0.45
83	118.91	0.49
79.95	127.26	0
60.09	64.64	1.91
48.87	104.39	0
42.49	95.82	0.15
39.37	98.92	0.06
24.7	84.59	0.19
19.81	92.37	0.08
7.12	78.63	0.13
2.89	78.75	0

Table 5.4: Detailed results of resonance fitting for the first excited potassium state ($m_{tot} = -23/2, m_F = -7/2$).

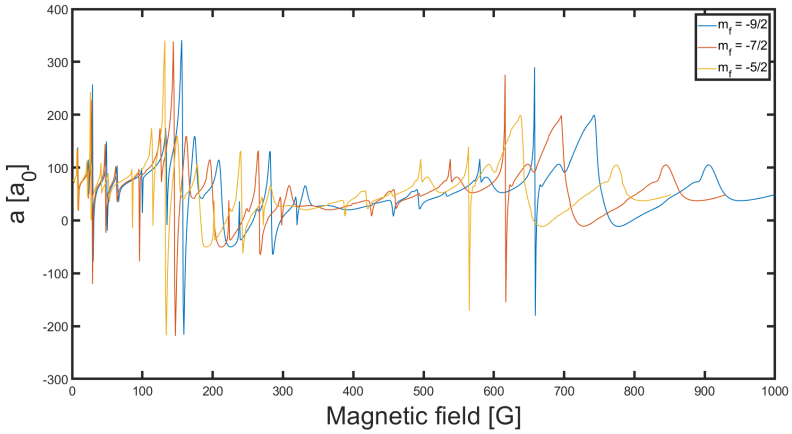

Fig. 5.6: Overlapping plots of the scattering length for different states: Dy in the first excited state, K in the lowest, first, and second excited states ($m_J = -7, m_F = -9/2, -7/2, -5/2$).

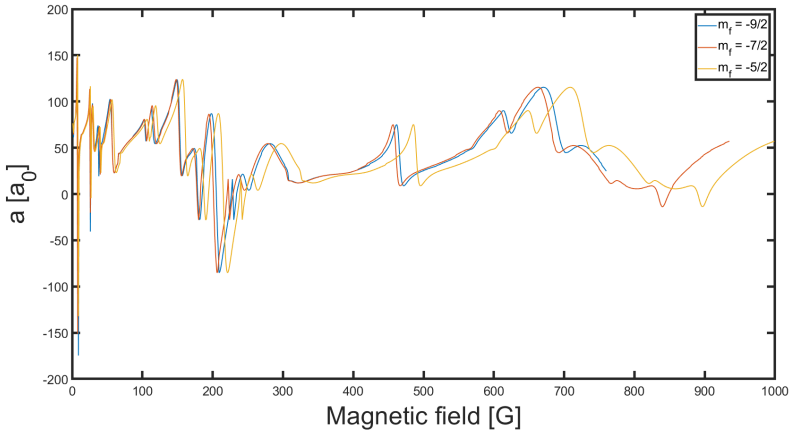

Fig. 5.7: Overlapping plots of the scattering length for different states: Dy in the second excited state, K in the lowest, first, and second excited states ($m_J = -6, m_F = -9/2, -7/2, -5/2$).

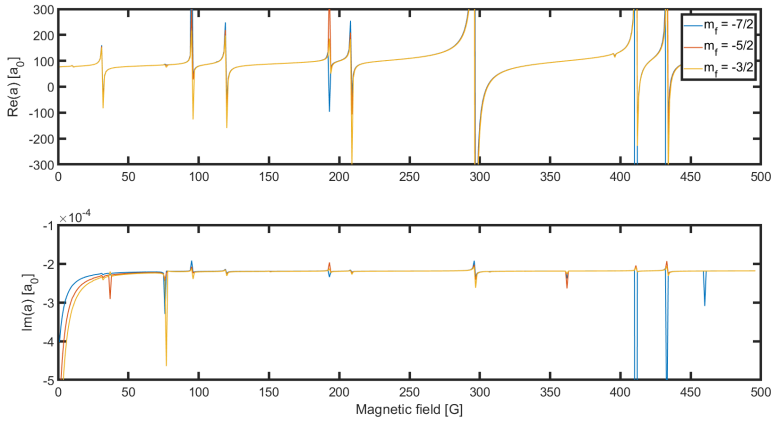

Fig. 5.8: Panel plot showing real (top) and imaginary (bottom) parts of the scattering length of excited potassium states ($m_F = -7/2, -5/2, -3/2$).

5.3.2 Bound state calculations

This section is devoted to the study of bound states in ultracold K-Dy molecules. Calculations were performed in ground and excited dysprosium states ($m_j = -8$ and $m_j = -7$) in a magnetic field ranging from 0 to 200 G for states below the dissociation threshold (energy between $-0.1K$ and $0K$). Diagram 5.9 shows the resulting bound level structure. The spectrum is rather irregular, with varying gaps between states and more crowded bands. All states increase their energy in a magnetic field, but inclination varies from low to almost horizontal. The bound state density and number of crossings are much greater than in the Li-Er system, even in the lower field range, which corresponds to a greater overall number of resonances detected.

Results for the excited state are displayed in the fig 5.10. It clearly bears resemblance to the ground state. Most bound states present previously have a lower slope, with some states even decreasing their energies, which moves crossings rightwards. They are accompanied by plenty of new bound states, further increasing the bound state density. A band of potential well's "bound" states is visible here as well. There are a few noticeable avoided crossings.

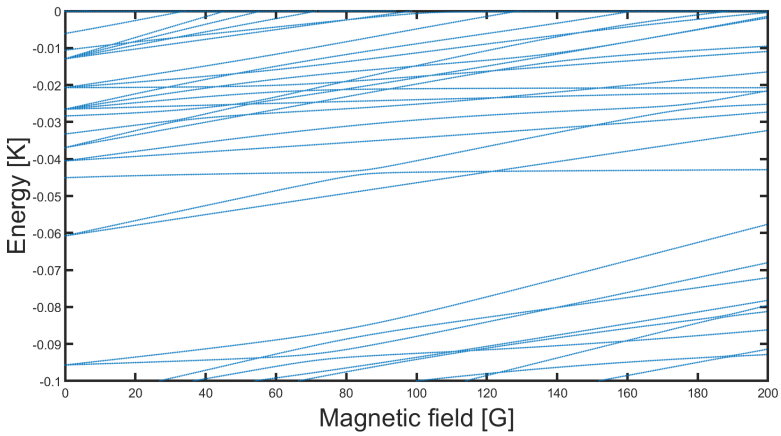

Fig. 5.9: Bound state energies as a function of magnetic field in the ground state ($m_{tot} = -25/2$).

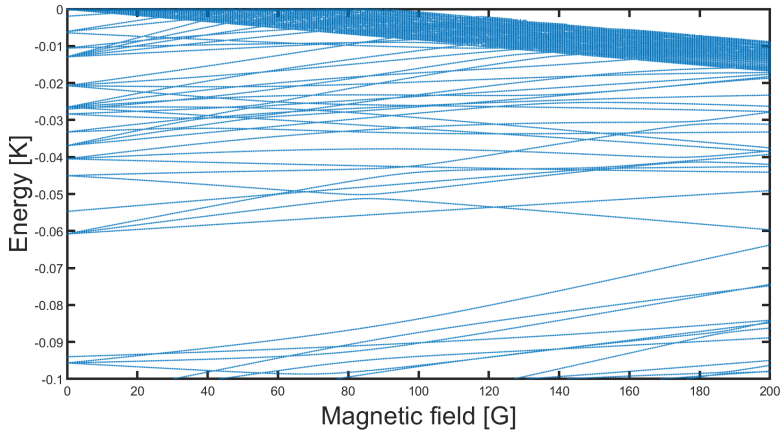

Fig. 5.10: Bound state energies as a function of magnetic field in the excited dysprosium state ($m_{tot} = -25/2, m_J = -7$).

5.3.3 Chaos in ground state resonances

First, resonance positions are "unfolded" by a cumulative spectral function; the staircase function of $\Theta(x)$ Heaviside step function, expressed in the formula 5.8. A smooth polynomial function is then fitted to it (as it is already almost linear in the magnetic field). A nearest-neighbour spacing function is constructed, with values depending on unfolded positions as $s_i = \xi_{i+1} - \xi_i$.

$$S(X) = \sum \Theta(X - X_i) \tag{5.8}$$

The Brody parameter η is fitted to the NNS distribution. It interpolates between limiting cases $\eta = 0, 1$. η has an interpretation that a function of $\eta = 0$ follows strictly Poisson statistics, and $\eta = 1$ is purely chaotic. A histogram with a fitted distribution is a good visualisation of this feature. The Brody distribution follows the formula 5.9:

$$P_B^{\eta}(s) = c_\eta(\eta + 1)s^{\eta} exp(-c_\eta s^{\eta+1}) \tag{5.9}$$

Light atoms, with rapidly varying wavefunctions, are more sensitive to the interaction potential, but have fewer channels and tend to have a more regular resonance distribution. Heavy atoms with high magnetic moments, on the other hand, have more degrees of freedom and anisotropic structures, which couple more channels, increasing the number of resonances and introducing quantum chaos. Diatomic molecules of light and heavy atoms could be expected to be in between those extremes [164]. For KDy molecules, an NNS distribution analysis was performed for ground-state resonances following the methods used in [109]. Brody parameter was derived, with a fit of $\eta = 0.66$, meaning the resonances are moderately chaotic, which is an expected outcome- dysprosium causes much of the resonance spectral irregularity in this system. Results are illustrated on plot 5.11.

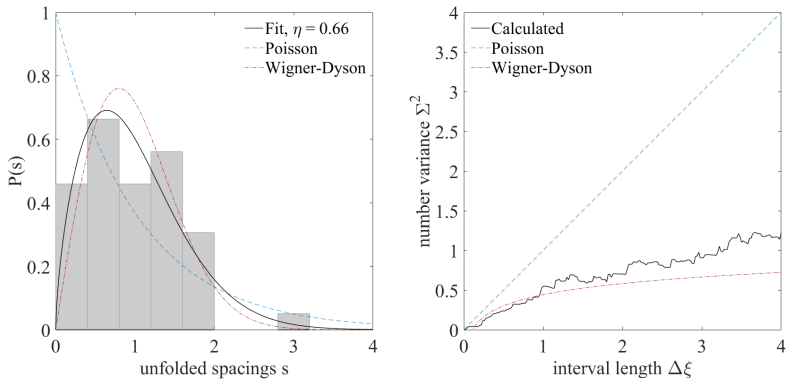

Fig. 5.11: Left panel: histogram of the NNS distribution for K-Dy resonances, with a Poisson, Wigner-Dyson, and fitted Brody distributions. Right panel: level number variance with Poisson and Wigner-Dyson predictions as a function of interval length.

5.3.4 Further considerations

This section addresses the results of varying basis size, potential scaling, and dipole-dipole interactions. We begin by examining the comparison between the scattering length calculated with and without taking the dipole-dipole interaction into account. As seen in 5.12, the plots are very similar. The curves are offset by a few G, and the line, including dipole-dipole interactions, shows a few additional peaks in the scattering length; their number is much lower than in a similar situation discussed in [185], where the amount of additional resonances is substantial.

Results of real and imaginary scattering length, both with and without dipole-dipole effect, in the first excited dysprosium state $m_j = -7$ are presented in 5.13. While the general patterns are similar here, there's a greater variance in scattering length's amplitude, which is noticeable in the imaginary part, even stronger than in the real one. The effect of incorporating dipole-dipole interactions is not as impactful as it is in other systems.

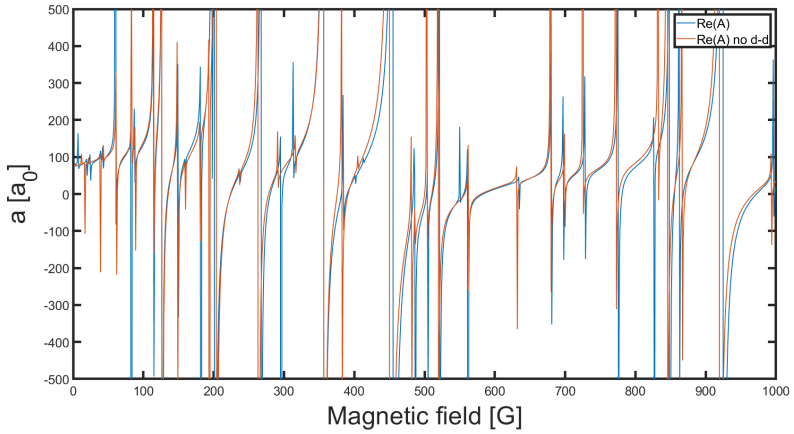

Fig. 5.12: Scattering length as a function of magnetic field. Overlapping results for the ground state with and without dipole-dipole interactions.

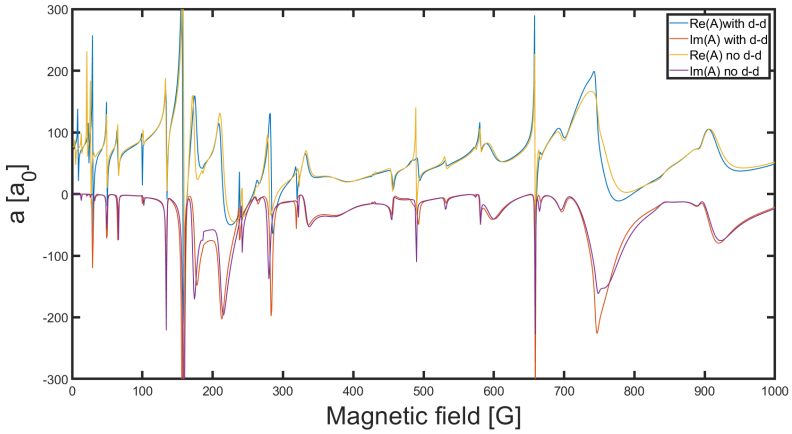

Fig. 5.13: Scattering length as a function of magnetic field. Overlapping results for the first excited dysprosium state with and without dipole-dipole interactions.

Next, we turn to measuring the effect of increasing the basis size. As computations in the K-Dy system are more costly than in Li-Er, full basis convergence wasn't conducted. Let's try to estimate this impact by comparing the results of calculations with various basis sets. Presented in fig 5.14 are results in the ground state with $L_{max} = 8, 12, 16$, with $L_{max} = 8$ being the benchmark for other calculations. Increasing the basis set to $L_{max} = 12$ increases the number of resonances considerably, though it requires much greater resources to perform. $L_{max} = 16$ does not seem to provide further advantage, despite even greater computational time. Similar results were obtained in the excited state, as documented in 5.15.

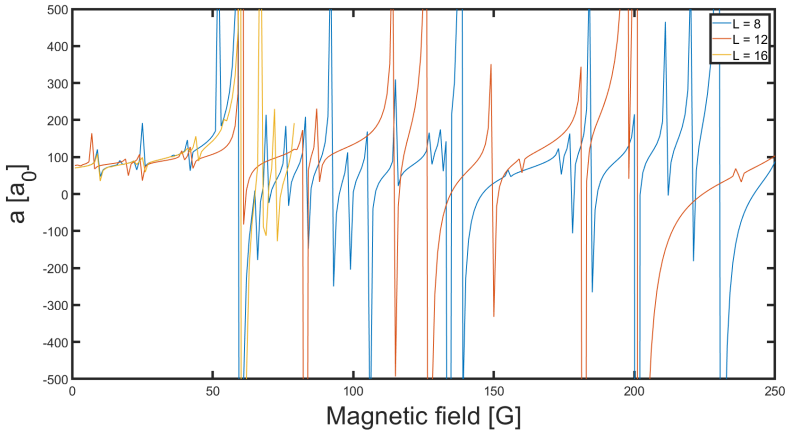

Fig. 5.14: Scattering length as a function of magnetic field. Results for the ground state for different basis sizes ($L_{max} = 8, 12, 16$).

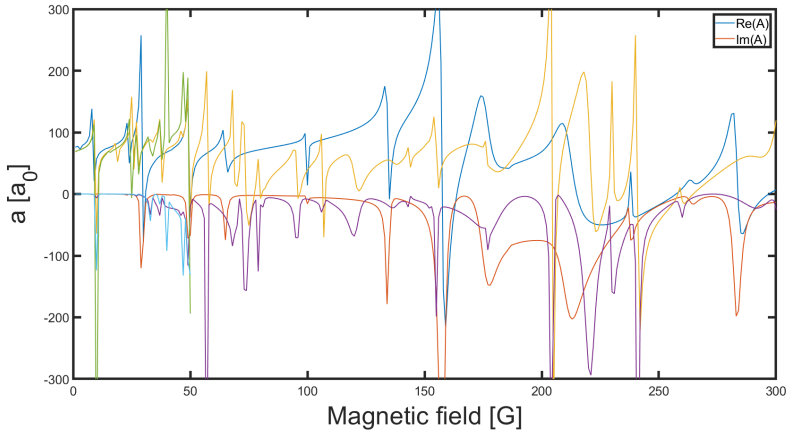

Fig. 5.15: Scattering length as a function of magnetic field. Results for excited dysprosium state for different basis sizes ($L_{max} = 8, 12, 16$).

Let us now examine results in a smaller basis set. The minimal size, which would include all necessary couplings, would be $L_{max} = 2$. Decreasing the resonance density could be a useful way of reducing the number of variables to pinpoint and separate the contribution of particular effects. The scattering length chart 5.16 shows very few peaks with no distinguishable pattern. Do note that results for the excited potassium match those for the ground state in this case.

Figure 5.17 shows results for ground and excited K states, both with and without dipole-dipole interaction. The results are mostly mimicked here, with a slight detuning and a single additional resonance in the former plot.

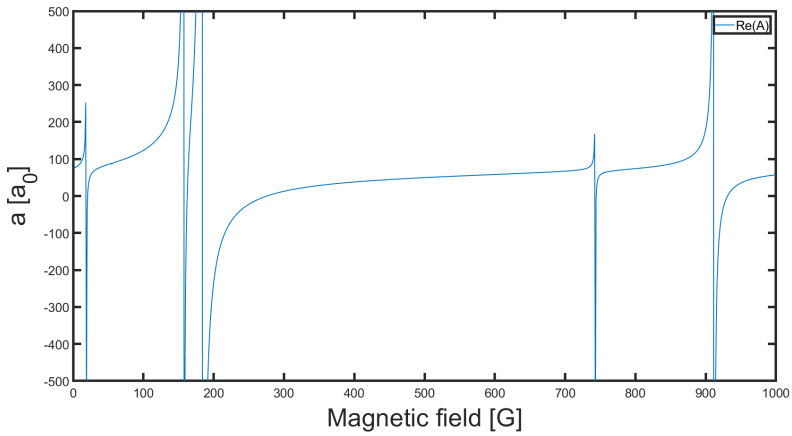

Fig. 5.16: Scattering length as a function of magnetic field for the ground and first excited K states in a smaller basis set ($L_{max} = 2$) including dipole-dipole interaction

Finally, we address the significance of scaling the interaction potential in the K-Dy system. Scattering length as a function of potential scaling follows a pattern recognized previously in 4.5. The full cycle of scattering length is expected to fit within 6% of the scaling factor due to the value of the reduced mass. Figure 5.18 illustrates the results of scaling by $+-1\%$. Such perturbation changes both the density and distribution of resonances.

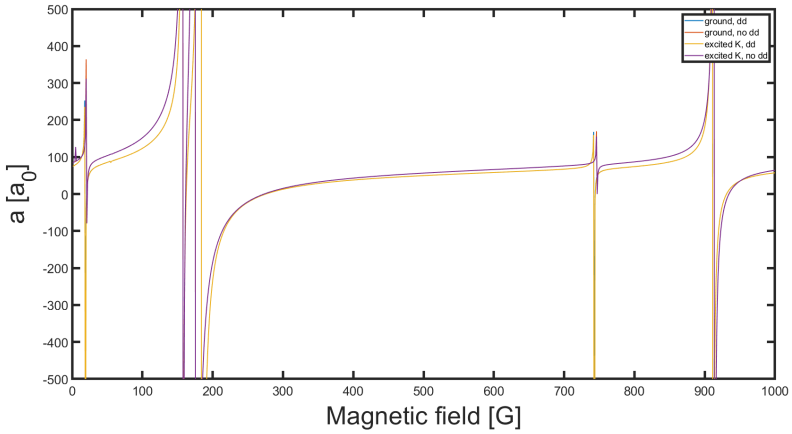

Fig. 5.17: Scattering length as a function of magnetic field for the ground and first excited K states in a smaller basis set ($L_{max} = 2$). Comparison of results with and without including the dipole-dipole interactions.

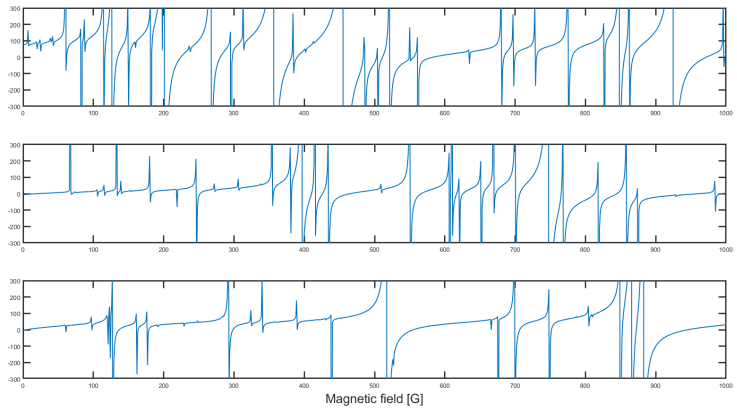

Fig. 5.18: Panel plot of the scattering length as a function of magnetic field for the ground state for various V_0 potential scaling factors λ. top panel: $\lambda = 0.99$, middle panel: $\lambda = 1$, bottom panel: $\lambda = 1.01$.

5.4 Chapter summary and future studies

In this chapter's introduction, a general picture of the potassium-dysprosium system was presented, and a survey of relevant publications and recent scientific progress was given. The system's features, with similarities and differences to the Li+Er molecules, as well as motivation for the research, were provided. The next section is dedicated to the methods and explains why and how the approach applied in the previous chapter could be extended to K+Dy, and what the key differences are. Computational details were disclosed.

The results section included resonance details, with both charts and tabular data. The resonance spectra were denser and less regular than in the case of Li+Er. While excited dysprosium states had radically altered resonance profiles, in the states of excited potassium, the changes were hardly distinguishable. Resonances corresponding to excited dysprosium states are highly decaying, as opposed to those involving excited potassium. Transferring potassium to higher states with simultaneous dysprosium excitation proved to have a nonlinear impact on the scattering length profiles. Bound state results provided a much denser structure, while the general behaviour remained consistent with previous observation, which aligns with the scattering length results. A statistical analysis of the scattering resonance distribution was performed, showing that the resonances in K+Dy are partially chaotic. The last section spanned the results of changing the basis size, verifying the impact of potential scaling and influence of dipole-dipole interactions, which appeared to be smaller than initially expected.

Potassium-dysprosium molecules are another example of a strongly asymmetric system with a highly magnetic atom, like Li+Er. Its resonance spectra are, however, more congested and chaotic, while some aspects, like incremental changes in the resonance spectrum in excited potassium results (compared to the ground-state spectrum), are not straightforward. This non-intuitive behaviour could be partially explained by a much smaller energy difference between the excited potassium and dysprosium states. While this system was not investigated as thoroughly as the previous one due to several limitations, many results highlight the core properties of K+Dy molecules, and gaps in our understanding provide justification for further research.

There is one potentially interesting application common to both the Li+Er and K+Dy cases. In quantum simulations, it is crucial to have well-controlled interactions between partners in optical arrays. Two-body losses have usually been considered an undesired feature, potentially killing the applications. In particular, Hubbard models (for fermions, bosons, or mixed ones) can be simulated with optical lattices (of tunable depth) and Feshbach resonances. As is evident from our study, it is possible to control the two-body loss with the magnetic field, tuning it from (almost) zero—where losses can be completely suppressed via *Fano* interference—to very large values. As an example application, consider a system described by a Hubbard Hamiltonian but with dissipation acting on a single particle, such as a fermionic Dy in the two lowest Zeeman states mixed with potassium. Tuning two-body loss near selected Feshbach resonances allows the realization of Hubbard-like models with an effective non-Hermitian contribution that encodes *controlled* dissipation.

In the ultracold realm, similar experiments were already studied; a prominent example is the combined work of the groups of Jun Ye and Ana Maria Rey. In their work, KRb chemical reactions were suppressed via lattice confinement and the continuous *quantum Zeno* effect. A similar scenario could be realized in K+Dy, with improved control over the two-body loss rate via the magnetic field and with much smaller kinetic-energy release. At a low magnetic field, the relaxation of Dy from an excited Zeeman state does not release more energy than a typical optical-trap depth. For instance, the kinetic energy release of the Zeeman state of Dy by $\Delta m_j = 1$ corresponds to an energy of 40 μK, equivalent to the field of 1 G. New types of quantum Zeno experiments can become possible with the systems which we studied in the present thesis.

CHAPTER 6

Ultracold Collisions of Strontium and Strontium Monohydroxide

6.1 Introduction to Sr+SrOH

Ultracold polyatomic molecules have recently emerged as powerful platforms for probing physics beyond the current state of knowledge [196]. Their rich internal structure, featuring opposite-parity states separated by a small energy gap, large permanent dipole moments, and rotational and vibrational degrees of freedom, makes them ideal candidates for the exploration of new physics [197, 198]. Long-lived bending vibrational levels can be fully polarized with fields and photon cycled, amplifying the sensitivity of searches for the electron electric dipole moment [199, 200]. Extended coherence times of trapped molecules allow precision spectroscopy of multi-mode vibrational transitions, which are particularly sensitive to variations in the proton-to-electron mass ratio [201]. Symmetric top molecules extend these advantages to probe T-violating interactions[202, 203, 121].

It is appealing to broaden such investigations to asymmetric top molecules. With three distinct principal moments of inertia, these molecules lack the simplifying symmetries present in linear or symmetric top models and thus exhibit more complex rotational and vibrational structures. This complexity gives rise to new features, such as independently controllable permanent dipole components, increasing their usefulness in precision measurement and quantum science applications [198]. At the same time, with strong dipolar interactions and complex internal structure, polyatomic species are compelling for quantum simulation [204, 205] and quantum information [206, 207, 208].

Theoretical progress has greatly expanded the range of polyatomic molecules considered for laser cooling, introducing entirely new classes of candidates with properties suitable for their precision control [209, 210, 211]. Radium monohydroxide has been recently noticed as the heaviest polyatomic molecule possible to directly laser cool, offering both efficiency and sensitivity to violations of fundamental symmetries in physics [212, 213]. The *ab initio* calculations have pointed to tetratomic species CaCCH and SrCCH as promising candidates, showing highly diagonal Franck–Condon factors (FCFs), short radiative lifetimes, and Doppler limits in the μK regime [214]. Current predictions extend even further to aromatic-ligand complexes containing alkaline-earth optical cycling centers, including benzene, phenol, cyclopentadienyl, naphthalene, coronene, and other frameworks incorporating alkynyl chains [215, 216, 217, 218]. Recent theoretical studies of lanthanide monohydroxides highlighted them for symmetry violation experiments, due to their electronic states, static dipole moments, and zero-field splittings[122].

The field of polyatomic ultracold molecules is still largely unexplored, with the exception of Li-SrOH collisions in a magnetic field [219]. To take advantage of the facts mentioned above, the production of ultracold asymmetric top molecules from Sr atoms interacting with a polyatomic radical, SrOH, was investigated. The study emphasised

their electronic structure, intermolecular interactions, cold collisions, and the possibility of forming molecules using the simplified concept of stimulated Raman adiabatic passage (STIRAP). To complement the state-of-the-art *ab initio* methods used to determine the static polarizability of SrOH, analyze its interactions with a family of s^2-type atoms (Mg, Ca, Sr, Yb, Hg), obtaining a detailed potential energy surface (PES) of the Sr–SrOH complex in its $X^2\Sigma^+$ electronic ground state and establishing a way of obtaining Sr_2OH molecules, calculations of resonance structures in cold collisions and bound state spectra were performed [220]. Numerical analysis proved that Sr–SrOH remains non-reactive under ultracold conditions and displays a high potential energy anisotropy. This produces a fine set of near-threshold bound states and an exceptionally rich array of scattering resonances.

6.2 Computational details

The collisional Hamiltonian accounts for the center-of-mass motion, the interaction potential between the collision partners, and the rotational structure of the linear rigid molecule. The reduced mass, $\mu = 47.83$ u, corresponding to ^{88}Sr + ^{88}Sr^{16}O^{1}H, was derived from the NIST atomic data [161]. The rotational constant of SrOH was set at $B = 0.249203$ cm^{-1}, based on the experimental results [221]. The collision energy E_{col} was fixed at 1 μK, limiting collisions to $s-$wave regime, where only the $L = 0$ partial wave contributes.

The following quantum scattering calculations were performed using MOLSCAT and BOUND [146, 86]. The scattering length a was extracted from the single-channel probability amplitude and phase by solving the close-coupling equations [77] using the hybrid log-derivative Airy propagator [78, 79]. Grid parameters for numerical propagation were optimized by tracking the number of resonances in the scattering length spectrum with varying interaction potential scaling by $\lambda = 1 \pm 0.05$. Final parameters were set to $R_{\text{min}} = 2.5$ Å, R_{mid} and $R_{\text{match}} = 10.0$ Å, $R_{\text{max}} = 300.0$ Å, and rotational states up to $j_{\text{max}} = 50$. This close-coupling methodology was then applied to the bound-state problem, using parameters identical to those used in the scattering length calculations.

Then, bound state positions were "unfolded" by the staircase function detailed in 5.8. A quadratic polynomial function was fitted to it, and the numerical derivative of the bound state with regard to binding energy was obtained. A NNS function was defined and the Brody parameter η fitted to the distribution. The method used is analogous to that employed in [109]. This is a similar procedure to the one used in the previous chapter, accommodated to limitations of field-free calculations, following the idea that "large variation on the shifts between adjacent resonances can be attributed to the repulsion between molecular bound states that is central to quantum chaos"[110].

6.3 Results

Figure 6.1 shows results for a narrow interval λ between 0.98 and 1.02, within which both spectra are very dense. The thick red line shows the real part of the s-wave scattering length calculated using only the isotropic component (Legendre term $V_{\lambda=0}$) of the interaction potential. Precise anisotropy control allows evaluation of its impact on the Feshbach resonance spectrum. As is known from Gribakin and Flambaum's formula [103] scattering length exhibits a pole whenever the bound state is exactly at threshold, thus a single broad resonance just above $\lambda = 1.00$.

However, when the full anisotropic potential is considered, the scattering length turns into a dense spectrum of narrow resonances associated with the rotational structure of the SrOH molecule, seen as blue lines in the plot. Each of these arises when a bound state is brought to the threshold by varying λ. Generally, narrow resonances are produced by bound states with weaker coupling to the ground rotational state, in particular, to states dominated by higher rotational states j and high end-over-end quantum number L, since, in the ground state, $\mathbf{j} + \mathbf{L} = 0$.

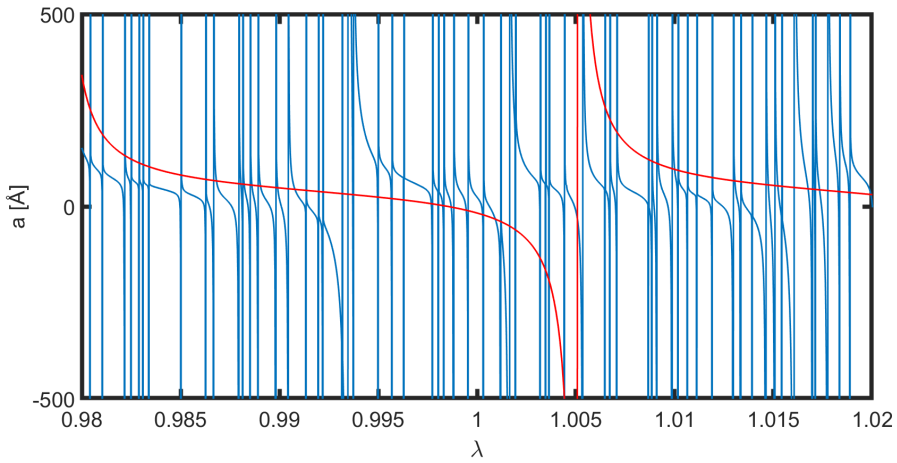

Fig. 6.1: Scattering length as a function of λ in the ground state. The red curve corresponds to only the isotropic part of the interaction potential, while the blue lines include all Legendre expansion terms.

Chart 6.2 confirms this observation: the near-threshold bound states show numerous avoided crossings, which are evidence of their coupling and actually cross zero energy at precisely the λ values corresponding to resonances in fig 6.1. During the full $\pm 5\%$ scan in λ, 159 distinct resonant features were identified, which corresponds to ~ 16 resonances per 1% change in the potential. Such a high density of resonances underlines the extreme sensitivity of ultracold Sr-SrOH collisions to details of the short-range potential, and illustrates the importance of including full anisotropic couplings when predicting or interpreting scattering properties in this system. A staircase plot of the bound state positions is presented in 6.3. A polynomial function fitted to the results and its derivative, the dependence of bound state density on binding energy, is shown in 6.4. Note that this illustrates states bound within $100 cm^{-1}$, as there are a total of 2209 bound states, including those lying deeper.

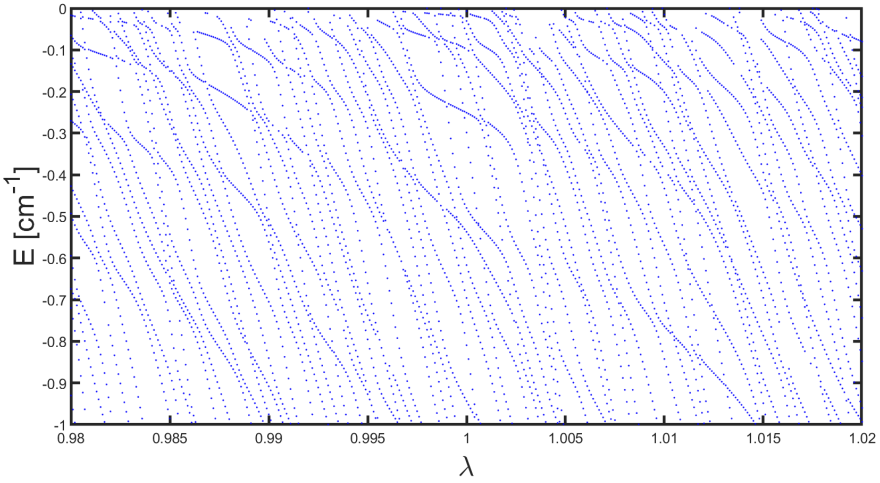

Fig. 6.2: Near threshold bound states as a function of λ in the ground state of Sr-SrOH.

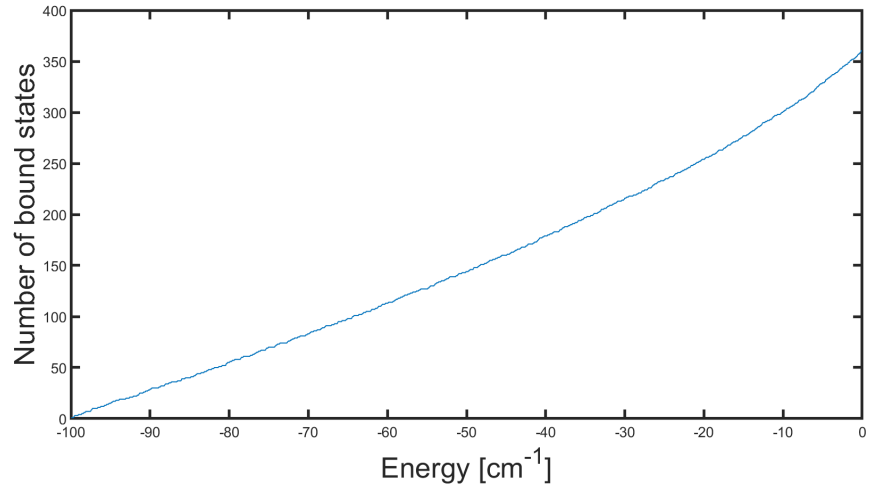

Fig. 6.3: Staircase function plot of $Sr - SrOH$ bound states.

Figure 6.1 clearly demonstrates that the source of resonances in the Sr-SrOH system is the anisotropy of the potential energy surface. The observed resonance spectrum as a function of potential scaling is significantly more congested than in the study of ErYb [110]. The spectrum of near-threshold bound states highlights the potential to form the Sr–SrOH complex by mergoassociation [68, 58]. By merging two optical tweezers [56, 67, 66], one containing a strontium atom and the other containing an SrOH molecule, slowly enough to follow the trap-induced avoided crossing between their separated motional state and a weakly bound Sr–SrOH level, one can adiabatically convert the pair into a molecule. Because Sr–SrOH exhibits a very dense spectrum of bound states, there will be multiple closely spaced avoided crossings; adiabatic passage across the most strongly coupled crossing may convert the atom–fragment pair into a bound Sr–SrOH molecule. As the ground- and excited-state potentials parallel each other, the STIRAP method could be favourable for the association of Sr_2OH molecules in the ground state [220].

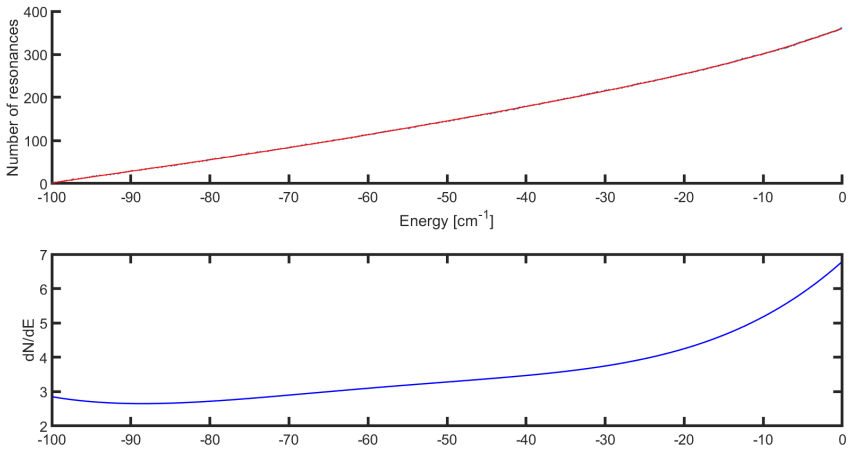

Fig. 6.4: Top panel: Polynomial fit of the staircase function of bound states. Bottom panel: derivative of the polynomial with respect to energy, dN/dE.

In systems containing highly magnetic lanthanide atoms [107, 222, 133, 223, 110], the interplay between strong interaction potential anisotropy and Zeeman coupling under an external magnetic field gives rise to a chaotic resonance distribution, as evidenced by level spacings following the Wigner-Dyson distribution [133]. Similarly, the Sr–SrOH system may exhibit a chaotic resonance structure, since its rotational degree of freedom effectively serves as orbital angular momentum in highly magnetic systems. This was displayed by chaotic signatures in the statistical analysis of Li-CaH and Li-CaF bound states near threshold [109]. In the ultracold regime, the structure of resonances and spacings between them is a result of repulsion between molecular bound states, which is associated with quantum chaos in the molecular system [110]. To quantify this behavior, the bound state distribution was analyzed by fitting the Brody parameter to the bound state profile, which yielded a value of $\eta = 0.84$, confirming the chaotic nature of the system, as shown in panels 6.5.

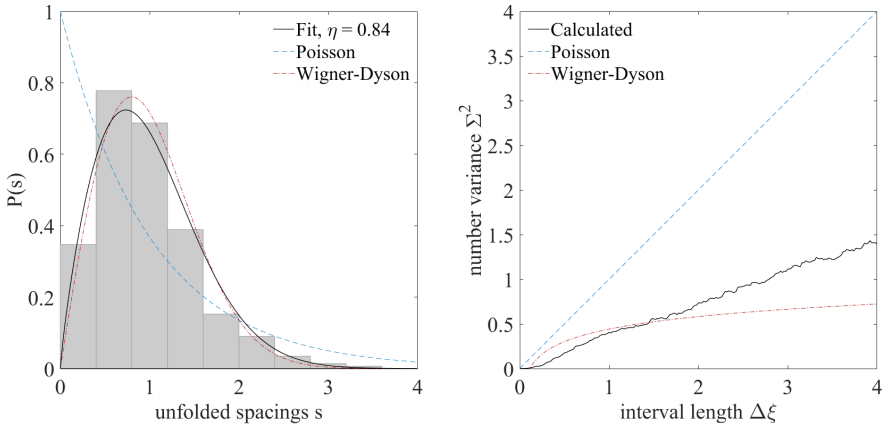

Fig. 6.5: Left panel: histogram of the NNS distribution for Sr-SrOH bound states, with a Poisson, Wigner-Dyson, and fitted Brody distributions. Right panel: level number variance with Poisson and Wigner-Dyson predictions as a function of interval length.

Figures 6.6 and 6.7 present results of preliminary calculations in rotationally excited states- J = 1 and 10, respectively. For the $J = 1$ state, the real part of the scattering length exhibits sharp, pronounced features, while the imaginary part shows high resonant values and essentially zero background scattering length- meaning that the decay would happen only on resonances. In contrast, the results for the $J = 10$ state depict lower resonant peaks and smaller variance in the scattering length, with both real and imaginary parts displaying considerable background values. This indicates resonances influence the loss characteristics less strongly than in the lower state.

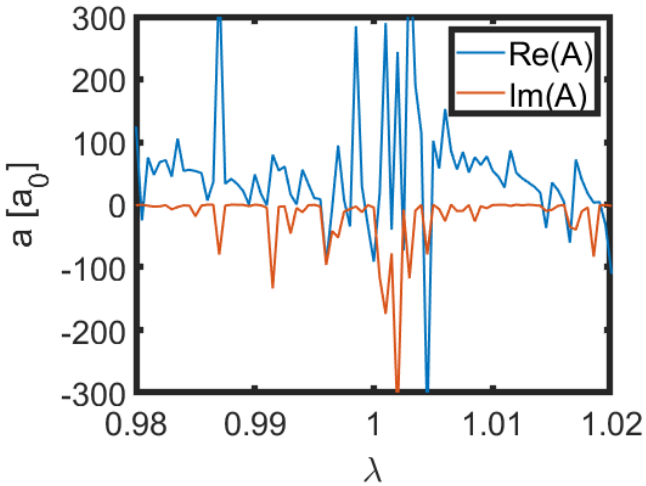

Fig. 6.6: Scattering length as a function of λ in the rotationally excited J=1 state.

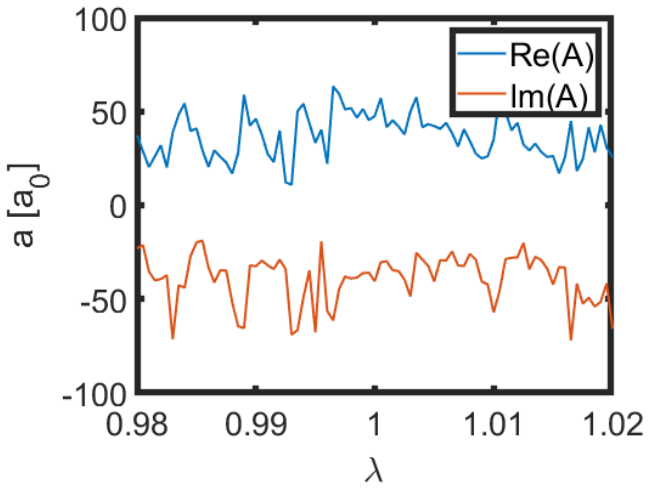

Fig. 6.7: Scattering length as a function of λ in the rotationally excited J=10 state.

6.4 Discussion on possible mechanisms behind Feshbach resonances

These preliminary observations motivate further investigations into the detailed nature of its resonance spectrum, as the chaotic nature of resonances means that the collision partners might stay 'glued' together in the bound state for a longer time [109, 106, 224] and experience so-called *sticky collisions*, which are likely producing losses due to atom-complex collisions, not to be confused with three-body events.

It is also worth discussing the association of Sr and SrOH perspectives, given the high density of states of this system. Full quantum scattering calculations are immensely complex and are out of the scope of this work. Hence, let us discuss the coupling mechanisms that might induce Feshbach resonances to explore the possibility of linking the atoms and molecules into bound states. Certainly, the rotational states of SrOH molecules are strongly coupled, and the bound states of the systems are in a Wigner-Dyson chaotic regime in which one can consider them to be a strong mixture of rotational quantum numbers and many end-over-end angular momentum states. However, for e.g., the magnetic field, it is more relevant if the Zeeman states of SrOH are coupled, given Sr has no spin. Let us consider several mechanisms:

- **Spin-rotation effect** for which the Hamiltonian reads $H_{\mathrm{SN}} = \gamma N \cdot S$, coupled to a strong potential anisotropy, can introduce Feshbach resonances in the scattering, similarly as in the case of Na-NaLi tested experimentally by the group of Ketterle [225, 226]. In the present case, the molecule is a doublet sigma, which produces fewer resonances than in NaLi, but at the same time, the rotational states in the system Sr-SrOH are coupled much more strongly.

- **R-dependent hyperfine terms**: as in the case of the Rb-Sr system [195, 227], one might strongly suspect that spin density on SrOH strongly transfers onto the Sr atom and depletes from the molecule, where it is mostly located on the Sr^+ ion.

The hyperfine coupling of SrOH is present only due to the Fermi contact interaction of energy density with the proton, unless strontium is fermionic. Hence, the mechanism of modification of SrOH hyperfine is expected to be very weak. In case a free Sr atom is a fermion with nuclear spin, one expects the same mechanism that drives low-field magnetic Feshbach resonances in the Rb-Sr case (mechanism II identified in [195]). These resonances were found to be very narrow, but in contrast to the Rb-Sr system, where bound states correspond to clean L quantum numbers, in the Sr-SrOH system, there are numerous and strongly coupled s-wave bound states, and there are more opportunities to produce Feshbach resonances. Similarly, the ^{87}SrOH molecule has hyperfine coupling on the Sr atom, which is geometry-dependent within the complex; thus, the Feshbach resonances of similar character as mechanism number I of [195] should be observed. Other hyperfine effects might also include changes of the electric field gradient on the nucleus of ^{87}Sr, which has a very large quadrupole moment. Given the high polarization of Sr by a polar molecule, very large changes of the electric field are possible. Electric quadrupole moment couples rotational states of the whole complex with nuclear spin projection quantum numbers, which *should* produce another mechanism for Feshbach resonances

- **Electric and microwave field**: Since the molecule is polar, and has a large dipole moment (about 2 D), it can be easily manipulated with static, electric or microwave, fields [228, 229]. Previously reported studies on collisions of He atoms with polar molecules revealed the presence of electric-field-induced resonances in low-energy scattering. The electric field mixes the rotational quantum numbers of the SrOH molecule due to the Stark effect, and in this process, the hyperfine effects should be just spectators. Again, a densely congested spectrum of bound states should facilitate the emergence of resonances.

Further investigations of suggested mechanisms are needed, including close-coupling equations and ab-initio studies of geometry-dependent coupling terms.

6.5 Chapter summary

Motivated by the growing interest in cooling and trapping polyatomic molecules, a theoretical investigation of the interactions between SrOH and alkaline-earth-like atoms was carried out. These systems are central to state-of-the-art precision-spectroscopy experiments; controlled assembly by linking SrOH with an alkaline-earth metal atom via electromagnetic fields could open access to a new class of molecules with interesting and structural properties, like near-symmetric tops. By analogy to alkali-metal dimers, such species may also serve as platforms for studies of ultracold chemical reactions and few-body dynamics.

Quantum scattering calculations using scaled interaction potentials demonstrated that anisotropy gives rise to an exceptionally dense resonance spectrum. The high resonance density arises from the involvement of numerous rotationally excited levels of SrOH and the strong anisotropy of the interactions. The bound state positions exhibit quantum chaos, with the Brody distribution almost matching the Wigner-Dyson case.

In conclusion, the Sr–SrOH system combines favorable trapping and stability properties with strong anisotropy, enabling both precise control of ultracold collisions and the potential creation of asymmetric top molecules in the ground state. The detailed PESs, scattering predictions, and excited-state characterizations provide a quantitative foundation for upcoming experimental efforts in this direction.

CHAPTER 7

Summary and future prospects

Ultracold-matter research has accelerated remarkably in recent years. A landmark is the first Bose–Einstein condensate of ground-state NaCs molecules from the Will group, alongside progress on continuous BECs, conveyor-belt MOT loading, and unprecedented control of collisions and spatial structure using optical-tweezer arrays.New types of species, like highly magnetic atoms and polyatomic molecules, broaden the range of constituents available in the ultracold regime. With new applications emerging, like quantum computing and simulations, high-resolution spectroscopy and measurements, and researchers looking for new physics, one can be sure of further breakthroughs in this field in the upcoming years.

The motivation for this dissertation was to gain an understanding of Feshbach resonances in complex, ultracold systems and, in particular, their decaying nature in complex systems. Various questions were stated regarding their usefulness, controllability, and importance.

This work presents theoretical studies conducted in several molecular systems. Each of the molecule types was reviewed, exposing their significance, progress made by other researchers, giving motivation for investigation, stating key goals, and putting the research in context. Theoretical methods were explained in detail, and computational procedures were described.

The second chapter focused on the interactions of nitrosonium and hydrogen. Bound state energies were calculated to supplement the results of the potential energy surface obtained. Their structure and dependence on total angular momentum were described. The molecule was characterised by the asymmetric top model, and its key spectroscopic parameters were derived from the behaviour of bound states. This chapter not only complements the work of researchers but also provides a foundation for mastering aspects used later in this thesis.

The third chapter is a summary of an ongoing study of helium and lithium. Numerical methods were implemented and tested to build a framework for computations incorporating complex optical potentials for which we used empirically derived parameters. As for certain collision energies, bound states of excited He+Li might be coupled to the continuum, and decaying Feshbach resonances emerge, allowing processes, like Penning ionization, to associate the atoms. Such resonant features were observed, confirming the tunability of the resonances and showing potential

The fourth and fifth chapters discussed the research in systems of lithium and erbium, and potassium and dysprosium. Those two systems of molecules consisting of a light alkali metal and a heavy, anisotropic, highly magnetic lanthanide proved to show some level of resemblance, yet have distinct characteristics. Feshbach resonances were described, and their behaviour explained. Excited states of lithium and erbium, with different mechanisms underlying the couplings, exhibit different widths, lifetimes, and

distributions of the resonances, while they remain relatively regular, with pronounced features. In dysprosium and potassium, the spectra are denser and chaotic. In excited potassium states, results exhibited minor changes, while excited dysprosium profiles were altered radically. The resonances were not only proven to be lossy in the case of excited dysprosium, but the results also point to the possibility that they might be controllable in different states. Chapter 5 also discusses the potential applications for the lossy resonances, where the accompanying dissipation could be utilized and considered a desirable *feature*, not a *bug*: one could introduce the model Hamiltonian where dissipation is present and well-controlled.

The collisions of strontium and strontium monohydroxide were the subject of the last chapter. A large number of densely laid out resonances as a function of potential scaling parameter were observed in the ground state, as well as a chaotic distribution of bound states. They were shown to be sensitive to interaction potential changes. The results strongly indicate that resonance in this system is related to the molecules' anisotropies. Understanding the coupling mechanisms between the states is crucial to predicting molecular formation and the Feshbach resonances responsible for it. It should be emphasized, however, that a very high density of states is a necessary, but not sufficient, condition for the Feshbach resonances. Possible scenarios for the mechanisms linking the states in these systems have been outlined. In addition to the small coupling for magnetic Feshbach resonances, the electric field may be considered as a means of manipulating the scattering properties in the ultracold Sr and SrOH mixture. Future studies of collisions in electric fields are therefore necessary.

In conclusion, the field of ultracold physics is rapidly evolving, offering numerous opportunities for discoveries. In the quantum world, unique phenomena, such as Feshbach resonances, emerge. These resonances are among the mechanisms underlying chemical processes and, more importantly, they provide tunability and controllability, making their understanding essential. By studying various types of resonances, this work not only deepened our comprehension but also highlighted experimental possibilities and provided groundwork for further research.

Bibliography

[1] G. Quéméner and P. S. Julienne, "Ultracold molecules under control!," *Chem. Rev.*, vol. 112, no. 9, pp. 4949–5011, 2012.

[2] C. Chin, V. V. Flambaum, and M. G. Kozlov, "Ultracold molecules: new probes on the variation of fundamental constants," *New J. Phys.*, vol. 11, p. 055048, 2009.

[3] J. M. Hutson, "Feshbach resonances in ultracold atomic and molecular collisions: threshold behaviour and suppression of poles in scattering lengths," *New J. Phys.*, vol. 9, no. 5, pp. 152–152, 2007.

[4] S. Inouye, M. R. Andrews, J. Stenger, H. J. Miesner, D. M. Stamper-Kurn, and W. Ketterle, "Observation of Feshbach resonances in a Bose-Einstein condensate," *Nature*, vol. 392, no. 6672, pp. 151–154, 1998.

[5] K. B. Davis, M. O. Mewes, M. R. Andrews, N. J. van Druten, D. S. Durfee, D. M. Kurn, and W. Ketterle, "Bose-einstein condensation in a gas of sodium atoms," *Phys. Rev. Lett.*, vol. 75, no. 22, pp. 3969–3973, 1995.

[6] M. H. Anderson, J. R. Ensher, M. R. Matthews, C. E. Wieman, and E. A. Cornell, "Observation of bose-einstein condensation in a dilute atomic vapor," *Science*, vol. 269, no. 5221, pp. 198–201, 1995.

[7] W. Ketterle, "Nobel lecture: When atoms behave as waves: Bose-einstein condensation and the atom laser," *Rev. Mod. Phys.*, vol. 74, no. 4, pp. 1131–1151, 2002.

[8] E. A. Cornell and C. E. Wieman, "Nobel lecture: Bose-einstein condensation in a dilute gas, the first 70 years and some recent experiments," *Rev. Mod. Phys.*, vol. 74, no. 3, pp. 875–893, 2002.

[9] A. Griesmaier, J. Werner, S. Hensler, J. Stuhler, and T. Pfau, "Bose-einstein condensation of chromium," *Phys. Rev. Lett.*, vol. 94, no. 16, p. 160401, 2005.

[10] K. Aikawa, A. Frisch, M. Mark, S. Baier, A. Rietzler, R. Grimm, and F. Ferlaino, "Bose-einstein condensation of erbium," *Phys. Rev. Lett.*, vol. 108, no. 21, p. 210401, 2012.

[11] I. Georgescu, "25 years of bec," *Nat. Rev. Phys.*, vol. 2, no. 8, pp. 396–396, 2020.

[12] B. DeMarco and D. S. Jin, "Onset of fermi degeneracy in a trapped atomic gas," *science*, vol. 285, no. 5434, pp. 1703–1706, 1999.

[13] C. Regal, M. Greiner, and D. S. Jin, "Observation of resonance condensation of fermionic atom pairs," *Phys. Rev. Lett.*, vol. 92, no. 4, p. 040403, 2004.

[14] C.-C. Chen, R. González Escudero, J. Minář, B. Pasquiou, S. Bennetts, and F. Schreck, "Continuous bose–einstein condensation," *Nature*, vol. 606, no. 7915, pp. 683–687, 2022.

[15] N. Bigagli, W. Yuan, S. Zhang, B. Bulatovic, T. Karman, I. Stevenson, and S. Will, "Observation of bose–einstein condensation of dipolar molecules," *Nature*, vol. 631, no. 8020, pp. 289–293, 2024.

[16] M. C. Asplund, J. A. Johnson, and J. E. Patterson, "The 2018 nobel prize in physics: optical tweezers and chirped pulse amplification," *Analytical and bioanalytical chemistry*, vol. 411, no. 20, pp. 5001–5005, 2019.

[17] W. Paul, "Electromagnetic traps for charged and neutral particles (nobel lecture)," *Angewandte Chemie International Edition in English*, vol. 29, no. 7, pp. 739–748, 1990.

[18] W. D. Phillips, "Laser cooling and trapping of neutral atoms," *Rev. Mod. Phys.*, vol. 70, pp. 721–741, JUL 1998.

[19] P. S. Julienne, "Ultracold molecules from ultracold atoms: a case study with the krb molecule," *Faraday discuss.*, vol. 142, pp. 361–388, 2009.

[20] D. J. Wineland, "Nobel lecture: Superposition, entanglement, and raising schrödinger's cat," *Rev. Mod. Phys.*, vol. 85, no. 3, pp. 1103–1114, 2013.

[21] S. Will and T. Zelevinsky, "Ultracold molecules find the sweet spot for collisions," 2023.

[22] I. Bloch, J. Dalibard, and W. Zwerger, "Many-body physics with ultracold gases," *Rev. Mod. Phys.*, vol. 80, no. 3, pp. 885–964, 2008.

[23] S. Truppe, R. Hendricks, S. Tokunaga, H. Lewandowski, M. Kozlov, C. Henkel, E. Hinds, and M. Tarbutt, "A search for varying fundamental constants using hertz-level frequency measurements of cold ch molecules," *Nat. Commun.*, vol. 4, no. 1, p. 2600, 2013.

[24] A. collaboration, J. Baron, W. Campbell, D. DeMille, J. Doyle, G. Gabrielse, Y. Gurevich, P. Hess, N. Hutzler, E. Kirilov, *et al.*, "Order of magnitude smaller limit on the electric dipole moment of the electron," *Science*, vol. 343, no. 6168, pp. 269–272, 2014.

[25] P. Wcisło, P. Morzyński, M. Bober, A. Cygan, D. Lisak, R. Ciuryło, and M. Zawada, "Experimental constraint on dark matter detection with optical atomic clocks," *Nat. Astron*, vol. 1, p. 0009, Dec 2016.

[26] P. Wcisło, P. Ablewski, K. Beloy, S. Bilicki, M. Bober, R. Brown, R. Fasano, R. Ciuryło, H. Hachisu, T. Ido, *et al.*, "New bounds on dark matter coupling from a global network of optical atomic clocks," *Sci. Adv.*, vol. 4, no. 12, p. eaau4869, 2018.

[27] M. Takamoto, F.-L. Hong, R. Higashi, and H. Katori, "An optical lattice clock," *Nature*, vol. 435, no. 7040, pp. 321–324, 2005.

[28] A. D. Ludlow, T. Zelevinsky, G. Campbell, S. Blatt, M. Boyd, M. H. de Miranda, M. Martin, J. Thomsen, S. M. Foreman, J. Ye, *et al.*, "Sr lattice clock at $1\times$ 10–16 fractional uncertainty by remote optical evaluation with a ca clock," *Science*, vol. 319, no. 5871, pp. 1805–1808, 2008.

[29] R. Le Targat, L. Lorini, Y. Le Coq, M. Zawada, J. Guéna, M. Abgrall, M. Gurov, P. Rosenbusch, D. Rovera, B. Nagórny, *et al.*, "Experimental realization of an optical second with strontium lattice clocks," *Nat. Commun.*, vol. 4, no. 1, p. 2109, 2013.

[30] G. E. Marti, R. B. Hutson, A. Goban, S. L. Campbell, N. Poli, and J. Ye, "Imaging optical frequencies with 100 μ hz precision and 1.1 μ m resolution," *Phys. Rev. Lett.*, vol. 120, no. 10, p. 103201, 2018.

[31] T. Zelevinsky, S. Kotochigova, and J. Ye, "Precision Test of Mass-Ratio Variations with Lattice-Confined Ultracold Molecules," *Phys. Rev. Lett.*, vol. 100, p. 043201, 2008.

[32] D. DeMille, "Quantum computation with trapped polar molecules," *Phys. Rev. Lett.*, vol. 88, p. 067901, 2002.

[33] H. P. Büchler, E. Demler, M. Lukin, A. Micheli, N. Prokof'ev, G. Pupillo, and P. Zoller, "Strongly correlated 2d quantum phases with cold polar molecules: Controlling the shape of the interaction potential," *Phys. Rev. Lett.*, vol. 98, p. 060404, 2007.

[34] M. A. Baranov, M. Dalmonte, G. Pupillo, and P. Zoller, "Condensed matter theory of dipolar quantum gases," *Chemical Reviews*, vol. 112, no. 9, pp. 5012–5061, 2012.

[35] S. Chu, "The manipulation of neutral particles," *Rev. Mod. Phys.*, vol. 70, pp. 685–706, JUL 1998.

[36] L. Caldwell, J. A. Devlin, H. J. Williams, N. J. Fitch, E. A. Hinds, B. E. Sauer, and M. R. Tarbutt, "Deep laser cooling and efficient magnetic compression of molecules," *Phys. Rev. Lett.*, vol. 123, p. 033202, Jul 2019.

[37] H. T. C. Stoof, "Breaking up a superfluid," *Nature*, vol. 415, no. 6867, pp. 25–26, 2002.

[38] J. M. Hutson and P. Soldán, "Molecule formation in ultracold atomic gases," *IRPC*, vol. 25, no. 4, pp. 497–526, 2006.

[39] J. F. Barry, D. McCarron, E. Norrgard, M. Steinecker, and D. DeMille, "Magneto-optical trapping of a diatomic molecule," *Nature*, vol. 512, p. 286, 2014.

[40] R. Grimm, M. Weidemüller, and Y. B. Ovchinnikov, "Optical dipole traps for neutral atoms," pp. 95–170, 2000.

[41] C. N. Cohen-Tannoudji, "Manipulating atoms with photons," *Rev. Mod. Phys.*, vol. 70, pp. 707–719, JUL 1998.

[42] I. Kozyryev, L. Baum, K. Matsuda, B. L. Augenbraun, L. Anderegg, A. P. Sedlack, and J. M. Doyle, "Sisyphus laser cooling of a polyatomic molecule," *Phys. Rev. Lett.*, vol. 118, p. 173201, Apr 2017.

[43] B. L. Augenbraun, Z. D. Lasner, A. Frenett, H. Sawaoka, C. Miller, T. C. Steimle, and J. M. Doyle, "Laser-cooled polyatomic molecules for improved electron electric dipole moment searches," *New Journal of Physics*, vol. 22, no. 2, p. 022003, 2020.

[44] D. Mitra, N. B. Vilas, C. Hallas, L. Anderegg, B. L. Augenbraun, L. Baum, C. Miller, S. Raval, and J. M. Doyle, "Direct laser cooling of a symmetric top molecule," *Science*, vol. 369, no. 6508, pp. 1353–1356, 2020.

[45] W. Ketterle and N. V. Druten, "Evaporative cooling of trapped atoms," pp. 181–236, 1996.

[46] N. Masuhara, J. M. Doyle, J. C. Sandberg, D. Kleppner, T. J. Greytak, H. F. Hess, and G. P. Kochanski, "Evaporative cooling of spin-polarized atomic-hydrogen," *Phys. Rev. Lett.*, vol. 61, pp. 935–938, AUG 1988.

[47] W. Petrich, M. H. Anderson, J. R. Ensher, and E. A. Cornell, "Stable, tight confining magnetic trap for evapoative cooling of neutral atoms," *Phys. Rev. Lett.*, vol. 74, p. 3352, 1995.

[48] N. R. Hutzler, H.-I. Lu, and J. M. Doyle, "The buffer gas beam: An intense, cold, and slow source for atoms and molecules," *Chem. Rev.*, vol. 112, no. 9, pp. 4803–4827, 2012.

[49] H. L. Bethlem, A. J. A. van Roij, R. T. Jongma, and G. Meijer, "Alternate gradient focusing and deceleration of a molecular beam," *Phys. Rev. Lett.*, vol. 88, p. 133003, APR 2002.

[50] M. R. Tarbutt, H. L. Bethlem, J. J. Hudson, V. L. Ryabov, V. A. Ryzhov, B. E. Sauer, G. Meijer, and E. A. Hinds, "Slowing heavy, ground-state molecules using an alternating gradient decelerator," *Phys. Rev. Lett.*, vol. 92, p. 173002, APR 2004.

[51] R. V. Krems, *Molecules in electromagnetic fields: from ultracold physics to controlled chemistry*. John Wiley & Sons, 2018.

[52] H. Son, J. J. Park, W. Ketterle, and A. O. Jamison, "Collisional cooling of ultracold molecules," *Nature*, vol. 580, no. 7802, pp. 197–200, 2020.

[53] J. Lim, J. Almond, M. Trigatzis, J. Devlin, N. Fitch, B. Sauer, M. Tarbutt, and E. Hinds, "Laser cooled ybf molecules for measuring the electron's electric dipole moment," *Phys. Rev. Lett.*, vol. 120, no. 12, p. 123201, 2018.

[54] E. S. Shuman, J. F. Barry, and D. DeMille, "Laser cooling of a diatomic molecule," *Nature*, no. 467, p. 820, 2010.

[55] J. J. Park, Y.-K. Lu, A. O. Jamison, and W. Ketterle, "Magnetic trapping of ultracold molecules at high density," *Nature Physics*, vol. 19, pp. 1567–1572, 2023.

[56] L. Anderegg, L. W. Cheuk, Y. Bao, S. Burchesky, W. Ketterle, K.-K. Ni, and J. M. Doyle, "An optical tweezer array of ultracold molecules," *Science*, vol. 365, pp. 1156–1158, 2019.

[57] S. Truppe, H. J. Williams, M. Hambach, L. Caldwell, N. J. Fitch, E. A. Hinds, B. E. Sauer, and M. R. Tarbutt, "Molecules cooled below the Doppler limit," *Nat. Phys.*, vol. 13, p. 1173, 2018.

[58] D. K. Ruttley, A. Guttridge, S. Spence, R. C. Bird, C. R. Le Sueur, J. M. Hutson, and S. L. Cornish, "Formation of ultracold molecules by merging optical tweezers," *Phys. Rev. Lett.*, vol. 130, p. 223401, May 2023.

[59] M. Tomza, F. Pawlowski, M. Jeziorska, C. P. Koch, and R. Moszynski, "Formation of ultracold sryb molecules in an optical lattice by photoassociation spectroscopy: theoretical prospects," *Phys. Chem. Chem. Phys.*, vol. 13, pp. 18893–18904, 2011.

[60] M. Kitagawa, K. Enomoto, K. Kasa, Y. Takahashi, R. Ciuryło, P. Naidon, and P. S. Julienne, "Two-color photoassociation spectroscopy of ytterbium atoms and the precise determinations of s-wave scattering lengths," *Phys. Rev. A*, vol. 77, p. 012719, Jan 2008.

[61] K.-K. Ni, S. Ospelkaus, M. De Miranda, A. Pe'Er, B. Neyenhuis, J. Zirbel, S. Kotochigova, P. Julienne, D. Jin, and J. Ye, "A high phase-space-density gas of polar molecules," *Science*, vol. 322, no. 5899, pp. 231–235, 2008.

[62] T. Köhler, K. Góral, and P. S. Julienne, "Production of cold molecules via magnetically tunable feshbach resonances," *Rev. Mod. Phys.*, vol. 78, no. 4, pp. 1311–1361, 2006.

[63] K.-K. Ni, S. Ospelkaus, D. Wang, G. Quéméner, B. Neyenhuis, M. H. G. de Miranda, J. L. Bohn, J. Ye, and D. S. Jin, "Dipolar collisions of polar molecules in the quantum regime," *Nature*, vol. 464, pp. 1324–1328, Apr 2010.

[64] M. T. Hummon, M. Yeo, B. K. Stuhl, A. L. Collopy, Y. Xia, and J. Ye, "2d magneto-optical trapping of diatomic molecules," *Phys. Rev. Lett.*, vol. 110, no. 14, p. 143001, 2013.

[65] D. Grün, L. B. Giacomelli, A. Tashchilina, R. Donofrio, F. Borchers, T. Bland, M. Mark, and F. Ferlaino, "Light-assisted collisions in tweezer-trapped lanthanides," *arXiv preprint arXiv:2506.05123*, 2025.

[66] Y. Bao, S. S. Yu, L. Anderegg, E. Chae, W. Ketterle, K.-K. Ni, and J. M. Doyle, "Dipolar spin-exchange and entanglement between molecules in an optical tweezer array," *Science*, vol. 382, p. 1138, 2023.

[67] L. Anderegg, S. Burchesky, Y. Bao, S. S. Yu, T. Karman, E. Chae, K.-K. Ni, W. Ketterle, and J. M. Doyle, "Observation of microwave shielding of ultracold molecules," *Science*, vol. 373, pp. 779–782, Aug 2021.

[68] R. C. Bird, C. R. Le Sueur, and J. M. Hutson, "Making molecules by mergoassociation: Two atoms in adjacent nonspherical optical traps," *Phys. Rev. Res.*, vol. 5, p. 043086, Oct 2023.

[69] Y. Kiefer, M. Hachmann, and A. Hemmerich, "Ultracold feshbach molecules in an orbital optical lattice," *Nat. Phys.*, vol. 19, no. 6, pp. 794–799, 2023.

[70] P. Paliwal, N. Deb, D. M. Reich, A. v. d. Avoird, C. P. Koch, and E. Narevicius, "Determining the nature of quantum resonances by probing elastic and reactive scattering in cold collisions," *Nat. Chem.*, vol. 13, no. 1, pp. 94–98, 2021.

[71] L. Piela, *Ideas of quantum chemistry*. Elsevier, 2006.

[72] S. Knoop, T. Schuster, R. Scelle, A. Trautmann, J. Appmeier, M. K. Oberthaler, E. Tiesinga, and E. Tiemann, "Feshbach spectroscopy and analysis of the interaction potentials of ultracold sodium," *Phys. Rev. A: At. Mol. Opt. Phys.*, vol. 83, no. 4, p. 042704, 2011.

[73] J. De Paula, *Atkins' Physical Chemistry*. Oxford University Press, 2010.

[74] J. Callaway and E. Bauer, "Inelastic collisions of slow atoms," *Phys. Rev.*, vol. 140, no. 4A, p. A1072, 1965.

[75] C. Chin, R. Grimm, P. Julienne, and E. Tiesinga, "Feshbach resonances in ultracold gases," *Rev. Mod. Phys.*, vol. 82, no. 2, pp. 1225–1286, 2010.

[76] J. M. Hutson, "Theory of cold atomic and molecular collisions," in *Cold Molecules: Theory, Experiment, Applications* (R. V. Krems, W. C. Stwalley, and B. Friedrich, eds.), pp. 3–37, Boca Raton: CRC Press, 2009.

[77] A. M. Arthurs and A. Dalgarno, "The theory of scattering by a rigid rotator," *Proc. Roy. Soc. (London Ser.)*, vol. A256, p. 540, 1960.

[78] M. H. Alexander, "Hybrid quantum scattering algorithms for long-range potentials," *J. Chem. Phys.*, vol. 81, p. 4510, 1984.

[79] M. H. Alexander and D. E. Manolopoulos, "A stable linear reference potential algorithm for solution of the quantum close-coupled equations in molecular scattering theory," *J. Chem. Phys.*, vol. 86, pp. 2044–2050, 1987.

[80] N. Moiseyev, *Non-Hermitian quantum mechanics*. Cambridge University Press, 2011.

[81] M. H. Alexander and A. R. Barrier, "Quantum molecular collision theory with problems based on matlab," 2023.

[82] B. R. Johnson, "The Multichannel Log-Derivative Method for Scattering Calculations," *J. Comp. Phys.*, vol. 13, p. 445, 1973.

[83] B. R. Johnson, "The renormalized numerov method applied to calculating bound states of the coupled-channel schroedinger equation," *J. Chem. Phys.*, vol. 69, no. 10, pp. 4678–4688, 1978.

[84] D. E. Manolopoulos, M. J. Jamieson, and A. D. Pradhan, "Johnson's log derivative algorithm rederived," *J. Comput. Phys.*, vol. 105, p. 169–172, 1993.

[85] J. M. Hutson and C. R. Le Sueur, "molscat: A program for non-reactive quantum scattering calculations on atomic and molecular collisions," *Comput. Phys. Commun.*, vol. 241, pp. 9–33, 2019.

[86] J. M. Hutson and C. R. Le Sueur, "Bound and Field: Programs for calculating bound states of interacting pairs of atoms and molecules," *Computer Physics Communications*, vol. 241, pp. 1–8, 2019.

[87] B. Johnson, "The log-derivative and renormalized numerov algorithms," *NRCC Proc. 5*, vol. 86, 1979.

[88] B. R. Johnson, "New numerical methods applied to solving the one-dimensional eigenvalue problem," *J. Chem. Phys.*, vol. 67, pp. 4086–4093, 11 1977.

[89] G. GAMOW, "Successive -transformations," *Nature*, vol. 123, no. 3103, pp. 606–606, 1929.

[90] M. Pawlak, Y. Shagam, E. Narevicius, and N. Moiseyev, "Adiabatic theory for anisotropic cold molecule collisions," *J. Chem. Phys.*, vol. 143, no. 7, 2015.

[91] M. Pawlak, P. S. Zuchowski, N. Moiseyev, and P. Jankowski, "Evidence of nonrigidity effects in the description of low-energy anisotropic molecular collisions of hydrogen molecules with excited metastable helium atoms," *J. Chem. Theory Comput.*, vol. 16, no. 4, pp. 2450–2459, 2020.

[92] S. Nandi, E. Plésiat, S. Zhong, A. Palacios, D. Busto, M. Isinger, L. Neoričić, C. Arnold, R. Squibb, R. Feifel, *et al.*, "Attosecond timing of electron emission from a molecular shape resonance," *Sci. Adv.*, vol. 6, no. 31, p. eaba7762, 2020.

[93] F. A. van Abeelen and B. J. Verhaar, "Time-dependent feshbach resonance scattering and anomalous decay of a na Bose-Einstein condensate," *Phys. Rev. Lett.*, vol. 83, pp. 1550–1553, AUG 1999.

[94] J. J. Park, Y.-K. Lu, A. O. Jamison, T. V. Tscherbul, and W. Ketterle, "A feshbach resonance in collisions between triplet ground-state molecules," *Nature*, vol. 614, no. 7946, pp. 54–58, 2023.

[95] X.-Y. Chen, A. Schindewolf, S. Eppelt, R. Bause, M. Duda, S. Biswas, T. Karman, T. Hilker, I. Bloch, and X.-Y. Luo, "Field-linked resonances of polar molecules," *Nature*, vol. 614, no. 7946, pp. 59–63, 2023.

[96] H. Son, J. J. Park, Y.-K. Lu, A. O. Jamison, T. Karman, and W. Ketterle, "Control of reactive collisions by quantum interference," *Science*, vol. 375, pp. 1006–1010, 2022.

[97] N. F. Mott and H. S. W. Massey, *The Theory of Atomic Collisions*. Oxford: Clarendon Press, 3rd ed., 1965.

[98] J. R. Taylor, *Scattering Theory: The Quantum Theory of Nonrelativistic Collisions*. New York: Wiley, 1972.

[99] J. Weiner, V. Bagnato, S. Zilio, and J. P.S., "Experiments and theory in cold and ultracold collisions," *Rev. Mod. Phys.*, vol. 71, pp. 1–85, 1999.

[100] P. S. Julienne and B. Gao, "Simple theoretical models for resonant cold atom interactions," *arXiv:physics/0609013*, 2006.

[101] A. J. Moerdijk, B. J. Verhaar, and A. Axelsson, "Resonances in ultracold collisions of ^{6}li, ^{7}li, and ^{23}na," *Phys. Rev. A*, vol. 51, pp. 4852–4861, JUN 1995.

[102] E. Timmermans, P. Tommasini, M. Hussein, and A. Kerman, "Feshbach resonances in atomic Bose-Einstein condensates," *Phys. Rep.*, vol. 315, pp. 199–230, JUL 1999.

[103] G. F. Gribakin and V. V. Flambaum, "Calculation of the scattering length in atomic collisions using the semiclassical approximation," *Phys. Rev. A*, vol. 48, pp. 546–553, Jul 1993.

[104] R. Ciuryło, E. Tiesinga, and P. S. Julienne, "Optical tuning of the scattering length of cold alkaline-earth-metal atoms," *Phys. Rev. A*, vol. 71, p. 030701, Mar 2005.

[105] X. Ye, M. Guo, M. L. González-Martínez, G. Quéméner, and D. Wang, "Collisions of ultracold 23na87rb molecules with controlled chemical reactivities," *Sci. Adv.*, vol. 4, no. 1, p. eaaq0083, 2018.

[106] J. F. Croft and J. L. Bohn, "Long-lived complexes, ergodicity and chaos in ultracold molecular collisions," *arXiv preprint arXiv:1311.0294*, 2013.

[107] A. Frisch, M. Mark, K. Aikawa, F. Ferlaino, J. L. Bohn, C. Makrides, A. Petrov, and S. Kotochigova, "Quantum chaos in ultracold collisions of gas-phase erbium atoms," *Nature*, vol. 507, p. 475, 2014.

[108] D. G. Green, C. L. Vaillant, M. D. Frye, M. Morita, and J. M. Hutson, "Quantum chaos in ultracold collisions between Yb($^1S_0$) and Yb($^3P_2$)," *Phys. Rev. A*, vol. 93, p. 022703, 2016.

[109] M. D. Frye, M. Morita, C. L. Vaillant, D. G. Green, and J. M. Hutson, "Approach to chaos in ultracold atomic and molecular physics: Statistics of near-threshold bound states for li+cah and li+caf," *Phys. Rev. A*, vol. 93, p. 052713, May 2016.

[110] M. B. Kosicki, M. Borkowski, and P. S. Żuchowski, "Quantum chaos in feshbach resonances of the eryb system," *New Journal of Physics*, vol. 22, no. 2, p. 023024, 2020.

[111] K. Zaremba-Kopczyk, P. S. Żuchowski, and M. Tomza, "Magnetically tunable feshbach resonances in ultracold gases of europium atoms and mixtures of europium and alkali-metal atoms," *Phys. Rev. A*, vol. 98, p. 032704, Sep 2018.

[112] O. Dutta, M. Gajda, P. Hauke, M. Lewenstein, D.-S. Lühmann, B. A. Malomed, T. Sowiński, and J. Zakrzewski, "Non-standard hubbard models in optical lattices: a review," *Rep. Prog. Phys.*, vol. 78, no. 6, p. 066001, 2015.

[113] F. Schäfer, T. Fukuhara, S. Sugawa, Y. Takasu, and Y. Takahashi, "Tools for quantum simulation with ultracold atoms in optical lattices," *Nat. Rev. Phys.*, vol. 2, no. 8, pp. 411–425, 2020.

[114] C. D. Bruzewicz, J. Chiaverini, R. McConnell, and J. M. Sage, "Trapped-ion quantum computing: Progress and challenges," *Appl. Phys. Rev.*, vol. 6, no. 2, 2019.

[115] S. Ebadi, T. T. Wang, H. Levine, A. Keesling, G. Semeghini, A. Omran, D. Bluvstein, R. Samajdar, H. Pichler, W. W. Ho, *et al.*, "Quantum phases of matter on a 256-atom programmable quantum simulator," *Nature*, vol. 595, no. 7866, pp. 227–232, 2021.

[116] S. Yelin, K. Kirby, and R. Côté, "Schemes for robust quantum computation with polar molecules," *Phys. Rev. A: At. Mol. Opt. Phys.*, vol. 74, no. 5, p. 050301, 2006.

[117] E. Kuznetsova, T. Bragdon, R. Côté, and S. Yelin, "Cluster-state generation using van der waals and dipole-dipole interactions in optical lattices," *Phys. Rev. A: At. Mol. Opt. Phys.*, vol. 85, no. 1, p. 012328, 2012.

[118] T. Wall, "Preparation of cold molecules for high-precision measurements," *Journal of Physics B: Atomic, Molecular and Optical Physics*, vol. 49, no. 24, p. 243001, 2016.

[119] R. A. Hart, X. Xu, R. Legere, and K. Gibble, "A quantum scattering interferometer," *Nature*, vol. 446, pp. 892–895, 2007.

[120] A. Ciamei, A. Koza, M. Gronowski, and M. Tomza, "Ultracold high-spin -state polar molecules for new physics searches," 2025.

[121] P. Yu and N. R. Hutzler, "Probing fundamental symmetries of deformed nuclei in symmetric top molecules," *Phys. Rev. Lett.*, vol. 126, p. 023003, Jan 2021.

[122] J. Kłos, E. Tiesinga, L. Cheng, and S. Kotochigova, "Anisotropic chemical bonding of lanthanide-oh molecules," *Scientific Reports*, vol. 15, p. 21480, 2025.

[123] C. Chin and V. V. Flambaum, "Enhanced Sensitivity to Fundamental Constants In Ultracold Atomic and Molecular Systems near Feshbach Resonances," *Phys. Rev. Lett.*, vol. 96, p. 230801, Jun 2006.

[124] D. DeMille, S. Sainis, J. Sage, T. Bergeman, S. Kotochigova, and E. Tiesinga, "Enhanced Sensitivity to Variation of m_e/m_p in Molecular Spectra," *Phys. Rev. Lett.*, vol. 100, p. 043202, 2008.

[125] V. Andreev, D. Ang, D. DeMille, J. Doyle, G. Gabrielse, J. Haefner, N. Hutzler, Z. Lasner, C. Meisenhelder, B. O'Leary, C. Panda, A. West, E. West, and X. Wu, "Improved limit on the electric dipole moment of the electron," *Nature*, vol. 562, no. 7727, pp. 355–360, 2018.

[126] J. J. Hudson, D. M. Kara, I. Smallman, B. E. Sauer, M. R. Tarbutt, and E. A. Hinds, "Improved measurement of the shape of the electron," *Nature*, vol. 473, no. 7348, pp. 493–496, 2011.

[127] M. R. Tarbutt, B. E. Sauer, J. J. Hudson, and E. A. Hinds, "Design for a fountain of YbF molecules to measure the electron's electric dipole moment," *New J. Phys.*, vol. 15, p. 053034, May 2013.

[128] T. Karman, M. Tomza, and J. Pérez-Ríos, "Ultracold chemistry as a testbed for few-body physics," *Nat. Phys.*, vol. 20, no. 5, pp. 722–729, 2024.

[129] S. Jurgilas, A. Chakraborty, C. Rich, L. Caldwell, H. Williams, N. Fitch, B. Sauer, M. D. Frye, J. M. Hutson, and M. Tarbutt, "Collisions between ultracold molecules and atoms in a magnetic trap," *Phys. Rev. Lett.*, vol. 126, no. 15, p. 153401, 2021.

[130] P. Weckesser, F. Thielemann, D. Wiater, A. Wojciechowska, L. Karpa, K. Jachymski, M. Tomza, T. Walker, and T. Schaetz, "Observation of feshbach resonances between a single ion and ultracold atoms," *Nature*, vol. 600, no. 7889, pp. 429–433, 2021.

[131] M. Tomza, K. Jachymski, R. Gerritsma, A. Negretti, T. Calarco, Z. Idziaszek, and P. S. Julienne, "Cold hybrid ion-atom systems," *Rev. Mod. Phys.*, vol. 91, no. 3, p. 035001, 2019.

[132] P. Naidon and S. Endo, "Efimov physics: a review," *Rep. Prog. Phys.*, vol. 80, no. 5, p. 056001, 2017.

[133] T. Maier, H. Kadau, M. Schmitt, M. Wenzel, I. Ferrier-Barbut, T. Pfau, A. Frisch, S. Baier, K. Aikawa, L. Chomaz, M. J. Mark, F. Ferlaino, C. Makrides, E. Tiesinga, A. Petrov, and S. Kotochigova, "Emergence of chaotic scattering in ultracold er and dy," *Phys. Rev. X*, vol. 5, p. 041029, 2015.

[134] L. Chomaz, I. Ferrier-Barbut, F. Ferlaino, B. Laburthe-Tolra, B. L. Lev, and T. Pfau, "Dipolar physics: a review of experiments with magnetic quantum gases," *Rep. Prog. Phys.*, vol. 86, no. 2, p. 026401, 2022.

[135] A. Petrov, E. Tiesinga, and S. Kotochigova, "Anisotropy-induced feshbach resonances in a quantum dipolar gas of highly magnetic atoms," *Phys. Rev. Lett.*, vol. 109, p. 103002, Sep 2012.

[136] D. Albritton, A. Schmeltekopf, and R. Zare, "Potential energy curves for no+," *J. Chem. Phys.*, vol. 71, no. 8, pp. 3271–3279, 1979.

[137] M. Oppenheimer, A. Dalgarno, F. Trebino, L. Brace, H. Brinton, and J. Hoffman, "Daytime chemistry of no+ from atmosphere explorer-c measurements," *J. Geophys. Res.*, vol. 82, no. 1, pp. 191–194, 1977.

[138] E. Herbst and E. F. Van Dishoeck, "Complex organic interstellar molecules," *Annu. Rev. Astron. Astrophys.*, vol. 47, no. 1, pp. 427–480, 2009.

[139] J. Pickles and D. Williams, "Model for surface reactions on interstellar grains—a numerical study," *Astrophys. Space Sci.*, vol. 52, no. 2, pp. 443–452, 1977.

[140] J. Cernicharo, S. Bailleux, E. Alekseev, A. Fuente, E. Roueff, M. Gerin, B. Tercero, S. Treviño-Morales, N. Marcelino, R. Bachiller, *et al.*, "Tentative detection of the nitrosylium ion in space," *Astrophys. J.*, vol. 795, no. 1, p. 40, 2014.

[141] I. Fourré and M. Raoult, "Vibrational structure of the ar no+ van der waals cation," *Chem. Phys.*, vol. 199, no. 2-3, pp. 215–225, 1995.

[142] C. Orek, J. Kłos, F. Lique, and N. Bulut, "Ab initio studies of the rg–no+ (x1σ+) van der waals complexes (rg= he, ne, ar, kr, and xe)," *J. Chem. Phys.*, vol. 144, no. 20, 2016.

[143] A. Viggiano, R. Morris, F. Dale, J. Paulson, and E. Ferguson, "Vibrational quenching of no+ (v) ions in collision with h2, d2, and o2," *J. Chem. Phys.*, vol. 90, no. 3, pp. 1648–1651, 1989.

[144] L. Cabrera-González, D. Páez-Hernández, and O. Denis-Alpizar, "Relaxation of no+ by collision with para-h2 (j= 0)," *Monthly Notices of the Royal Astronomical Society*, vol. 494, no. 1, pp. 129–134, 2020.

[145] C. Orek, M. Umiński, J. Kłos, F. Lique, P. S. Zuchowski, and N. Bulut, "No++ h2: Potential energy surface and bound state calculations," *Chem. Phys. Lett.*, vol. 771, p. 138511, 2021.

[146] J. M. Hutson and C. R. Le Sueur, "Molscat: A program for non-reactive quantum scattering calculations on atomic and molecular collisions," *Computer Physics Communications*, vol. 241, pp. 9–18, 2019.

[147] M. Karplus, M. Levitt, and A. Warshel, "The nobel prize in chemistry 2013," *Nobel Media AB 2014*, 2013.

[148] M. Movre, L. Thiel, and W. Meyer, "Theoretical investigation of the autoionization process in molecular collision complexes: He*(2 3 s)+ li (2 2 s)$\rightarrow$ he+ li++ e-," *J. Chem. Phys.*, vol. 113, no. 4, pp. 1484–1491, 2000.

[149] W. Skomorowski, Y. Shagam, E. Narevicius, and C. P. Koch, "Photoassociation spectroscopy in penning ionization reactions at sub-kelvin temperatures," *J. Phys. Chem. A*, vol. 120, no. 19, pp. 3309–3315, 2016.

[150] J. J. Omiste, J. Floß, and P. Brumer, "Coherent control of penning and associative ionization: Insights from symmetries," *Phys. Rev. Lett.*, vol. 121, no. 16, p. 163405, 2018.

[151] C. Makrides, D. S. Barker, J. A. Fedchak, J. Scherschligt, S. Eckel, and E. Tiesinga, "Collisions of room-temperature helium with ultracold lithium and the van der waals bound state of heli," *Phys. Rev. A*, vol. 101, no. 1, p. 012702, 2020.

[152] J. Grzesiak, T. Momose, F. Stienkemeier, M. Mudrich, and K. Dulitz, "Penning collisions between supersonically expanded metastable he atoms and laser-cooled li atoms," *J. Chem. Phys.*, vol. 150, no. 3, 2019.

[153] K. Dulitz, T. Sixt, J. Guan, J. Grzesiak, M. Debatin, and F. Stienkemeier, "Suppression of penning ionization by orbital angular momentum conservation," *Phys. Rev. A*, vol. 102, no. 2, p. 022818, 2020.

[154] K. Dulitz, T. Sixt, J. Guan, J. Grzesiak, M. Debatin, and F. Stienkemeier, "Control of he*-li chemi-ionization," in *APS Division of Atomic, Molecular and Optical Physics Meeting Abstracts*, vol. 2022, pp. S11–002, 2022.

[155] P. Siska, "Molecular-beam studies of penning ionization," *Rev. Mod. Phys.*, vol. 65, no. 2, p. 337, 1993.

[156] H. Hotop, T. Roth, M.-W. Ruf, and A. Yencha, "Diatomic potential well depths from analyses of high-resolution electron energy spectra for autoionizing collision complexes," *Theor. Chem. Acc.*, vol. 100, no. 1, pp. 36–50, 1998.

[157] D. Kędziera, Ł. Mentel, P. S. Żuchowski, and S. Knoop, "Ab initio interaction potentials and scattering lengths for ultracold mixtures of metastable helium and alkali-metal atoms," *Phys. Rev. A*, vol. 91, no. 6, p. 062711, 2015.

[158] B. M. Smirnov and M. I. Chibisov *Sov. Phys. JETP*, vol. 21, p. 624, 1965.

[159] M.-W. Ruf, A. Yencha, and H. Hotop, "The interaction of metastable helium atoms with alkali atoms," *Zeitschrift für Physik D Atoms, Molecules and Clusters*, vol. 5, no. 1, pp. 9–20, 1987.

[160] A. Merz, M. Müller, M.-W. Ruf, H. Hotop, W. Mayer, and M. Movre, "Experimental and theoretical studies of simple attractive penning ionization systemsag," *Chem. Phys.*, vol. 145, no. 2, pp. 219–238, 1990.

[161] J. Emsley, *The Elements*. Oxford Chemistry Guides, New York, NY: Oxford University Press, 1995.

[162] E. Arimondo, M. Inguscio, and P. Violino, "Experimental determinations of the hyperfine structure in the alkali atoms," *Rev. Mod. Phys.*, vol. 49, no. 1, p. 31, 1977.

[163] J. M. Hutson, E. Tiesinga, and P. S. Julienne, "Avoided crossings between bound states of ultracold Cesium dimers," *Phys. Rev. A*, vol. 78, p. 052703, 2008.

[164] M. L. González-Martínez and P. S. Żuchowski, "Magnetically tunable feshbach resonances in li+ er," *Phys. Rev. A*, vol. 92, no. 2, p. 022708, 2015.

[165] F. Schäfer, N. Mizukami, and Y. Takahashi, "Feshbach resonances of large-mass-imbalance er-li mixtures," *Phys. Rev. A*, vol. 105, no. 1, p. 012816, 2022.

[166] F. Schäfer, Y. Haruna, and Y. Takahashi, "Observation of feshbach resonances in an 167er–6li fermi–fermi mixture," *J. Phys. Soc. Jpn.*, vol. 92, no. 5, p. 054301, 2023.

[167] D. Grün, S. White, A. Ortu, A. Di Carli, H. Edri, M. Lepers, M. Mark, and F. Ferlaino, "Optical tweezer arrays of erbium atoms," *Phys. Rev. Lett.*, vol. 133, no. 22, p. 223402, 2024.

[168] J. Kalia, J. Rivera, R. R. Emran, W. J. S. Hernandez, K. Kwon, and R. J. Fletcher, "Creation of a degenerate bose-bose mixture of erbium and lithium atoms," 2025.

[169] K. Xie, X. Li, Y.-Y. Zhou, J.-H. Luo, S. Wang, Y.-Z. Nie, H.-C. Shen, Y.-A. Chen, X.-C. Yao, and J.-W. Pan, "Feshbach spectroscopy of ultracold mixtures of li6 and dy164 atoms," *Phys. Rev. A*, vol. 111, no. 2, p. 023327, 2025.

[170] N. Craig, J. Taylor, E. Lester, C. Marcus, M. Hanson, and A. Gossard, "Tunable nonlocal spin control in a coupled-quantum dot system," *Science*, vol. 304, no. 5670, pp. 565–567, 2004.

[171] G. Zürn, A. Wenz, S. Murmann, A. Bergschneider, T. Lompe, and S. Jochim, "Pairing in few-fermion systems with attractive interactions," *Phys. Rev. Lett.*, vol. 111, no. 17, p. 175302, 2013.

[172] A. Amaricci, A. Richaud, M. Capone, N. D. Oppong, and F. Scazza, "Engineering the kondo impurity problem with alkaline-earth atom arrays," *arXiv preprint arXiv:2505.14630*, 2025.

[173] G. Zürn, T. Lompe, A. N. Wenz, S. Jochim, P. Julienne, and J. Hutson, "Precise characterization of li 6 feshbach resonances using trap-sideband-resolved<? format?> rf spectroscopy of weakly bound molecules," *Phys. Rev. Lett.*, vol. 110, no. 13, p. 135301, 2013.

[174] M. L. González-Martínez and J. M. Hutson, "Sympathetic cooling of fluorine atoms with ultracold atomic hydrogen," *Phys. Rev. A*, vol. 88, p. 053420, Nov 2013.

[175] M. Allegrini, E. Arimondo, and L. A. Orozco, "Survey of hyperfine structure measurements in alkali atoms," *J. Phys. Chem. Ref. Data*, vol. 51, no. 4, 2022.

[176] R. V. Krems, G. C. Groenenboom, and A. Dalgarno, "Electronic interaction anisotropy between atoms in arbitrary angular momentum states," *J. Phys. Chem. A*, vol. 108, pp. 8941–8948, OCT 2004.

[177] M. L. González-Martínez and J. M. Hutson, "Sympathetic cooling of fluorine atoms with ultracold atomic hydrogen," *Phys. Rev. A*, vol. 88, no. 5, p. 053420, 2013. Publisher: American Physical Society.

[178] V. Aquilanti, D. Ascenzi, D. Cappelletti, and F. Pirani, "Velocity dependence of collisional alignment of oxygen molecules in gaseous expansions," *Nature*, vol. 371, pp. 399–402, Sept. 1994. Publisher: Nature Publishing Group.

[179] M. D. Frye and J. M. Hutson, "Characterizing feshbach resonances in ultracold scattering calculations," *Phys. Rev. A*, vol. 96, no. 4, p. 042705, 2017.

[180] M. D. Frye and J. M. Hutson, "Characterizing quasibound states and scattering resonances," *Phys. Rev.*, vol. 2, no. 1, p. 013291, 2020.

[181] V. V. Flambaum, G. F. Gribakin, and C. Harabati, "Analytical calculation of cold-atom scattering," *Phys. Rev. A*, vol. 59, pp. 1998–2005, Mar 1999.

[182] H. Nussenzveig, "The poles of the s-matrix of a rectangular potential well of barrier," *Nuclear Physics*, vol. 11, pp. 499–521, 1959.

[183] M. D. Frye and J. M. Hutson, "Characterizing feshbach resonances in ultracold scattering calculations," *Phys. Rev. A*, vol. 96, no. 4, p. 042705, 2017.

[184] R. A. Fisher, "Statistical methods for research workers," in *Breakthroughs in statistics: Methodology and distribution*, pp. 66–70, Springer, 1970.

[185] S. Kotochigova, "Controlling interactions between highly magnetic atoms with feshbach resonances," *Rep. Prog. Phys.*, vol. 77, no. 9, p. 093901, 2014.

[186] E. Soave, A. Canali, Z.-X. Ye, M. Kreyer, E. Kirilov, and R. Grimm, "Optically trapped feshbach molecules of fermionic dy 161 and k 40," *Phys. Rev. Research*, vol. 5, no. 3, p. 033117, 2023.

[187] Z.-X. Ye, A. Canali, E. Soave, M. Kreyer, Y. Yudkin, C. Ravensbergen, E. Kirilov, and R. Grimm, "Observation of low-field feshbach resonances between dy 161 and k 40," *Physical Review A*, vol. 106, no. 4, p. 043314, 2022.

[188] K. Baumann, N. Q. Burdick, M. Lu, and B. L. Lev, "Observation of low-field fano-feshbach resonances in ultracold gases of dysprosium," *Phys. Rev. A*, vol. 89, no. 2, p. 020701, 2014.

[189] M. Lecomte, A. Journeaux, L. Renaud, J. Dalibard, and R. Lopes, "Loss features in ultracold dy 162 gases: Two-versus three-body processes," *Phys. Rev. A*, vol. 109, no. 2, p. 023319, 2024.

[190] M. Lecomte, A. Journeaux, J. Veschambre, J. Dalibard, and R. Lopes, "Production and stabilization of a spin mixture of ultracold dipolar bose gases," *Physical Review Letters*, vol. 134, no. 1, p. 013402, 2025.

[191] J. Mitroy and M. W. J. Bromley, "Semiempirical calculation of van der waals coefficients for alkali-metal and alkaline-earth-metal atoms," *Phys. Rev. A*, vol. 68, p. 052714, Nov 2003.

[192] A. Ciamei, A. Koza, M. Gronowski, and M. Tomza, "Ultracold high-spin

\

sigma $-state polar molecules for new physics searches,"$ $arXiv preprint arXiv$: 2507.16760, 2025.

[193] A. Ciamei, S. Finelli, A. Trenkwalder, M. Inguscio, A. Simoni, and M. Zaccanti, "Exploring ultracold collisions in li 6-cr 53 fermi mixtures: Feshbach resonances and scattering properties of a novel alkali-transition metal system," *Physical Review Letters*, vol. 129, no. 9, p. 093402, 2022.

[194] S. Finelli, A. Ciamei, B. Restivo, M. Schemmer, A. Cosco, M. Inguscio, A. Trenkwalder, K. Zaremba-Kopczyk, M. Gronowski, M. Tomza, *et al.*, "Ultracold li cr: A new pathway to quantum gases of paramagnetic polar molecules," *PRX Quantum*, vol. 5, no. 2, p. 020358, 2024.

[195] V. Barbé, A. Ciamei, B. Pasquiou, L. Reichsöllner, F. Schreck, P. S. Żuchowski, and J. M. Hutson, "Observation of feshbach resonances between alkali and closed-shell atoms," *Nat. Phys.*, vol. 14, no. 9, pp. 881–884, 2018.

[196] B. L. Augenbraun, L. Anderegg, C. Hallas, Z. D. Lasner, N. B. Vilas, and J. M. Doyle, "Chapter two - direct laser cooling of polyatomic molecules," in *Advances in Atomic, Molecular, and Optical Physics* (L. F. DiMauro, H. Perrin, and S. F. Yelin, eds.), vol. 72, pp. 89–182, Academic Press, 2023.

[197] N. R. Hutzler, "Polyatomic molecules as quantum sensors for fundamental physics," *Quantum Sci. Technol.*, vol. 5, p. 044011, 2020.

[198] J. M. Doyle, B. L. Augenbraun, and Z. D. Lasner, "Ultracold polyatomic molecules for quantum science and precision measurements," *JPS Conf. Proc.*, vol. 37, p. 011004, 2022. Proceedings of the 24th International Spin Symposium (SPIN2021).

[199] I. Kozyryev and N. R. Hutzler, "Precision measurement of time-reversal symmetry violation with laser-cooled polyatomic molecules," *Phys. Rev. Lett.*, vol. 119, p. 133002, 2017.

[200] L. Anderegg, N. B. Vilas, C. Hallas, P. Robichaud, A. Jadbabaie, J. M. Doyle, and N. R. Hutzler, "Quantum control of trapped polyatomic molecules for eEDM searches," *Science*, vol. 382, pp. 665–668, Nov 2023.

[201] I. Kozyryev, Z. Lasner, and J. M. Doyle, "Enhanced sensitivity to ultralight bosonic dark matter in the spectra of the linear radical SrOH," *Phys. Rev. A*, vol. 103, p. 043313, 2021.

[202] E. B. Norrgard, D. S. Barker, S. Eckel, N. R. Hutzler, L. Liu, J. M. Doyle, and D. DeMille, "Nuclear-spin dependent parity violation in optically trapped polyatomic molecules," *Commun. Phys.*, vol. 2, no. 1, p. 77, 2019.

[203] B. L. Augenbraun, Z. D. Lasner, A. Frenett, H. Sawaoka, A. T. Le, J. M. Doyle, and T. C. Steimle, "Observation and laser spectroscopy of ytterbium monomethoxide, $yboch_3$," *Phys. Rev. A*, vol. 103, p. 022814, Feb 2021.

[204] M. L. Wall, K. Maeda, and L. D. Carr, "Simulating quantum magnets with symmetric top molecules," *Annalen der Physik*, vol. 525, pp. 845–865, 2013.

[205] M. L. Wall, K. Maeda, and L. D. Carr, "Realizing unconventional quantum magnetism with symmetric top molecules," *New J. Phys.*, vol. 17, p. 025001, Feb 2015.

[206] Q. Wei, S. Kais, B. Friedrich, and D. Herschbach, "Entanglement of polar symmetric top molecules as candidate qubits," *J. Chem. Phys.*, vol. 135, p. 154102, 2011.

[207] P. Yu, L. W. Cheuk, I. Kozyryev, and J. M. Doyle, "A scalable quantum computing platform using symmetric-top molecules," *New J. Phys.*, vol. 21, p. 093049, 2019.

[208] V. V. Albert, J. P. Covey, and J. Preskill, "Robust Encoding of a Qubit in a Molecule," *Phys. Rev. X*, vol. 10, p. 031050, 2020.

[209] T. A. Isaev and R. Berger, "Polyatomic candidates for cooling of molecules with lasers from simple theoretical concepts," *Phys. Rev. Lett.*, vol. 116, p. 063006, Feb 2016.

[210] M. Li, J. Kłos, A. Petrov, and S. Kotochigova, "Emulating optical cycling centers in polyatomic molecules," *Commun Phys*, vol. 2, no. 1, p. 148, 2019.

[211] M. Li, J. Kłos, A. Petrov, H. Li, and S. Kotochigova, "Effects of conical intersections on hyperfine quenching of hydroxyl oh in collision with an an ultracold sr atom," *Scientific Reports*, vol. 10, no. 1, p. 14130, 2020.

[212] T. A. Isaev, A. V. Zaitsevskii, and E. Eliav, "Laser-coolable polyatomic molecules with heavy nuclei," *J. Phys. B: At. Mol. Opt. Phys.*, vol. 50, p. 225101, Oct 2017.

[213] C. Zhang, P. Yu, C. J. Conn, N. R. Hutzler, and L. Cheng, "Relativistic coupled-cluster calculations of raoh pertinent to spectroscopic detection and laser cooling," *Phys. Chem. Chem. Phys.*, vol. 25, pp. 32613–32621, 2023.

[214] W. Xia, H. Ma, and W. Bian, "Production of ultracold cacch and srcch molecules by direct laser cooling: A theoretical study based on accurate ab initio calculations," *J. Chem. Phys.*, vol. 155, p. 204304, 2021.

[215] M. V. Ivanov, F. H. Bangerter, P. Wójcik, and A. I. Krylov, "Toward Ultracold Organic Chemistry: Prospects of Laser Cooling Large Organic Molecules," *J. Phys. Chem. Lett.*, vol. 11, pp. 6670–6676, 2020.

[216] G.-Z. Zhu, D. Mitra, B. L. Augenbraun, C. E. Dickerson, M. J. Frim, G. Lao, Z. D. Lasner, A. N. Alexandrova, W. C. Campbell, J. R. Caram, J. M. Doyle, and E. R. Hudson, "Functionalizing aromatic compounds with optical cycling centres," *Nat. Chem.*, vol. 14, pp. 995–999, 2022.

[217] C. E. Dickerson, H. Guo, A. J. Shin, B. L. Augenbraun, J. R. Caram, W. C. Campbell, and A. N. Alexandrova, "Franck-condon tuning of optical cycling centers by organic functionalization," *Phys. Rev. Lett.*, vol. 126, p. 123002, Mar 2021.

[218] D. Mitra, Z. D. Lasner, G.-Z. Zhu, C. E. Dickerson, B. L. Augenbraun, A. D. Bailey, A. N. Alexandrova, W. C. Campbell, J. R. Caram, E. R. Hudson, and J. M. Doyle, "Pathway toward optical cycling and laser cooling of functionalized arenes," *J. Phys. Chem. Lett.*, vol. 13, pp. 7029–7035, 2022.

[219] M. Morita, J. Kłos, A. A. Buchachenko, and T. V. Tscherbul, "Cold collisions of heavy $^2\blacksquare$ molecules with alkali-metal atoms in a magnetic field: Ab initio analysis and prospects for sympathetic cooling of $\mathbf{SrOH}(^2\blacksquare^+)$ by $\mathbf{Li}(^2S)$," *Phys. Rev. A*, vol. 95, p. 063421, 2017.

[220] M. B. Kosicki, M. Borkowski, M. Umiński, and P. S. Żuchowski, "Production of ultracold asymmetric tops from sr atoms and sroh molecules," *arXiv preprint arXiv:2508.14543*, 2025.

[221] T. C. Steimle, D. A. Fletcher, K. Y. Jung, and C. T. Scurlock, "A supersonic molecular beam optical Stark study of CaOH and SrOH," *J. Chem. Phys.*, vol. 96, pp. 2556–2564, Feb 1992.

[222] A. Frisch, M. Mark, K. Aikawa, S. Baier, R. Grimm, A. Petrov, S. Kotochigova, G. Quéméner, M. Lepers, O. Dulieu, and F. Ferlaino, "Ultracold Dipolar Molecules Composed of Strongly Magnetic Atoms," *Phys. Rev. Lett.*, vol. 115, p. 203201, Nov 2015.

[223] L. D. Augustovičová and J. L. Bohn, "Manifestation of quantum chaos in Fano-Feshbach resonances," *Phys. Rev. A*, vol. 98, p. 023419, Aug 2018.

[224] J. F. E. Croft, C. Makrides, M. Li, A. Petrov, B. K. Kendrick, N. Balakrishnan, and S. Kotochigova, "Universality and chaoticity in ultracold k+krb chemical reactions," *Nat. Comm.*, vol. 8, no. 15897, 2017.

[225] T. Karman, M. Gronowski, M. Tomza, J. J. Park, H. Son, Y.-K. Lu, A. O. Jamison, and W. Ketterle, "Ab initio calculation of the spectrum of feshbach resonances in nali+ na collisions," *Phys. Rev. A*, vol. 108, no. 2, p. 023309, 2023.

[226] J. J. Park, H. Son, Y.-K. Lu, T. Karman, M. Gronowski, M. Tomza, A. O. Jamison, and W. Ketterle, "Spectrum of feshbach resonances in na li+ na collisions," *Phys. Rev. X*, vol. 13, no. 3, p. 031018, 2023.

[227] P. S. Żuchowski, J. Aldegunde, and J. M. Hutson, "Ultracold rbsr molecules can be formed by magnetoassociation," *Phys. Rev. Lett.*, vol. 105, p. 153201, Oct 2010.

[228] S. V. Alyabyshev, T. V. Tscherbul, and R. V. Krems, "Microwave-laser-field modification of molecular collisions at low temperatures," *Phys. Rev. A*, vol. 79, p. 060703(R), 2009.

[229] T. V. Tscherbul, G. Groenenboom, R. V. Krems, and A. Dalgarno, "Dynamics of OH(2Π)He collisions in combined electric and magnetic fields," *Faraday Discuss.*, vol. 142, p. 127, 2009.